# Searches for new physics phenomena with jet final states in the ATLAS detector

Brottmann Hansen, Eva

2020

*Document Version:*
Publisher's PDF, also known as Version of record

Link to publication

*Citation for published version (APA):*
Brottmann Hansen, E. (2020). *Searches for new physics phenomena with jet final states in the ATLAS detector*. [Doctoral Thesis (monograph), Particle and nuclear physics]. Lund University.

*Total number of authors:*
1

LUND UNIVERSITY

PO Box 117
221 00 Lund
+46 46-222 00 00

# Searches for new physics phenomena with jet final states in the ATLAS detector

by Eva Brottmann Hansen

LUND
UNIVERSITY

Thesis for the degree of Doctor of Philosophy
Thesis advisors: Dr. Caterina Doglioni
Faculty opponent: Niki Saoulidou

To be presented, with the permission of the Faculty of Science of Lund University, for public criticism in the Rydberg lecture hall (Rydbergsalen) at the Department of Physics on the 3rd of December 2020 at 13:00.

Organization
**LUND UNIVERSITY**

Department of Physics
Box 118
SE–221 00 LUND
Sweden

Document name
**DOCTORAL DISSERTATION**

Date of disputation
2020-12-03

Sponsoring organization
The European Research Council

Author(s)
Eva Brottmann Hansen

Title and subtitle
Searches for new physics phenomena with jet final states in the ATLAS detector

Abstract

Collimated sprays of particles, known as *jets*, are abundantly produced in high-energy proton-proton (*pp*) collisions, and predicted by many theories of physics beyond the Standard Model. This thesis reports first on the calibration of jets with focus on the data-driven *in situ* calibration. Two searches for new physics phenomena in events with jets in the final state are then presented. The analyses use $\sqrt{s} = 13$ TeV *pp* collision data collected by the ATLAS experiment at the LHC.

The response to small- and large-radius jets is measured *in situ* using data collected between 2015 and 2017. The jet energy scales are measured in events where a jet recoils against a calibrated reference object. The mass scale of large-radius jets is measured with two methods: one uses track jets to provide an independent measurement of the jet mass, the other uses $t\bar{t}$-events with boosted, hadronically decaying $W$-bosons and top quarks.

The first analysis is a search for massive coloured objects which are pair-produced and decay to two jets. The data was recorded between 2015 and 2016, corresponding to an integrated luminosity of 36.7 fb$^{-1}$ of data. Two selections of four-jet events are defined; one with two *b*-tagged jets and one inclusive. No significant deviation from the expected background of Standard Model processes is observed in either of the event selections. The results are interpreted in a SUSY simplified model where the lightest supersymmetric particle is a stop squark, which decays to two quarks through *R*-parity violating couplings. Limits are derived on the the stop squark mass and on the mass of pair-produced colour-octet resonances. The scenario where the two squarks decays to a *b*-quark and a lighter quark is considered separately using the *b*-tagged event selection.

The second analysis is still ongoing and using data collected between 2015 and 2018, which corresponds to an integrated luminosity of 139 fb$^{-1}$. The search looks for a resonance, which could be a mediator between a confined hidden sector and the Standard Model sector. The mediator decays to two dark partons which shower and hadronise according to the dynamics of the hidden sector. The search targets a selection of model parameters where all dark hadrons decay promptly to visible particle. The signature is a pair of "dark jets" with different characteristics than Standard Model QCD-jets. An mass-decorrelated tagger is defined based on the number of tracks associated with the jet. The tagger is designed to distinguish dark jets from the QCD background, without distorting the smoothly falling background distribution.

Key words
particle physics, jets, dark matter, supersymmetry, hidden sectors

Classification system and/or index terms (if any)

Supplementary bibliographical information

Language
English

ISSN and key title

ISBN
978-91-7895-685-2 (print)
978-91-7895-684-5 (pdf)

Recipient's notes

Number of pages
185

Price

Security classification

I, the undersigned, being the copyright owner of the abstract of the above-mentioned dissertation, hereby grant to all reference sources the permission to publish and disseminate the abstract of the above-mentioned dissertation.

Signature

Date 2020-10-23

DOKUMENTDATABLAD enl SIS 61 41 21

# Searches for new physics phenomena with jet final states in the ATLAS detector

by Eva Brottmann Hansen

LUND
UNIVERSITY

**Cover illustration front:** Artistic interpretation of a parton shower (Credits: Trine Poulsen)

**Funding information:** The work in this thesis is part of a project that has received funding from the European Research Council under the European Union Horizon 2020 research and innovation program (grant agreement 679305).

Faculty of Science, Department of Physics

ISBN: 978-91-7895-685-2 (print)
ISBN: 978-91-7895-684-5 (pdf)

Printed in Sweden by Media-Tryck, Lund University, Lund 2020

# Abstract

Collimated sprays of particles, known as *jets*, are abundantly produced in high-energy proton-proton ($pp$) collisions, and predicted by many theories of physics beyond the Standard Model. This thesis reports first on the calibration of jets with focus on the data-driven *in situ* calibration. Two searches for new physics phenomena in events with jets in the final state are then presented. The analyses use $\sqrt{s} = 13$ TeV $pp$ collision data collected by the ATLAS experiment at the LHC.

The response to small- and large-radius jets is measured *in situ* using data collected between 2015 and 2017. The jet energy scales are measured in events where a jet recoils against a calibrated reference object. The mass scale of large-radius jets is measured with two methods: one uses track jets to provide an independent measurement of the jet mass, the other uses $t\bar{t}$-events with boosted, hadronically decaying $W$-bosons and top quarks.

The first analysis is a search for massive coloured objects which are pair-produced and decay to two jets. The data was recorded between 2015 and 2016, corresponding to an integrated luminosity of 36.7 fb$^{-1}$ of data. Two selections of four-jet events are defined; one with two $b$-tagged jets and one inclusive. No significant deviation from the expected background of Standard Model processes is observed in either of the event selections. The results are interpreted in a SUSY simplified model where the lightest supersymmetric particle is a stop squark, which decays to two quarks through $R$-parity violating couplings. Limits are derived on the the stop squark mass and on the mass of pair-produced colour-octet resonances. The scenario where the two squarks decays to a $b$-quark and a lighter quark is considered separately using the $b$-tagged event selection.

The second analysis is still ongoing and using data collected between 2015 and 2018, which corresponds to an integrated luminosity of 139 fb$^{-1}$. The search looks for a resonance, which could be a mediator between a confined hidden sector and the Standard Model sector. The mediator decays to two dark partons which shower and hadronise according to the dynamics of the hidden sector. The search targets a selection of model parameters where all dark hadrons decay promptly to visible particle. The signature is a pair of “dark jets” with different characteristics than Standard Model QCD-jets. An mass-decorrelated tagger is defined based on the number of tracks associated with the jet. The tagger is designed to distinguish dark jets from the QCD background, without distorting the smoothly falling background distribution.

# Populærvidenskabeligt sammendrag

Partikelfysikken stræber efter en fuldkommen forståelse af universets mindste byggesten - *elementarpartiklerne* - og hvordan de interagerer med hinanden - deres *vekselvirkninger*. Fremskridt sker gennem samspil mellem teoretisk indsigt og eksperimentelle observationer, som utallige fysikere verden over bidrager til i fællesskab. Denne fælles stræben førte i det 20. århundrede til enorme landvindinger indenfor vores forståelse af den sub-atomare verden.

Ideen om, at en simpel, underliggende struktur kan forklare den enorme variation af materiale i unverset, stammer tilbage fra oldtidens Grækenland. Den lå dog i dvale et par tusinder år indtil begyndelsen af 1800-tallet, da atomteorien om stof opstod. Efterhånden som flere og flere atomare grundstoffer blev opdaget, begyndte man at ane et mønster i grundstoffernes karaktertræk. Omkring begyndelsen af 1900-tallet blev det tydeligt, at atomerne ikke er fundamentale enheder, men sammensatte af mindre bestandele. Det skulle vise sig, at atomer består af en positivt ladet kerne som er omgivet af negativt ladede elektroner. Denne underliggende struktur kunne forklare både det store antal grundstoffer, men også deres regelmæssige opførsel, som vi kender fra det periodiske system.

Sidenhen viste det sig at selv atomkernerne bestod af mindre dele: Positivt ladede *protoner* og elektrisk neutrale *neutroner*. Måske var elektronerne, protonerne og neutronerne i virkeligheden de ultimativt fundamentale byggesten? Håbet svandt i løbet af 1950'erne da flere og flere proton- og neutron-lignende partikler blev opdaget. Disse *hadroner* lod sig villigt arrangere i periodiske mønstre og billedet begyndte at minde om 1800-tallets grundstoffer. Det sendte datidens fysikere på en hæsblæsende jagt efter hadronernes underliggende struktur. Ved at beskyde protoner med høj-energiske elektroner, stod det omkring år 1970 klart, at protonernes masse rigtignok er koncentreret omkring små- faktisk punktlignende - partikler ved navn *kvarker*. Opdagelsen, holdt hårdt, da kvarker ikke kan eksistere alene, men omdanner sig til en sværm af hadroner i det øjeblik, de bliver skabt. Hvis en kvark bliver skabt med høj nok energi, bevæger sværmen af hadroner sig i samme retning, og danner hvad vi kalder en *jet*. Først da man kunne skabe tilstrækkeligt høj energi til direkte at se sådanne jets i detektorerne, blev de sidste tvivlere overbevist om kvarkernes virkelige eksistens.

Siden 1970'erne er flere slags kvarker og elektroner blevet opdaget, men endnu ser de ud til at opføre sig som fundamentale, og betegnes derfor som elementarpartikler. Vores samlede viden om alle elemtarpartiklerne og deres vekselvirkninger er beskrevet i en teori ved navn *Standardmodellen*, som er illustreret i Figur 2.1. Selv for naturvidenskabelige dicipliner er Standardmodellen enestående præcis og omfattende i sine forudsigelser. Dog er der meget, som tyder på at vi endnu ikke har fat i naturens ultimativt fundamentale mønster.

Vi ved i dag, at Standarmodellen som minimum er ukomplet. For eksempel giver den ikke nogen forklaring på hvad tyngdekræft er for en størrelse. Den har heller ikke et bud på hvorfor der er ca. fem gange mere masse i universet end hvad mængden af lys fra galakserne indikerer. Det sidste fænomen kaldes for *mørkt stof*, men ingen ved endnu hvad det egentlig er. Forklaringen involverer højst sandsynligt (mindst) en ny slags partikel, som stort set ikke vekselvirker med de partikler, vi kender. Der er heldigvis ingen mangel på teorier, som kan forklarer både mørkt stof og mange af de andre problemer, som Standardmodellen bakser med. Nogle de mest tiltalende teorier forudsiger en hel sektor af nye partikler med deres egen interne dynamik.

Måden hvorpå vi bliver studerer elementarpartiklerne, er stadig ved at kollidere f.eks. protoner eller elektroner med en høj energi, og måle de partikler, der kommer ud af kollisionen. Einsteins masse-energi-ækvivalens, $E = mc^2$, betyder at selv tunge partikler, der ikke findes i protonerne i udgangspunktet, kan skabes ud af energien, som er til rådighed i kollisionen. På CERN i Schweiz findes verdens største partikelaccelerator, The Large Hadron Collider (LHC), og den er beregnet netop til dette formål. I en 27 km lang, cirkulær tunnel accelereres protoner op til nær lystes hastighed, før de bliver bragt til at kollidere i de fire eksperimenter langs ringen.

Denne afhandling tager udgangspunkt i data fra LHC, som er samlet med ATLAS eksperimentet. To forskellige dataanalyser vil blive præsentereret, som begge har til formål at lede efter afvigelser i data fra Standardmodellens forudsigelser. Specifikt, ser vi efter afvigelser, som kunne skyldes en ny, tung partikel. Standardmodellen er efterhånden så gennemtestet, at vi må gå ud fra, at afvigelser forekommer uhyre sjældent. Derfor er det nu nødvendigt, at målrette vores analyser til helt specifikke scenarier, som ellers kunne blive overset.

I den første analyse afsøger vi nogle mulige teorier for *supersymmetri*. Disse teorier postulerer en udvidelse af Standardmodellen med en slags spejlbillede af de partikler vi allerede kender. Specifikt leder vi efter “spejlbilledet” til en af de velkendte kvarker. Denne nye partikel skulle som oftest skabes i par og derefter henfalder til to kvarker. Det vil altså sige, at vi kigger på de begivenheder, som resulterer i fire jets. Jeg må desværre afsløre, at der i resultatet ingen afvigelse er at se fra Standardmodellen med den tilgængelige data.

I den anden analyse, leder vi efter en ny, tung partikel, der kunne fungere som en slags portal til en for-os-usynlig, eller “mørk”, partikelsektor, der minder om den kvarksektor vi kender fra Standardmodellen. Når den tunge partikel henfalder til to mørke kvarker, vil disse danne jets af mørke hadroner i overensstemmelse med den dynamik, der regerer i den mørke sektor. En sådan jet vil i udgangspunktet være usynlig i vores detektor, men hvis de mørker hadroner hurtigt nok henfalder tilbage til Standarmodelpartikler vil de faktisk blive synlige. Det vil sige, at vi her ser efter begivenheder med to jets, der afviger i udseende fra dem vi er vant til. Denne analyse er endnu ikke nået til nogen konklusion, så håbet for ny fysik lever fortsat.

# List of Publications

Some of the original work documented in this thesis, has led to results which have already been reported in the following publications:

**In situ calibration of large-radius jet energy and mass in 13 TeV proton-proton collisions with the ATLAS detector**
*ATLAS Collaboration*
Eur. Phys. J. C **79** (2019) no.2, 135

**A search for pair-produced resonances in four-jet final states at $\sqrt{s} = 13$ TeV with the ATLAS detector**
*ATLAS Collaboration*
Eur. Phys. J. C **78** (2018) no.3, 250

**Search for low-mass dijet resonances using trigger-level jets with the ATLAS detector in $pp$ collisions at $\sqrt{s} = 13$ TeV**
*ATLAS Collaboration*
Phys. Rev. Lett. **121** (2018) no.8, 081801

**Jet energy scale and resolution measured in proton-proton collisions at $\sqrt{s} =$ TeV with the ATLAS detector**
*ATLAS Collaboration*
CERN-EP-2020-083
Submitted to EPJC-20-07-046

# Acknowledgements

The results presented in this thesis are all products of many people's work and contributions. The data itself relies on the successful operation of the LHC and ATLAS which occupy thousands of physicists and engineers. The data analyses have been performed in collaboration with several ATLAS colleagues. Furthermore, I would not have been able to write this thesis without the guidance, support, and inspiration from many good colleagues and friends. As such, a good number of names deserve recognition for their contributions:

First and foremost, I wish to thank my supervisor, Caterina, who have guided me on this journey with encouragements, attention to my well-being, and an infectious enthusiasm for physics. Your confidence in my abilities and appreciation for every little job I did, always kept the infamous imposter syndrome at a safe distance. I have felt I could reach out to you any time, and always known where to find you (if not in the office, *always* available online).

I also wish to thank my co-supervisors, Torsten and Roman, who have been available for physics chats and councelling whenever needed. To Bogdan Malaescu, my technical supervisor on my ATLAS qualification task, if not for you I would never have found my way around the in-situ combination code, so thank you for teaching me the ropes.

A special thanks to Murrough Landon, who mentored me in my work for the gFEX software. Though we never got as far with the project as hoped, I greatly appreciate the time and effort you spent teaching me about the L1Calo and everything related. Our chats and work sessions at CERN were very enjoyable.

The Dark Jet Resonance team, Jannik, Dilia, Nathan, Marie-Helene, and Caterina, thank you very much for the collaboration over the past two year. It has been a pleasure to share goals, results, doubts, and curiosities with you, and I hope to meet you all at CERN in the near future.

I am also very grateful for the feedback I have received on the thesis itself. Thank you to David Sylvermyr for reviewing (and approving) the thesis draft. Thank you to Göran Jarlskog for taking a critical look at the theory chapter, and not least to Trine for reading the jet chapter and helping to design the cover. This book would have been much worse off without you.

The Particle Physics Division at Lund University, has been a wonderful and nourishing place to grow up scientifically. Thank you to all my colleagues here for making everyday both fun and educational through lunch discussions, seminars, doctoral student days, after-works, excursions, and Christmas parties.

Particularly my colleagues in the ATLAS PhD office, have mean a great deal to me. I have been lucky to be surrounded everyday by wonderful friends with all kinds of skills and knowledge from which I have benefited. My jet experts, trigger experts, tracking experts, python experts, theory experts, computing experts, documentation experts, and most excellent debugger ducks, you have taught me so much and made my years in Lund a very happy time. Though we are scattering now little by little, I look forward to meeting all of you around in the world for many years to come.

Finally, Mikko, thank you for cheering me on these past six months. Falling in love while finishing a PhD unavoidably introduces some internal conflicts of interest, but you made it easy for me to balance those interests. In fact, having a former theoritician in the house, willing to discuss all the many things I don't understand about physics, has been very helpful. Your company, your patience, your cooking, and your rewards for every page written, made some potentially difficult months a very happy time for me.

The work in this thesis is part of a project that has received funding from the European Research Council under the European Union Horizon 2020 research and innovation program (grant agreement 670305).

# Contents

# Part I

# Introductions

# Chapter 1

# Introduction to the Thesis

## 1.1 Particle physics anno 2020

Particle physics is the study of the most fundamental elements of matter and their interactions. Based on the ancient notion that a simple underlying structure is responsible for all the variety of matter around, one can say that particle physics strives towards and understanding of everything. The last time a new layer of structure was discovered, was during the late 1960s to early 1970 when it became evident that protons and neutrons are not elementary, but built from even tinier objects. Hereby, the understanding of particle physics as we see it today, was established.

Many of the methods and principles of particle physics were, however, founded during the preceding decades. By the year 1950, following the discoveries of the electron, positron, proton, and neutron, physicist thought that the fundamental constituents of matter was a closed chapter. Only a few details still needed to fall into place. The discovery of the neutrino in 1956 would soon provide an explanation for one of those details, while the concurrent discoveries of multiple new particles would create many more.

At that time, a quantum field theory of electrodynamics had proven to explain the interactions of charged particles with an astonishing accuracy, using the photon as the force carrier. The triumph of quantum electrodynamics gave physicists confidence that a similar dynamics, involving pions, would soon explain the strong interactions between neutrons and protons. As experiments attempted to unveil strong interactions, new families of particles, similar to protons and pions, began to emerge during the 1950s. These many *hadrons* caused severe unease, leading Enrico Fermi to complain “If I could remember the names of all these particles, I’d have become a botanist instead of a physicist”. To his and many others comfort, a simpler underlying structure was indeed at play. Hadrons eventually came to be understood as composite of just a handful of even smaller, fractionally charged entities, called quarks.

The physical reality of quarks as more than a mathematical curiosity was not readily accepted. By bombarding protons and neutrons with high-energy electrons, it was clear that the nucleon mass was centered around a few point-like objects, but quarks refused to reveal themselves in isolation. Somehow quarks had to metamorphose into hadrons before they reached the detector. Direct observational evidence of quark's individual existence came in the shape of *jets*: Sprays of hadrons emerging from the collision in a few specific directions. Jets could only be (simply) explained as a quark getting kicked out of the proton with a high transverse momentum to then swarm itself with hadrons flying off in the same direction. The visible appearance of jets in hadron collisions during the late 1970s, convinced the last remaining skeptics.

Our knowledge of particle physics today, can be condensed to a single quantum field theory, called the *Standard Model*. It is built on the same principles as quantum electrodynamics, and it stands even more triumphant. Explaining not only the dynamics of the particles known at the time it was formulated, the Standard Model also predicted the existence of new particles which were later discovered. The last predicted particle to be discovered, was the Higgs boson in 2012. The discovery ultimately demonstrated the predictive power of the Standard Model, but once again, a few exceptions to the tale of triumphs remain.

One of the more bewildering exceptions is the repeated observation that there is much more gravitational mass in the universe than the luminous matter indicates. The Standard Model does not provide a viable explanation for this unknown substance, so we simply call it *dark matter*. Even gravitation is not accounted for by the Standard Model. Clearly, we are still short of a theory of everything.

As in the 1950s, our hope today is that an expansion of the quantum field theory we have, will unravel the remaining mysteries. Perhaps some explanations will once again be found in yet another layer of structure, hiding within thought-to-be fundamental constituents? Perhaps the discovery of a new particle will be the telltale of a missing symmetry? The approach for testing new theories is still to collide particles with high energy, and study what comes out of the collision. Heisenberg's uncertainty principle teaches us that the smaller a thing we want to probe, the higher the energy needed. The available collision energy also sets the limit of how heavy particles can be created, due to Einstein's famous mass-energy equivalence. For these reasons, particle physics is also called *high energy physics*.

The Large Hadron Collider (LHC) at CERN marks the highest energy frontier of particle physics so far. It was at the LHC that the Higgs boson was finally discovered. At the start of the LHC, it was the expectation and hope of most physicists, that a particularly appealing extension to the Standard Model, called *supersymmetry*, would soon be discovered. Supersymmetry (SUSY) has the potential to solve many of the problems posed by the Standard

Model, and can even provide a particle candidate for dark matter. But the predictions of the simplest supersymmetric theories have yet to be observed at the TeV scale. Instead, many physicist are directing their attention towards more complex signatures which could arise from less conventional SUSY models, or other kinds of hidden particle sectors.

We stand today at a unique point in the history of particle physics. We have a model which is astonishingly accurate at the energy scale we can reach, yet we know it to be incomplete. The strategy is now to narrow down the search field of possible new physics theories, starting with the best motivated ones. With an apparent lack of experimental clues, we are guided by constraints from cosmology and astronomy, and the historically founded belief that the laws of nature are aesthetic and symmetric.

## 1.2 Overview of the dissertation

The work presented in this thesis is centered around jets. Not only are jets abundant and striking signatures in proton collisions, they are also predicted as the final state in a wealth of models for physics beyond the Standard Model. The thesis gives detailed account of the principles of measuring and calibrating jets. This is followed by the report of two analyses, which both aim to look for new physics phenomena beyond the Standard Model, using events with jets in the final state. The analysed proton-proton collision data is collected with the ATLAS experiment at the LHC.

The first analysis tests a supersymmetric extension to the Standard Model, where the lightest supersymmetric particle decays promptly to a pair of quarks through an $R$-parity violating coupling. The second analysis looks for signs of new physics in the less conventional form of a *hidden sector* that is weakly coupled to the Standard Model particle sector. The hidden sector is characterised by a confining gauge interaction, which could gives rise to jets with distinguishable substructure.

The thesis is divided into three parts:

- **Part I:** The first part introduces the theoretical and experimental concepts and tools, necessary to give a comprehensive explanation of the presented searches. We start in Chapter 2 with the theoretical foundation regarding both the Standard Model and the possible extensions which the two analyses aim to test. Chapter 3 gives an overview of the experimental setup where the analyzed data is recorded.

- **Part II:** The second part revolves around the topic of how jets are measured. In Chapter 4 we will se how jets are defined and reconstructed. Chapter 5 reviews the calibration of the measured jets, with a particular emphasis of the data-driven *in situ* calibration. Chapter 6 explains how different types of jets can be identified based on their substructure.

- **Part III:** In the third part of this thesis, the two analyses are finally presented. Chapter 7 summarises the search for $R$-parity violating stop squarks using events with four jets in the final state. Chapter 8 reports on the ongoing search for jets arising from a confined hidden sector.

## 1.3 Author's contributions

The results presented in this thesis have all been achieved in smaller groups, but were made possible by the combined efforts of the entire ATLAS collaboration roughly 3000 active members. With that said, I list my own personal contributions below:

- **Chapter 3:** My contributions to running and upgrading the experiment are not directly reflected in the document, still I mention them here. I have been involved with the upgrade of the Level-1 calorimeter trigger, specifically the gFEX module. My contributions have been to test and improve communication between the module and the TDAQ system, and begin the development of the control software. I have also done expert on-call shifts for the Level-1 Calorimeter Trigger during data-taking periods.

- **Chapter 5:** The first project I did in ATLAS was on the combination of *in situ* calibrations for large-radius jets. I adapted the existing combination code from the small-radius jet $p_{\mathrm{T}}$ calibration to the large-radius jet $p_{\mathrm{T}}$ and mass calibrations. Since then, I have been running, maintaining, and updating the framework for both small- and large-radius jets for each new year of data taking. This work is documented in Sections 5.3.4, 5.3.5, and 5.4.3.

- **Chapter 7:** During my first year as a PhD student, I also got involved with the search for $R$-parity violating stop squarks in event with four jets. I performed fits of the multi-jet background, as described in Section 7.6 and 7.9, which were used to validate the nominal background estimate and assign an uncertainty to it.

- **Chapter 8:** For the last two years I have been increasingly focused on the Dark Jet Resonance search, especially as analysis coordinator for the past year. My main contribution has been to design the signal region selection while ensuring a constant background efficiency across the search spectrum. This work is documented in Section 8.6. I have also been responsible for testing and implementing the baseline event selection, Section 8.3, and studied effects of changing the dark meson decay modes in the signal sample generation.

# Chapter 2

# The Theoretical Foundation

From the perspective of theoretical physics, nature is governed by symmetries. Symmetries give rise to interactions and conservation laws that determine the dynamics of fundamental particles. The ultimate goal of theoretical particle physics is unification; to combine all governing symmetries of nature in a single theory, and thus obtain a unified description of the four fundamental forces.

The Standard Model of particle physics is a theory of symmetries which combines three of the four fundamental interactions of nature. In spite of its impressive record of predicting experimental results, we know the Standard Model to be incomplete - particularly failing at the high energies still out of reach with current accelerators.

Possible solutions to some of the unanswered questions, are provided by models of supersymmetry [1] and hidden particle sectors [2]. Such extensions to the Standard Model that can be tested at hadron colliders like the LHC.

This chapter introduces the theoretical foundation of the work presented in the thesis. In Section 2.1 the Standard Model is described in a chronolgical fashion to give a some historical context to the work. The phenomenology and simulation of hadron collider physicsis is described in Section 2.2 and 2.3. Finally, Section 2.4 looks at the motivation for searching for physics phenomena *beyond* the predictions of the Standard Model - particularly phenomena of supersymmetry and hidden sectors.

## 2.1 The Standard Model

The Standard Model is a relativistic quantum field theory which describes the known elementary particles and the forces via which they interact. For the past 40 years, it has stood as "The" theory of particle physics, passing numerous experimental tests. The model came about as the distillation of decades of research conducted by numerous scientists. By attempts to explain one anomaly occurring after another, different bits of understanding were obtained piece-wise and put together as the Standard Model during the 1970s [3] [4].

The Standard Model is a theory of interactions, describing three of the four fundamental forces of nature: The strong nuclear force, the electromagnetic force and the weak nuclear force. Gravity, though prominent in the macroscopic lives of humans, is negligible at the minuscule level of particle physics. With a coupling strength to quarks of $10^{-33}$ times the strength of the weak force [5], gravity is not included in the Standard Model. Yet, until the four forces are unified in a single theory, the Standard Model remains the theory of *almost* everything.

The particles in the Standard Model can be divided into two categories: fermions and bosons. Fermions have spin $1/2$ and they include the matter particles that make up everything around us. Bosons have integer spin and mostly act as force carriers. There are two types of fermions, the quarks and the leptons. They are arranged in three generations of increasing mass, where each generation contains two quarks and two leptons. The four force carrying bosons have a spin of 1, while the Higgs boson, giving rise to most of the particle masses, is the only spin-zero particle in the Standard Model.

Figure 2.1 illustrates the particles of the Standard Model, grouped according to their interactions. All atoms around us are made up of the first generation fermions, *up* ($u$) quarks, *down* ($d$) quarks, and electrons ($e$), so these are noted as "standard matter". Fermions of the heavier generations can be produced if sufficient energy is present, but they quickly decay to lighter fermions, why they are noted as "unstable matter".

Mathematically, the dynamics of the Standard Model is described by a *Langrangian* equation, where each particle is represented as a field. The full formulation takes up to a few pages, but the essence can be summarised in a form that easily fits on a coffee mug:

$$\begin{aligned}\mathcal{L}_{\mathrm{SM}} = &-\frac{1}{4}F_{\mu\nu}F^{\mu\nu} \\ &+ i\bar{\psi}\not{D}\psi + \text{h.c.} \\ &+ \psi_i y_{ij}\psi_j\phi + \text{h.c.} \\ &+ |D_\mu\phi|^2 - V(\phi)\end{aligned} \tag{2.1}$$

The first line describes the gauge bosons and how they interact with each other. The second line describes the matter fermions and their interactions via the gauge bosons. In the third

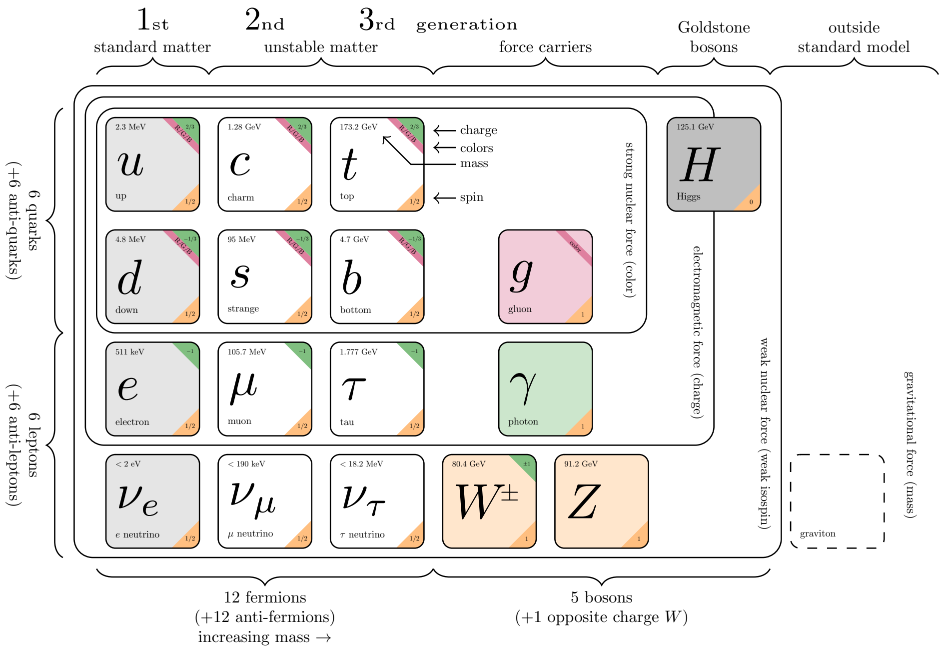

**Figure 2.1:** Compilation of the current understanding of the universe, as seen through the lense of particle physics [6]. Particle charge, colour, mass, and spin are indicated.

line *Yukawa* couplings are introduced, through which fermions interact with the Higgs field. The fourth line adds the boson couplings to the Higgs field and the Higgs field potential, describing the Higgs boson self-couplings.

In its mathematical form, the Standard Model is a theory of symmetries which give rise to the interactions and conservation laws. The Lagrangian is symmetric under translations, rotations and boosts, and is built on the gauge invariant symmetry group $SU(3) \otimes SU(2) \otimes U(1)$.

Each gauge invariant symmetry is roughly responsible for one of the three forces that the Standard Model explains. In the following, I will go through the three types of interactions in the order they were discovered, followed by a brief description of the Higgs mechanism.

### 2.1.1 Electromagnetic interactions: Quantum Electrodynamics

Electricity and magnetism have been known for thousands of years as more or less mysterious phenomena that created lightning and made the compass needle swing. Only in the 19th century was the relation between the two phenomena discovered and electromagnetism understood as a single force.

The groundwork for the quantum field theory of electrodynamics, was laid by Albert Einstein in 1905 who - building on a suggestion by Max Planck - proposed a quantum of light and developed the theory of special relativity [7][8][9]. Followed by the revolutionary work of several contributors to quantum theory, Paul Dirac was in 1928 able to combine quantum mechanics and special relativity in a single theory to describe the electron [10]. As theoretical and experimental difficulties with Dirac's formulation increased, the search for a consistent theory of *quantum electrodynamics* (QED) was on. It would take another couple of decades before a covariant and gauge invariant formulation of QED was introduced, based on the work of Freeman Dyson, Richard Feynman, Julian Schwinger,and Shin'ichiro Tomanaga. QED has since served as the model and template for all subsequent quantum field theories.

In QED, the mediating gauge boson is the photon ($\gamma$) which is charge- and massless and, therefore, has infinite range. The photon couples to all the electrically charged particles, with a coupling constant that is about two orders of magnitude weaker than the strong force. Therefore, the electromagnetic force is particularly important for the charged leptons, as they don't have strong interactions. The electromagnetic force obeys a $U(1)$ symmetry and the conserved quantity of electromagnetic interactions is the electromagnetic charge. However, lepton flavour is also a conserved quantum number.

The charged leptons comes in three *flavours* of (rapidly) increasing masses; the electron $e$, the muon $\mu$ (roughly 200 times heavier than the electron), and the tau lepton $\tau$ (nearly 4000 times the electron mass). The electron was the first particle to be discovered of all the particles we still consider fundamental today. This is why, the unit of electric charge was defined as the charge of the electron.

### 2.1.2 Weak interactions

A theory of weak interactions was first proposed by Enrico Fermi in 1933 as a zero-range contact interaction between four fermions [11]. The motivation was to explain beta decays using Wolfgang Pauli's proposed neutrino, but Fermi's theory only proved valid up to about $100$ GeV. The current formulation came about much later, in 1968, to explain the discovery of parity violation in weak interactions. Sheldon Glashow, Abdus Salam and Steven Weinberg unified the electromagnetic and the weak interaction and showed them as two aspects of a single force - the *electroweak force* [12][13][14]. More on the spontaneous electroweak symmetry breaking in Section 2.1.4.

The suitably named weak interaction has an effective coupling strength which is about an order of magnitude smaller than the electromagnetic force at low energies. The coupling strength increases with energy until the two forces merge into one above $200\,\text{GeV}$. The weak force is mediated by three massive vector bosons; the electrically neutral $Z$ boson, and the two charged $W^{\pm}$ bosons. Due to the force carrier masses of about $80 - 90\,\text{GeV}$, the weak interaction has a range of only $10^{-18}$ m - less than the diameter of a proton.

The weak force affects all fermions. The $W$ boson couples only to particles of left-handed helicity, meaning their spin is oriented opposite to the direction of motion, and anti-particles of right-handed helicity. The $Z$ boson interacts with both left- and right-handed particles. The gauge group of weak force is $SU(2)$ and the conserved charge is called *weak isospin*, or left-helicity handedness. Unlike electromagnetic interactions, weak interactions can change the particle flavour.

Weak interactions are of particular importance for the neutral leptons, namely the *neutrinos*, as they have neither electric nor strong interactions. Like the charged leptons, neutrinos come in the same three flavours; electron neutrino $\nu_e$, the muon neutrino $\nu_\mu$, and the tau neutrino $\nu_\tau$. The neutrinos appear in the Standard Model in flavour doublets with the charged leptons;

$$\begin{pmatrix} e \\ \nu_e \end{pmatrix}_L, \quad \begin{pmatrix} \mu \\ \nu_\mu \end{pmatrix}_L, \quad \begin{pmatrix} \tau \\ \nu_\tau \end{pmatrix}_L \tag{2.2}$$

The subscript $L$ stands for “left” as neutrinos are left-handed. The right-handed counterparts are flavour singlets, $(e_R, \mu_R, \tau_R)$.

In the Standard Model, neutrinos do not couple to the Higgs boson and are therefore massless. However, with the discovery of neutrino oscillations it was established that they do have mass. We return to neutrino masses in Section 2.4.

### 2.1.3 Strong interactions: Quantum Chromodynamics

Around the year 1960 particle physics was a chaotic zoo of observations. During the past decade, a plethora of new hadrons had appeared in cloud chambers all over the world. Most physicists disliked the possibility that there could be 30 fundamental particles in nature, so in an attempt to fix the situation Murray Gell-Mann and George Zweig independently made a drastic suggestion: That hadrons themselves might be composite of tiny, fractionally charged particles. Gell-Mann called the quirky little things *quarks*, allegedly taking their name from the James Joyce novel, *Finnigan's Wake* [15].

The proposal of quarks had major implications. To explain resonances like the $\Delta^{++}$, three identical quarks of charge $+2/3$ and spin $1/2$ required. But this would be a violation of Pauli's exclusion principle, which states that identical fermions (spin $1/2$ particles) can not occupy the same state. In order to form such hadrons, quarks had to be assigned a new quantum number, which was named colour charge and could take on three values; red, green, and blue. The quark model also needed a new force holding the quarks bound together in the hadrons, which was called the strong force seeing as it had to be about 100 times stronger at than the electromagnetic force.

The first evidence of quarks came from electron-proton scattering experiments at the Stanford Linear Accelerator (SLAC) in 1968. An analysis by James Bjorken and Richard Feynman showed that the electrons appeared to be bouncing off small hard cores inside the proton. The observation of proton constituents manifested the quark model as a physical reality rather than a mathematical trick.

The experiments implied that quarks interacted almost as free particles inside the nucleus, meaning that the strong force had to be very week at such small distances. On the other hand, fractionally charged particles had never been observed in spite of many enthusiastic attempts. Therefore, quarks should not be allowed to be observed freely. The strong force had to grow ever stronger with distance to keep the quarks in their bound state. The mediator of this strong force was appropriately named the gluon.

While the original quarks model only required three quarks, it quickly became evident that a fourth quark was necessary to match the patterns seen in the lepton sector. Searches for the fourth quark, named "charm", was evoked. The charm quark was discovered by both SLAC and The Brookhaven National Lab in 1974, as a bound state with its anti-quark, called the J/$\psi$ meson. It was after this discovery that the term "Standard Model" was first coined by Abraham Pais and Sam Treiman in 1975, with reference to the electroweak theory, including four quarks.

The theory of quark and gluon interactions grew into what we call quantum chromodynamics (QCD). Today QCD involves six quarks (and six anti-quarks). The strong force obeys $SU(3)$ symmetry and the conserved quantity is the colour charge.

Because quarks carry colour charge, they predominantly interact via the strong force. In addition to colour, quarks have fractional electrical charge as predicted by Gell-Mann: The *up* ($u$), *charm* ($c$), and *top* ($t$) quarks have a charge of $2/3e$, while *down* ($d$), *strange* ($s$), and *bottom* ($b$) quarks have a charge of $-1/3e$. Like the leptons, the quarks are ordered in flavour doublets of increasing mass;

$$\begin{pmatrix} u \\ d \end{pmatrix}_L, \quad \begin{pmatrix} c \\ s \end{pmatrix}_L, \quad \begin{pmatrix} t \\ b \end{pmatrix}_L \tag{2.3}$$

The gluon is a massless spin-1 boson with no electric charge, and it comes in eight different double-colour states which are combinations of one colour and another anticolour (e.g. green-antiblue). As gluons themselves are colour-charged, they have self-interactions. This restricts the range of the strong force to the size of a nucleus, in spite of the gluons being massless.

The gluon self-interactions also cause the strong coupling constant $\alpha_s$ to increase with increasing distance. In effect, quarks are bound in colour-neutral states and can not be observed freely, as originally postulated. This effect is called *confinement*. Equivalently, $\alpha_s$ decreases with decreasing distance, meaning that they are nearly free at distances smaller than the size of a hadron, as originally observed - an effect called *asymptotic freedom*.

The evolution, or *running*, of $\alpha_s$ with distance can equivalently be expressed in terms of the the energy scale $\mu$ at which it is probed:

$$\alpha_s(\mu) = \frac{12\pi}{(32 - 2n_f)\ln\frac{\mu^2}{\Lambda^2_{\mathrm{QCD}}}} \tag{2.4}$$

Here $n_f$ is the number of quarks flavours relevant at the energy scale $\mu$. The reference scale $\Lambda_{\mathrm{QCD}}$ is experimentally determined to be around 250 MeV. Measurement of $\alpha_s$ are compared to the theoretical predictions in Figure 2.2.

The running of $\alpha_s$ leads to a complex phenomenology which examined in Section 2.2.

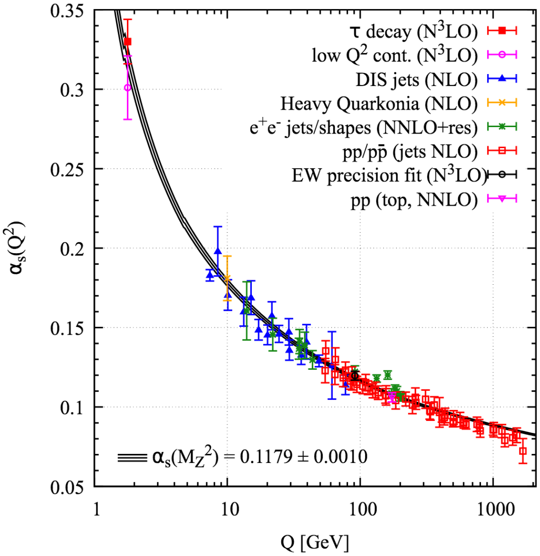

**Figure 2.2:** Measurements of the strong coupling constant as function of momentum transfer $Q$ [16].

### 2.1.4 The Higgs mechanism and electroweak symmetry breaking

All particles are predicted to be massless in electroweak theory. The terms which would give mass to gauge bosons violates the local symmetry of the underlying theory. The Brout-Englert-Higgs (BEH) mechanism was theorised by Robert Brout, François Englert [17], and Peter Higgs [18] in 1964 and incorporated into the electroweak theory by Steven Weinberg and Abdus Salam to give masses to gauge bosons and fermions while preserving the local gauge symmetry.

The problem is solved by introducing a quantum field, the *Higgs field*, which permeates all space. Interactions with the Higgs field causes a spontaneous symmetry breaking of the $SU(2) \otimes U(1)$ gauge group which describes electroweak interactions. The resulting symmetry is a $U(1)$ gauge group, which is identified as electromagnetism. Independently, the $SU(2)$ group has one neutral and two oppositely charged bosons, and the $U(1)$ group one neutral boson - all of which are initially massless. The electroweak symmetry breaking introduces a mixing between the two neutral generators whereby the massive $Z^0$ and the massless $\gamma$ bosons are formed. Likewise, the charged generators combine to the two massive bosons $W^{\pm}$.

The fermions of the Standard Model in turn acquire mass through Yukawa coupling with the Higgs field. Yukawa coupling are special in the context of the Standard Model, as the coupling strength is proportional to the particle mass. Or rather, the masses are given by how strongly the particle couples to the Higgs field.

Peter Higgs predicted that the quantum excitation of the Higgs field leads to a spin-0 particle, later called the Higgs boson. Until 2012 this was the last remaining prediction of the Standard Model yet to be discovered. The mass of the Higgs boson is a free parameter in the Standard Model, but has been measured to be around 125 GeV [19].

### 2.1.5 Symmetries and conservation laws

According to Noether's first theorem, every continuous symmetry of a physical system corresponds to a conservation law. The theorem also applies to the Standard Model, where the conservation law that arise from a symmetry are thought to be exact laws. These include:

- Time invariance → Conservation of energy
- Translation invariance → Conservation of momentum
- Rotation invariance → Conservation of angular momentum
- Lorentz invariance → Conservation of charge, parity, and time reversal, combined

- Gauge invariance → Conservation of electrical charge
- SU(3) Gauge invariance → Conservation of colour charge
- SU(2) Gauge invariance → Conservation of weak isospin

The conservation laws of the Standard Model function as theoretical safe guards which prevent stable particles from decaying: Unless the decay is prohibited by a conservation law, all particles will decay to a lighter particle. From the missing observation of certain decays, we can infer additional conservation laws which may be only be approximately true.

Based on the observation that the electron is stable, we say that the lepton number $L$, defined as the number of leptons minus antileptons, is conserved. Similarly, the stability of the proton, tells us that the baryon number $B$, defined as $B = (-)1$ for (anti)baryons and $B = (-)\frac{1}{3}$ for (anti)quarks, is conserved. But baryon number $B$ and lepton number $l$ are assumed to be conserved, because the violation of these quantum numbers have not been observed so far, not because of a fundamental symmetry.

## 2.2 Phenomenology of QCD

The properties of QCD lead to a rich and complicated phenomenology, which is especially relevant at hadron colliders. We have already learned that quarks are bound in hadrons which are colour-neutral, due to colour confinement. The most typical types of hadrons are *mesons* and *baryons*. Mesons are composed of two quarks with colour and anticolour (for example green-antigreen). Baryons are composed of three quarks, one of each (anti)colour (for example red-green-blue). The protons and neutrons that make up the nuclei of all atoms around us, are examples of baryons. Where protons consist of two up quarks and one down quark, giving the proton a net electrical charge of $+1e$, neutrons have two down quarks and one up quarks, making it electrically neutral.

In the previous section, we also learned that asymptotic freedom means that quarks are loosely bound at very small distances, well inside the hadrons. So what happens when we collide two protons at high enough energies to resolve such tiny distances? That's what we will explore in this section.

### 2.2.1 Parton distribution functions

Before we can make any predictions of what will happen in a proton-proton collision, we need a way to describe the initial state of the protons before the collision. Though we just established that protons consist of three quarks, the *valence quarks*, they are also flooded with, so-called, *sea quarks*. Sea quarks and gluons appear by quantum fluctuations inside the protons. When two protons collide at TeV scale energies, it is in fact the individual quarks and gluons, the *partons*, that are interacting. Parton distribution functions (PDFs) describe the initial state of the proton in terms of these partons.

Since the proton is a composite object, the proton momentum is in fact carried by both valence quarks, sea quarks, and gluons. Due to asymptotic freedom, the parton motion is unrestricted in all directions inside the proton, but the net effect gives overall proton momentum. The PDF describes how the overall momentum is divided between the various quarks and gluons within the proton.

The PDFs can not be computed from first principles, but are typically obtained by fitting a large number of measurements from experiments such as deep inelastic scattering of electrons off protons. Figure 2.3 shows the longitudinal momentum fraction $x$ times the PDF $f(x,Q)$, as a function of $x$, measured at momentum transfer scale of $Q = 2\,\text{GeV}$ and $Q = 1000\,\text{GeV}$. The distributions show that at if a parton carries more than 20% of the longitudinal momentum, it is most likely a valence quark ($u$ or $d$) or a gluon. However, the valence quarks become less dominant at high $x$, when the proton is probed at larger momentum transfer $Q$.

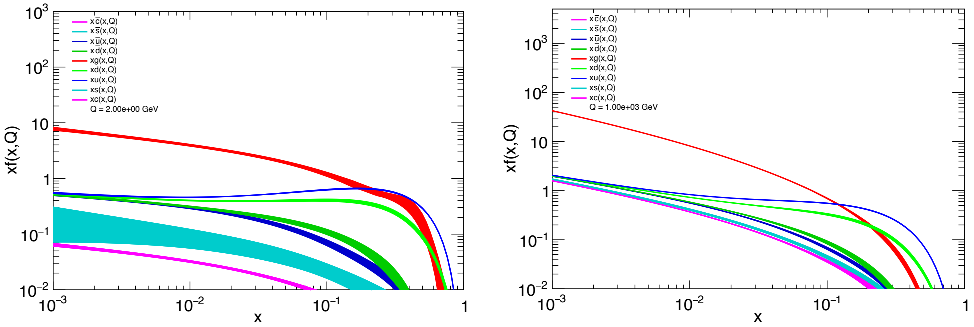

(a) (b)

**Figure 2.3:** Parton distribution functions showing the fractional distribution of momentum between (anti)quarks of the three lightest flavours and gluons. In (a) the PDFs are evaluated at $Q = 2\,\text{GeV}$ and in (b) they are evaluated at $Q = 1000\,\text{GeV}$. The plots are generated with APFEL 2.7.1 Web [20], using the PDF set, NNPDF2.3LO [21].

### 2.2.2 The hard scattering: Perturbative calculations and Feynman diagrams

Once the intial state of the protons is described, we can start to compute the probabilities for what may come out of the hard-scattering interaction of two partons in the proton-proton collision. This is also an appropriate time to introduce some mathematical tools and expressions that will come in handy later on.

For calculating high-energy particle interactions, we often rely on *perturbation theory*. In perturbative calculations a complicated problem is split into smaller parts of increasing precision, not unlike series expansions. We call the simplest perturbative approximation the *leading-order* calculation. Adding the higher-order corrections is called next-to-leading order (NLO) calculations, and even higher orders we call next-to-next-to-leading order (NNLO) and so on.

Perturbation theory in particle physics is more easily understood in terms of *Feynman diagrams*. They are graphical representations of particle interactions, and powerful tools for calculating and understanding interaction probabilities. As a very simple example, we can look at $e^+e^-$ scattering. Figure 2.4 illustrates two paths through which a positron (anit-electron) scatters off an electron by the exchange of a photon.

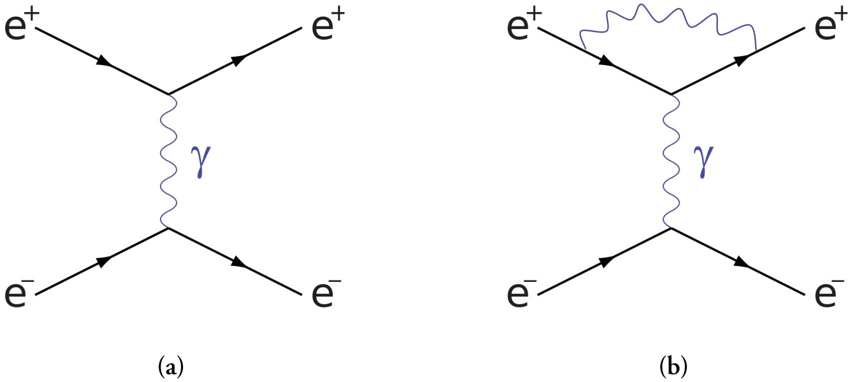

(a) (b)

**Figure 2.4:** Feynman diagrams of $e^+e^-$-scattering. A treel-level diagram is shown in (a) and a NLO correction is shown in (b).

The additional gamma emission by the incoming positron, occuring in Figure 2.4b, could in principal happen anywhere on the diagram, and we wouldn't be able to tell the difference on the final state. In fact, there are infinite ways, more or less complicated, an $e^+e^-$ pair can end up as an $e^+e^-$ pair. To calculate the total probability, the *cross section*, for $e^+e^-$ scattering we should in principle add together the probability for all these possible paths, taking their quantum mechanical interference into account. This would, of course, take a huge amount of computing resources, but luckily we don't need to.

To leading order in perturbation theory, we only take into account the *tree-level* diagrams - the ones that only have two *vertices*, like the one in Figure 2.4a. In order to go to NLO in perturbation, we need to add all the Feynman diagrams with four vertices, like the one in Figure 2.4b. But the perturbative approach only works if the coupling is small enough.

This is because each vertex in the Feynman diagram represents an coupling with a coupling strength. The probability of the Feynman diagram scales with the product of the couplings. So, if the couplings are smaller than one, every additional vertex in the Feynman diagram decreases the probability for that path.

In the case of QCD processes, the strong coupling satisfies $\alpha_s \ll 1$ for momentum transfers of $Q > 1$ GeV. This is well below the center-of-mass energy of the proton collisions at the LHC. Therefore, perturbative calculations can be used for computing cross-sections of the hard-scattering interaction which, by definition, involves a large momentum transfer. The processes that happen before and after the high-energy collision can occur at much lower scales, and must be treated differently. One example is the PDFs which we already learned can not be calculated from first principles, but must be determined phenomenologically [1]. Fortunately, the different stages are independent of each other - they are *factorisable* - which basically means we can compute the probabilities at each stage separately and multiply them in the end.

### 2.2.3 Shower formation

The partons involved in the hard-scatter interaction are violently accelerated. Similarly to Bremstrahlung, where accelerated electric charges deposit energy by emitting photons, accelerated colour charges deposit energy by emitting gluons. Since the gluons themselves also carry colour charge, they can emit further radiation, thereby creating what we call a *parton shower*. The showering causes the parton to loose energy. As the energy reaches the regime where confinement rules, $Q < 1$ GeV, the showering stops. The partons can no longer be considered free particles and must form hadrons.

Though the parton shower could, in principle, be computed perturbatively as higher-order corrections to the hard-scatter interactions, this approach is not practically feasible. Instead, the shower formation can be approximated by considering only the dominant contributions which are mainly collinear parton splittings and soft gluon emissions.

### 2.2.4 Hadronisation

The property of colour confinement in QCD means that coloured objects, quarks and gluons, can not propagate freely. As a consequence, any outgoing parton created in the hard scattering process must *hadronise* in order to veil it self as an uncoloured object at distances larger than the proton radius. This transformation can not be treated in perturbative QCD

---

[1] Though the PDFs can not be calculated from first principals, it is possible to derive the PDF at one value of $Q$ given a measurement at another value of $Q$. This can be done using Dokshitzer-Gribov-Lipatov-Alterelli-Parisi (DGLAP) equations, which are valid in the perturbative regime ($\alpha_S << 1$) [22].

since the strong coupling $\alpha_{\rm s}$ is too large. Instead we rely on models to make predictions about the observed final state.

There exist several alternative ways of modeling the hadron formation. The main ones can be categorised as *string* or *cluster* hadronisation.

String models are based on the dynamics of the colour flux stretched between the original quark/antiquark pair. The self-interaction of gluons causes the colour field lines between the quarks to be compressed into a tube-like region of strong colour field. In the *Lund String Model* [23] the force between two outgoing quarks is treated as a classical string, where the potential increases linearly with the distance between the quarks. At a certain distance it becomes more economical to break the string by creating a new quark-antiquark pair than to further stretch the string. The original and the new quark pair form two new strings which then stretch and break in to more quark pairs. The process continues until all the potential energy is converted to quarks, which are connected to each other by small gluon strings - in other words *hadrons*.

In cluster models [24], the gluons produced in the parton shower are split non-perturbatively to quark-pairs, $g \to q\bar{q}$. The $q\bar{q}$ combine to form colour-singlet clusters, which undergo simple isotropic decay into lighter clusters or pairs of hadrons. The decays are determined by the available phase-space, such that the production of baryons and heavy quarks is suppressed.

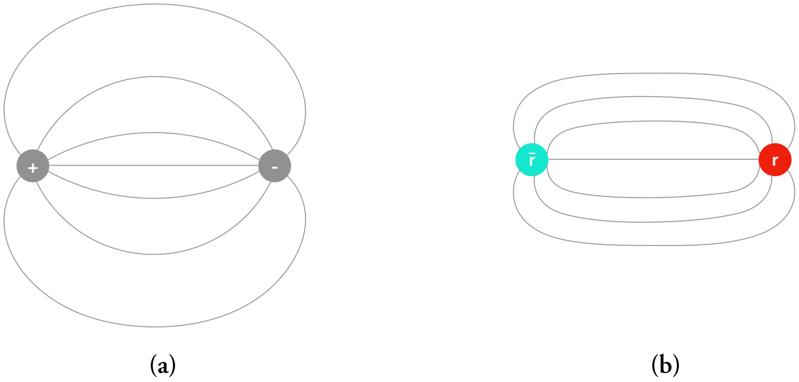

(a) (b)

**Figure 2.5:** Illustration of electric field lines (a) and colour field lines (b).

If the energy of the original parton is large, the gluon emissions during the showering phase are more likely to be aligned with the original parton. In this case, the hadronisation results in a spray of hadrons which we call a *jet*. The experimental definition of a jets is described in Chapter 4.

Hadronisation happens at much larger time-scales than the hard interaction and, therefore, does not affect the hard scatter cross sections. Still, the process must obey the conservation laws, making jets a useful signature for studying QCD; by measuring the jet properties we directly gauge the properties of the original parton although we can not observe it directly.

### 2.2.5 Underlying event

In the complex system that is a high-energy proton-proton (*pp*) collision, there is always a lot more going on than just the hard-scatter interaction between two partons. Where the term *hard-scattering* refers to the most energetic of the parton interactions, all the other hadronic activity is called the *underlying event*.

Part of the underlying event comes from interactions between the proton remnants of the collision. When a coloured parton is knocked out of a proton, the proton itself also acquires colour. Similarly to the hadronisation of hard-scattering partons, the proton remnants form gluon field lines between them, which break into hadrons.

Additional contributions can come from *multiple parton interactions*, where more than one parton of each proton can interact during the collision.

Partons that are produced and accelerated in the underlying event also shower and hadronise, and thereby add noise to the picture of the hard-scatter interaction. But the underlying event predominantly produces soft and diffuse radiation on top of which, jets from the hard interaction can be distinguished.

## 2.3 Simulation of *pp* collision

It should now be clear, that a proton-proton collision is a highly complex and indeterministic process. Not only is there a near-infinite number of possible interactions which can occur in the hard-scattering, but also the initial state of the protons and processes following the collision are probabilistic by nature. Even from looking at the data of an single collision, we can not deduce exactly what happened. For this reason, one of the key ingredients in particle physics is calculating probabilities and comparing distributions.

Even though the cross-section of a simple scattering process can be calculated by hand to leading order, it would not be feasible to compute the probabilities of every possible combination of interactions that might occur in the billions of collisions produced daily at the LHC. In order to make theoretical predictions, we rely on Monte Carlo (MC) methods to mimic the stochastic nature of the processes by sampling probability distributions with the use of pseudorandom number generators. With MC simulations we can generate huge numbers of collision events to which we can compare the data.

Various software programs typically go into the production of *pp* collision simulations, each performing a different task. General-purpose event generators are capable of producing the hard-scatter interaction as well as the parton shower, hadronisation, and the underlying event. Examples of these include PYTHIA [25], HERWIG [26], and SHERPA [27]. Matrix element generators are specialised in computing cross-sections of the hard-scattering interactions only, but can provide these calculations to higher orders. Examples of these are MADGRAPH5_aMC@NLO [28] and POWHEG-BOX V2 [29].The generated final-state particles are then propagated through a detailed detector simulation based on GEANT 4 [30].

A large number of free parameters enter in the simulation of the non-perturbative processes, parton showering, hadronisation and the underlying event. Their values must be determined from experimental data for a given parton density function through an optimisation known as tuning. The resulting set of parameters is called the *generator tune*, and can be optimised for specific observables of interest.

With the high proton beam intensity of the LHC, several protons are typically colliding simultaneously. These collisions induce additional interactions, called *pile-up*, on top of the hard-scatter and the underlying event. Contributions from pile-up are accounted for by generating events that satisfy very loose triggers with as little bias as possible, called *minimum bias* events. For each simulated hard-scatter event, a number of minimum bias events are overlaid to match the distribution of the average number of simultaneous collisions, as observed in collision data. The simulated events are then assigned a weight according to the relevant pile-up conditions. Finally, the full events (consisting of the hard-scatter and pile-up) are propagated through the detector simulation, reconstructed, and calibrated in the same way as data, see Chapter 5.

## 2.4 Physics Beyond the Standard Model

Since its creation, the Standard Model (SM) has proven to be an incredibly robust description of the subnuclear world. Nearly all theoretical predictions given by the Standard Model have, in time, been confirmed by experiments, and nearly all experimentally observed phenomena can be explained by the Standard Model. There are, however, a few exceptions to the successes, which let us know that the Standard Model can not be the full story.

The theoretical rationale for expecting that a more complete theory of nature exists, is prompted by the many questions left unanswered by the Standard Model: Why is the weak force $10^{25}$ times stronger than gravity, why are there exactly three fermion generations, and why are there such large variations between the particle masses? The answers to these questions might lead the way to a unified theory of all four forces, incorporating gravity as described by general relativity.

In addition to the theoretical questions posed above, there is a number of observed phenomena to which the Standard Model offers no explanation. These serve as observational evidence of physics *beyond* the Standard Model, or just "BSM physics".

### 2.4.1 Empirical evidence of BSM physics

Neutrino masses provide the only experimental contradiction to the Standard Model. Though neutrinos do not interact with the Higgs field, their observed ability to oscillate between flavour states without any interaction, requires at least two non-zero mass states. Neutrino masses can be incorporated into the Standard Model in different ways, but which is the correct one depends on whether neutrinos are Dirac or Majorana particles, and this is still unknown [31].

Another undeniable and severe problem of the Standard Model, is that it treats particles and antiparticles on an equal footing. According to both theory and observations, particles are always created along with their antiparticles and annihilate in such pairs as well. It is natural to assume that this was also the case in the early Universe when matter started to form. Therefore, there ought to be equal amounts of matter and antimatter in the Universe or nothing left at all. However, the fact that we exist to ask why, implies that there is now mostly matter, and almost no antimatter left. An explanation of this so-called *baryon asymmetry* requires three conditions as identified by Sakharov in 1967 [32]. One condition is the existence of processes which can violate baryon-number conservation. In addition, the laws of nature must in some way favor matter, and thereby violate charge-parity (CP) conservation. While baryon-number violation has never been observed, CP-violation does occur e.g. in the weak decay of kaons. Unfortunately, electroweak CP-violation in the Standard Model is to small an effect to generate the required difference of one additional particle per billion particle-antiparticle pairs.

Finally, a spectacular shortcoming of the Standard Model is the its inability to describe all the matter content of the Universe. Throughout the past $\sim 100$ years, numerous independent astronomical observations have confirmed that the particles we know from the SM only make up about 15% of the total matter content of the Universe. The remaining 85% we do not know the nature of, and have no candidate particle for in the SM. It goes by the common name of *dark matter*.

### 2.4.2 Dark matter

The hypothesis of dark matter (DM) can be dated back all the way to 1884 where Lord Kelvin estimated the number of dark bodies in the Milky Way from the observed velocity dispersion of the stars orbiting around the center of the galaxy. The term was coined by the Swiss astrophysicist, Fritz Zwicky, who noticed a large gravitational anomaly by studying the motion of galaxies near the edge of the Coma Cluster. Further indications, that luminous matter only makes out a small part of the mass of galaxies came from measurements of galaxy rotation curves. The need for dark matter was fortified around 1980 when Vera Rubin and Kent Ford showed from rotation curves that most galaxies contain about six time more dark than luminous matter. However, the possibility that the discrepancy could be caused by an unknown astronomical phenomenon, or that the theory of gravity, General Relativity, does not apply at all scales, still remained [33].

Today the list of observational evidence of dark matter is much longer. A few examples are shown in Figure 2.6, and short explanations of each figure is given below:

- **Rotation curves** show the velocities of stars as function of their distance from the galaxy center. The green dots in Figure 2.6a show the observed velocities, while the orange line illustrates the velocities that would be expected from the mass of the luminous disk. The rotation curve of M33 and many other galaxies imply that the mass of the galaxies extend way beyond the galactic disks we can see. An explanation could be that the galaxies are surrounded by a much bigger dark matter halo.
- **The Bullet Cluster**, is formed by the collision of two galaxy clusters. The pink regions in Figure 2.6b correspond to the location of hot gas, detected as X-rays. The blue regions indicate the concentration of mass as inferred by gravitational lensing - a method to locate and measured mass by seeing how light from a distant source is bended. The image shows that the mass is not primarily centered around the luminous matter, which could be explained if the clusters contain a large amount of dark matter which only interacts weakly with itself and ordinary matter.
- **The cosmic microwave background (CMB)** is low energy electromagnetic radiation coming from all directions of the universe, as it was created in the early Universe when atoms formed. In Figure 2.6c, the measured data points are shown in red along with predictions assuming different compositions of the total energy content in the universe. The most accurate prediction is given by fraction of baryonic matter $\Omega_b \sim 5\%$ and dark matter $\Omega_{\mathrm{dm}} \sim 22\%$. The remaining $67\%$ is ascribed to *dark energy* - an even more mysterious substance than dark matter.

By independent approaches, gauging the matter content at vastly different scales, the dark matter density is consistently found to be roughly five times larger than the visible matter.

Theories of new astrophysical phenomena or modified gravity struggle to explain all the various observations. Therefore it is now widely accepted that one or more new particles is required for a complete explanation.

The particle explanation implies that millions of dark matter particles must pass through any square centimeter of the Earth at any second. Since these particles have yet escaped detection, except through their gravitational effect, they must interact very weakly with known matter, if at all. Many experiments aim to test different dark matter hypothesis via other interactions. Most of them fall into one of three categories: Direct detection, that look for low-energy recoils of nuclei which could be induced by an interaction with a neutrino passing through the Earth. Indirect detection, which look to the sky for products of either decay or self-annihilation of dark matter. Finally, accelerator experiments aim to produce dark matter and typically try to detect it as missing energy escaping the detector.

#### 2.4.2.1 Dark matter candidates

One would hope that the Standard Model neutrino, being stable, neutral, and weakly interacting, could actually make out the dark matter. It would certainly have been neat if Pauli's "desperate remedy" [35] eventually had prevented future physicist from postulating another, potentially unmeasureable, new particle. Unfortunately, neutrinos are too light to account for more than a small fraction of dark matter abundance and too relativistic to give the structure formations we see in the Universe.

Therefore, most BSM theories contain at least one hypothesized particle which could work as the dark matter - a dark matter candidate. Many of them can be catergorised under the broad term of Weakly Interacting Massive Particles (WIMP). WIMPs are typically expected to have been produced in the early universe and could provide the observed DM abundance with a mass at the order of 100 GeV and interaction strengths of the same order as the weak force. A particle with these properties would be possible to discover at the LHC, which is part of the reason WIMPs have long been the favored candidates. However, the absence of evidence for WIMPs at the LHC and other experiments,so far, have prompted physicist to cast a wider net that looks beyond these BSM favorites.

Luckily, there is no shortage of dark matter candidates. For a complete review of various possible explanations, I refer the reader to this review article [34]. The remaining part of this section, will focus on two categories of BSM theories that are particularly relevant for this thesis.

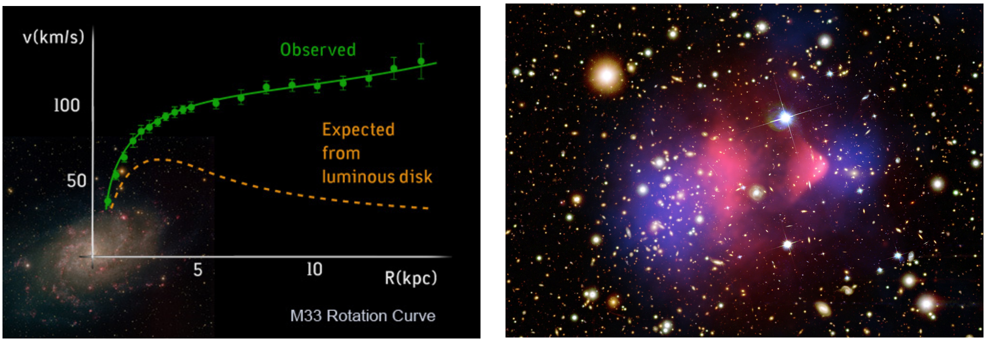

(**a**) Rotation curve of the M33 galaxy. The green dots show the observed velocities, while the orange line illustrates the velocities that would be expected from the mass of the luminous disk.

(**b**) Composite image of the "bullet cluster", taken by the Chandra X-ray observatory. Pink regions correspond to the location of hot gas, detected as X-rays. Blue regions correspond to concentration of mass, inferred by gravitational lensing.

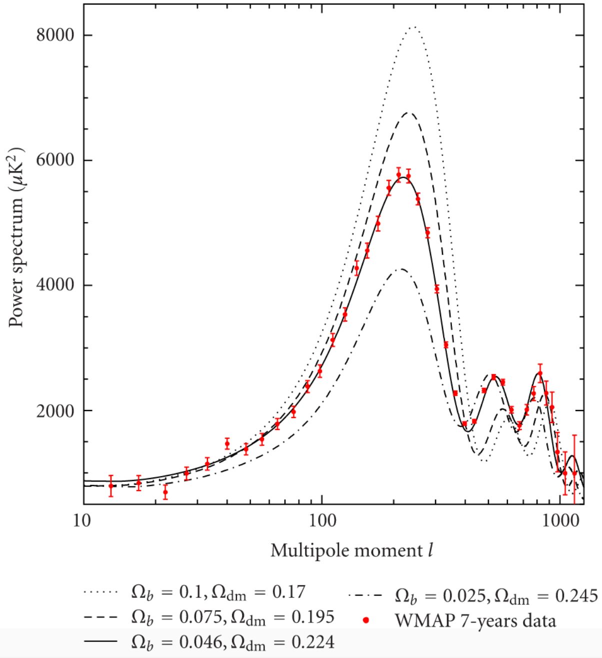

(**c**) The power spectrum of the cosmic microwave background (CMB), measured by WMAP. The measured data points are shown in red along with predictions assuming different compositions of the total energy content in the universe. [34]

**Figure 2.6:** Selection of observational evidence for dark matter.

### 2.4.3 Supersymmetry

Supersymmetry is a class of extensions to the Standard Model which were originally proposed in the 1970s [1]. By imposing a new type of symmetry between fermions and bosons, supersymmetry offers explanations to both the Higgs mass and the Hierarchy problem and provide a dark matter candidate. These features along with certain mathematical properties makes supersymmetry theoretically well-motivated.

In supersymmetry (SUSY) every SM fermion has a boson superpartner and vice versa, such that the particle content is roughly doubled. The naming convention of the superpartners follows a simple scheme. Superpartners of of fermions, the *sfermions*, are named by adding a *s* to the SM fermion name, e.g. *selectron*. The superpartner to SM bosons are named by adding *-ino* to the end of the boson name. For example, the gluon superpartner is called the *gluino*. The Standard Model particles and their superpartners are arranged in chiral *supermultiplets*. An overview of the Standard Model particles along with their supersymmetric partners is shown in Figure 2.7.

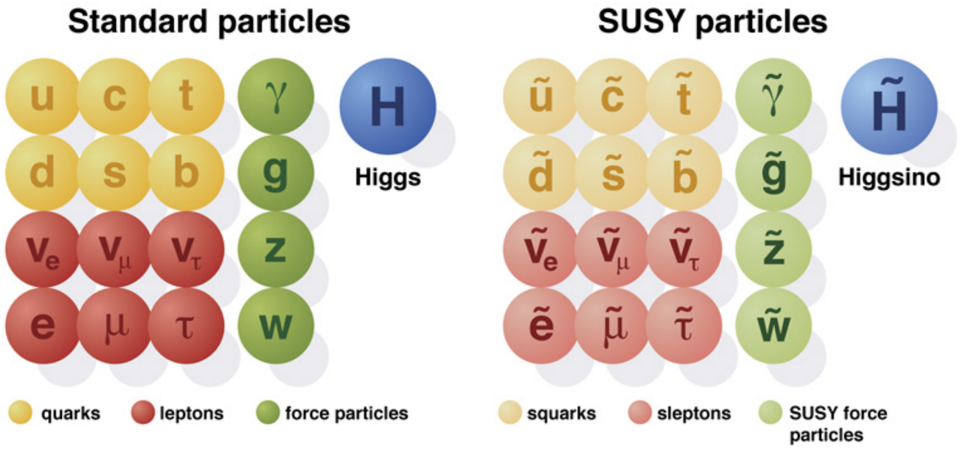

**Figure 2.7:** Illustration of the ordinary Standard Model particles along with their proposed supersymmetric partners. The additional Higgses and the mixings between the hissinos and electroweak gauginos are left out for simplicity. Image by CERN.

The superpartners have the same quantum numbers except for the spin which differs by $\frac{1}{2}$. In the simplest supersymmetry theories, each superpartner would also share the same mass. Since we have not observed supersymmetric particles at the masses of the Standard Model, supersymmetry must be spontaneously broken, if it exists. Supersymmetry and the WIMP-paradigm lend additional motivation to each other, because many supersymmetric extension to the Standard Model readily predict WIMP-like particles. Specifically, the lightest stable SUSY particle (LSP) could well have the properties of a WIMP with a mass around the GeV- to TeV-scale. This apparent coincidence is know as the "WIMP miracle" and has long caused the LSP to be the prime dark matter candidate.

The simplest possible supersymmetric extension to the Standard Model, is called the *Minimal Supersymmetric Standard Model* (MSSM). It includes only the necessary new particles and has been shown to solve the hierarchy problem. The particle spectrum of the MSSM includes those particles shown in Figure 2.7, but the full picture is slightly more complicated. There are two complex Higgs doublets, resulting in two fermionic Higgsino doublet partners. The higgsinos mix with the electroweak gauginos to form four mass eigenstates called *neutralinos* and two mass eigenstates called *charginos*. In total the MSSM predicts 32 mass eigenstates corresponding to new particles.

In the MSSM baryon number and lepton number are not strictly conserved by all couplings. Since baryon number and lepton number conservation have been tested very precisely, these couplings would need to be very small in order to explain the stability of the proton. Therefore, a new symmetry called *R*-parity is imposed on the MSSM fields which forbids these couplings. The definition of *R*-parity is

$$P_{\mathrm{R}} = (-1)^{3B+L+2s} \tag{2.5}$$

where $s$ is spin, $B$ is baryon number, and $L$ is lepton number. The Standard Model particles all have $P_{\mathrm{R}} = 1$ and the SUSY particles all have $P_{\mathrm{R}} = -1$.

An enforced conservation of *R*-parity means that the lightest supersymmetric particle can not decay. Therefore, the possibility of supersymmetric dark matter is closely related to the concept of *R*-parity.

#### 2.4.3.1 *R*-parity violating SUSY

Enforcing conservation of *R*-parity serves the purposes of protecting the proton from decaying and providing a dark matter candidate. However, the invariance is introduced by hand and not as a result of a fundamental logic. Though strong constraints are imposed by the proton life time on the possible strength, small *R*-parity violating (RPV) couplings are, in principle, allowed. In fact, *R*-parity violations could even appear as a desired feature, since they may provide a source of Majorana masses for neutrinos. [36]

A general and gauge-invariant MSSM Lagrangian would include the terms

$$W_{\Delta L=1} = \frac{1}{2}\lambda^{ijk} L_i L_j \overline{e}_k + \lambda'^{ijk} L_i Q_j \overline{d}_k + \mu'^{i} L_i H_u \tag{2.6}$$

$$W_{\Delta B=1} = \frac{1}{2}\lambda''^{ijk} \overline{u}_i \overline{d}_j \overline{d}_k \tag{2.7}$$

where the indices $i, j, k$ refer to the generations. The objects $L, \overline{e}, Q, \overline{u}, \overline{d}$, and $H_u$ correspond to chiral supermultiplets, which represent left-handed leptons and sleptons ($L$), their right-handed conjugates ($\overline{e}$), left-handed quarks and squarks ($Q$), their right-handed up- and down-type conjugates ($\overline{u}, \overline{d}$), and the Higgs and Higgsinos of weak hypercharge $Y = 1/2$ ($H_u$). The couplings $\lambda$, $\lambda'$, and $\lambda''$ all violate *R*-parity. The terms in equation 2.6 violate lepton number and the terms in equation 2.7 violate baryon number.

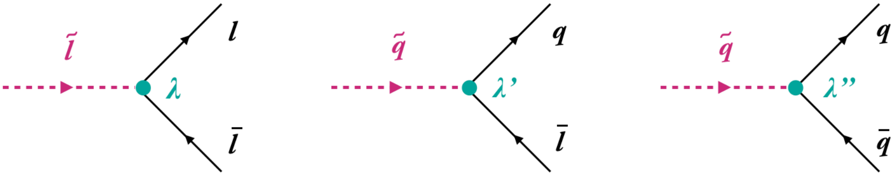

**Figure 2.8:** Basic tree-level diagrams illustrating *R*-parity violating interactions. Lepton number is violated by $\lambda$ and $\lambda'$ couplings, and baryon number by $\lambda''$ couplings.

If both $\lambda'$ and $\lambda''$ were present, the proton life time would be much too short. Therefore, either Baryon-violating or Lepton-violating couplings are allowed, but not both. Depending on the strength of the RPV couplings, the life time of the LSP can be anything between prompt and long-lived. If the life time is long enough, the LSP could still be a dark matter candidate. More information on RPV supersymmetry can be found in the review article [37].

The experimental signatures of RPV SUSY could be dramatically different than those expected of the MSSM. Firstly, RPV couplings allow for single-particle production of SUSY sparticles in addition to the usual pair-production. Secondly, the potential decays of sparticles, particularly the LSP, to SM particles, means that the final states of RPV processes could be visible in the detector as more than just missing transverse energy. Depending on the strength of the RPV coupling, and hence the typical decay length, various signatures are possible: prompt decays will give signals similar to those of SM processes, long lifetimes will lead to missing transverse energy, just like the *R*-parity conserving case, and intermediate decay lengths could lead to long-lived particle signatures, such as displaced tracks and vertices. As a consequence, individual SUSY searches must be tailored to each of the many possible scenarios for *R*-parity violating and conserving supersummetry.

### 2.4.4 Hidden sectors and asymmetric dark matter

If known particles, with all the complexity of the Standard Model, only make out 15% of the Universe matter content, there is no reason to assume that the remaining 85% is necessarily made up of one single fundamental particle. While a single particle would be the simplest explanation, the persistent lack of experimental signs, has promoted models of more complex dark, or *hidden*, sectors. Such scenarios arise from many "top-down" theories, where the phenomenology is derived from a set of cherished principles, like unification or naturalness. Similarly to supersymmetry, constructions of string theory and grand unification theories also require large symmetry groups which imply several new particles.

Hidden sector (also sometimes called *hidden valley*) models share the common premise that dark matter resides in a hidden sector with its own rich dynamics, potentially giving rise to multiple states and forces. The hidden sector may communicate with the visible sector through a heavy mediator with a mass around the TeV scale or beyond.

The idea of hidden sectors intuitively seems likely, due to the sheer size of the DM abundance, but additional motivation is given by the fact that the DM and baryonic abundances are so similar, $\Omega_D \sim 5\Omega_B$. In WIMP models, the DM mass is set by the electroweak scale and the number density by the thermal freeze-out mechanism. The baryon masses, however, are related to the QCD confinement scale, and the number density is set by CP-violating parameters. Thus, the DM and baryon abundance are determined by unrelated dynamics in the WIMP paradigm, and the similarity comes out as a coincidence. By contrast, the similar abundances can be explained by combining the idea of a confining hidden sector with the framework of asymmetric dark matter (ADM) [38]. In ADM models the DM number density is also set by an asymmetry between matter and antimatter, that is governed by the same physics as the baryon asymmetry. If the dark matter arises from a hidden sector with a strong dynamics similar to the SM QCD, where the asymmetry is shared between the sectors through some portal, the similar abundances come out naturally. The dark matter would in such case be charged under a hidden gauge group $SU(N_d)$, causing confinement at a scale $\Lambda_d$. Further support for considering dark matter with strong interactions, comes from a number of astrophysical discrepancies between observations of dark matter halos on subgalactic scales and the predictions of the standard "cold dark matter" picture [39]. On the contrary, cosmological simulations of dark matter halo densities and substructure dark matter with large self-interactions [40] [41] [42] [43], which is naturally obtained if dark matter is a stable, composite particle from a confining hidden sector, in other words a dark hadron.

#### 2.4.4.1 Phenomenology of "dark QCD"

The signature of a hidden sector, charged under a confining gauge group, also called "dark QCD", could well be distinguishable at collider experiments. If a dark parton is produced with an energy larger than the confinement scale, it will shower and then hadronise to a cluster of dark hadrons, consisting mainly of light mesons. These may then decay back to visible SM particles, forming what we refer to as "dark jets". Each of these steps depends on the underlying parameters of the hidden sector and the portal(s) between the hidden and SM sector, thus dark QCD can result in a variety of different phenomenologies.

Similarly to SM QCD, a dark QCD sector may include multiple hadronic states with a hierarchy of life times. Some may be stable to the full extent of our detector or beyond. We say they are *collider stable* (C.S.). Others may decay to SM particles in the detector at a measureable distance from the collision point. Particles with such a property are generally called *long-lived particles*. Finally, some hadrons may decay promptly, at distances we can not resolve.

The features of a dark jet is largely determined by its composition of long- and short-lived hadrons. Various possible scenarios are illustrated as four different types of dark jets in Figure 2.9. The categorisation is based on the amount of stable (invisible) dark hadrons in the jet and the life time of the dark hadrons that decay to SM particles:

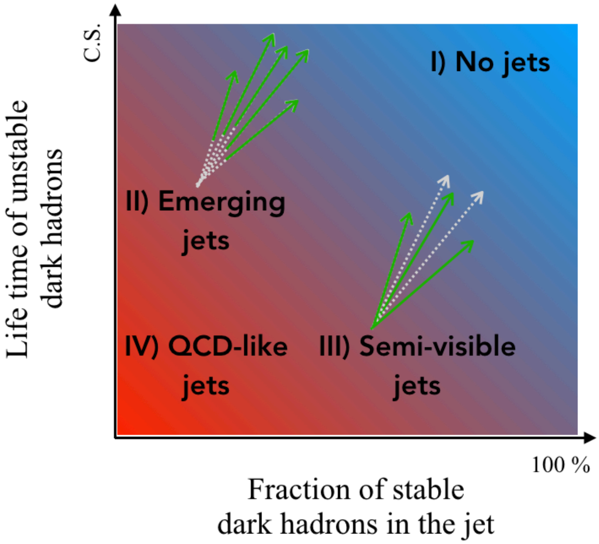

**Figure 2.9:** Illustration of different dark QCD scenarios, modified from [44]. The models are categorised according to the percentage of stable (hence, invisible) dark hadrons in the dark jet and the life time of the dark hadrons decaying to SM particles. In the sketches of jets, visible SM particles are depicted with full, green arrows and stable or collider stable (C.S.) particles with light grey dashed arrows.

I If most or all of the dark hadrons are collider stable, there are no jets to be seen, unless formed by initial state radiation. These models could therefore result in events with large missing transverse energy, resembling events where a WIMP is produced. These types of signatures are extensively covered by the ATLAS physics program. For example by the mono-jet search [45] which uses events where missing transverse energy is balanced against a single jet, and could therefore also be sensitive to this type of dark QCD.

II If the dark sector creates long-lived dark mesons, that decay to SM particles with a life time smaller than the size of the detector, the jets would seem to appear in the detector displaced from the primary vertex. Depending on the life time and invisible fraction, we could either see jets emerge in the calorimeter without any tracks pointing back to the primary vertex, jets with multiple displaced vertices inside, or, if the invisible fraction is large, just a few displaced vertices. The latter case is largely covered by the various searches for long-lived particles (LLPs) at ATLAS and CMS [46], and an ATLAS search for emerging jets is currently in development.

III Models where only a fraction of the dark hadrons decay promptly to SM particles predict dijet events where some amount of missing transverse energy is aligned with one of the jets. Such "semi-visible" jets are proposed in [47] and a further investigation of their phenomenology is presented in [48]. An ATLAS search for this signature is currently in development.

IV If all or most of the dark hadrons decay promptly to SM particles, the dark jets will look a lot like SM QCD jets. Identification based on displaced vertices or missing transverse energy becomes ineffective. However, such jets might be distinguishable from SM jets by studying the radiation pattern, or substructure, of the jets. Such properties could differ significantly if the colour factor or confinement scales differs between the SM and the hidden sector. An ongoing ATLAS analysis for this type of signature is presented in Chapter 8.

# Chapter 3

# The Experimental Tools

## 3.1 The Large Hadron Collider

The Large Hadron Collider (LHC) [49] is CERN's largest particle accelerator, measuring 27 km in circumference. It is located about 100 m under ground near the Swiss/French border. With two counter-rotating beams, bunches of either protons or heavy ions are brought to collision at four intersections along the ring. The LHC's primary objective is to generate proton-proton ($pp$) collisions at center-of-mass energy up to $\sqrt{s} = 14\,\text{TeV}$ for the four experiments located at the collision points, *ATLAS* [50], *ALICE* [51], *CMS* [52], and *LHCb* [53] [1].

### 3.1.1 Acceleration chain

Before protons are injected into the LHC they are accelerated in several stages, using previous generations of CERN accelerators. The injection chain starts from a Hydrogen source, where the molecules are stripped of their electrons by passing through a strong electric field. The resulting protons are initially accelerated up to 50 keV through a series of radio-frequency (RF) cavities in the linear accelerator, LINAC2. The alternating fields of the RF cavities ensure that particles arriving early experience a deceleration, where those that arrive late are accelerated. This has the two-fold effect that all particles get closer to the ideal energy, and the particles are arranged into *bunches*. The LINAC2 sends the proton bunches to the Booster, where they are brought to an energy of 1.4 GeV. From the Booster they go to the Proton Synchrotron (PS), where they are accelerated to 26 GeV, before they are

---

[1] The work presented in this thesis is based on proton collisions, and the cases of proton-lead and lead-lead collisions will not be discussed.

directed to the Super Proton Synchrotron (SPS). In the SPS the proton energies are further increased to 450 GeV, before finally being injected into the LHC. This injection chain is illustrated in Figure 3.1.

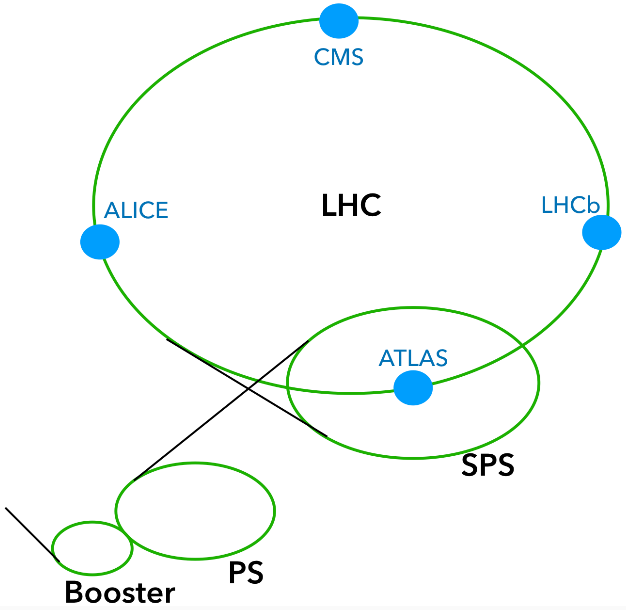

**Figure 3.1:** Sketch of the LHC injection chain. The protons begin at the linear accelerator (LINAC2), and go from there to the Booster, on to the Proton Synchrotron (PS), and then to the Super Proton Synchrotron (SPS), before finally getting injected into the LHC tunnel. The four large experiments on the LHC are marked with blue dots.

Once in the LHC, the beam is accelerated by eight RF cavities which also compensate for the energy lost to synchrotron radiation. With a maximum voltage of 2 megavolt per RF cavity, the beam energy is increased by 16 MeV per round trip in the LHC. Thus it takes more than 10 million round trips or about 20 minutes for the protons to reach the target energy of 7 TeV. The beam trajectory is bent to the same curvature as the beam pipe by 1232 superconducting dipole (or "bending") magnets. The current in the magnets increases as the protons are accelerating in order to keep the particles orbiting with the right radius. An additional 392 quadrupole magnets focus the beam to increase the number of collisions in the bunch crossings.

**Table 3.1:** Summary of the LHC operating parameters for Run-2.

| Parameter | 2015 | 2016 | 2017 | 2018 |
|---|---|---|---|---|
| Energy [TeV] | 6.5 | 6.5 | 6.5 | 6.5 |
| Number of bunches | 2244 | 2220 | 1868 – 2556 | 2556 |
| Protons per bunch [$10^{11}$] | 1.2 | 1.25 | 1.25 | 1.1 |
| Integrated luminosity [$\text{fb}^{-1}$] | 3.2 | 33.0 | 44.3 | 59.9 |
| Mean number of interactions per bunch crossing | 13.4 | 25.1 | 37.8 | 36.1 |

### 3.1.2 Run schedule

The LHC is designed to accelerate protons to 7 TeV, thus colliding them with a center-of-mass energy of 14 TeV. But to reach the design specifications of LHC, the run schedule is going through multiple running stages separated by periods of upgrading the accelerator and experiments, called shut-downs. During Run-1 (2011 to 2012) LHC was operating at energies of $\sqrt{s} = 7$ and 8 TeV with a spacing between the bunches of 50 ns. In Run-2 (2015 to 2018) the LHC was running at $\sqrt{s} = 13$ TeV with a bunch spacing of 25 ns. LHC is expecting to reach the target center-of-mass energy of 14 TeV with Run-3, where the bunch spacing will still be 25 ns, but the number of protons per bunch, or bunch intensity, will increase.

The results presented in this analysis are based on data taken in Run-2. The relevant operating parameters for this run is shown year by year in Table 3.1.

### 3.1.3 Interlude: Luminosity and pile-up

The number of protons per bunch and the frequency with which the bunches cross, determine how often two protons collide. Today the processes that often occur in *pp* collisions are generally well known and understood. It is the very rare events that are of most interest at the LHC, such as Higgs production which occurs in about one in a billion *pp* collisions.

By increasing the number of collisions we also increase the probability of seeing a rare event. Therefore, the possible extent of the experiments physics programs is limited not only by the center-of-mass energy, but by the amount of proton collisions the LHC can deliver.

A key concept for characterising the beam of a particle collider is the *instantaneous luminosity*, $L$, defined as

$$L = \frac{n_p n_b f \gamma}{4\pi\sigma_x\sigma_y} F \tag{3.1}$$

where:

- $n_p$ is the number of protons per bunch
- $n_b$ is the number of bunches in the ring
- $\gamma$ is the relativistic Lorentz factor of the protons
- $f$ is the revolution frequency
- $\sigma_x$ and $\sigma_y$ are the beam sizes in the $x$ and $y$ direction
- $F$ is a correction factor depending on the crossing angle of the beams at the interaction point

The instantaneous luminosity is defined like this to give the rate $R$ of some process with cross section $\sigma$ as:

$$R = L \cdot \sigma \tag{3.2}$$

Thereby the *integrated luminosity* can give us the number of times $N$ an event occurs within a time interval $\Delta T$ as

$$N = \sigma \int_{t}^{t+\Delta t} L dt \tag{3.3}$$

This means we can measure the integrated luminosity experimentally by measuring the number of times an event with a known cross section occurs. Conversely, if the integrated luminosity is well known, we can measure cross sections of known processes. Finally, knowing the integrated luminosity allows us to make predictions of the number of times a hypothetical event should occure, given the theoretical cross section.

Having established that a higher luminosity leads to an increased probability of discovering new physics, we turn to the downsides of high luminosity. In order to maximise luminosity, the LHC fills and squeezes the bunches so that several simultaneous proton interactions occur in most bunch crossings. This means that when a seemingly interesting event is read out, signals coming from several other interactions are also overlaid. Likewise, the short spacing between the bunches can cause signal from previous or future bunch crossing to be overlaid within the detector which has a slower readout time. When an event is recorded, the most energetic parton collision is considered to be the hard-scatter interaction, and signal coming from any other proton collision is referred to as *pile-up*. The presence of pile-up reduces the resolution with which the detector measures the outgoing particles; one can say that it causes a blurring of the picture that the detectors take of the event. The amount of pile-up is typically quantified by the average number of interactions per bunch crossing $\langle\mu\rangle$ which is shown for the years 2015 to 2018 in Figure 3.2.The figure illustrates how an increase in luminosity leads to an increase in pile-up, meaning there is a trade-off between gaining statistics and losing precision. Dedicated techniques to mitigate the effects of pile-up are discussed in Section 5.1.

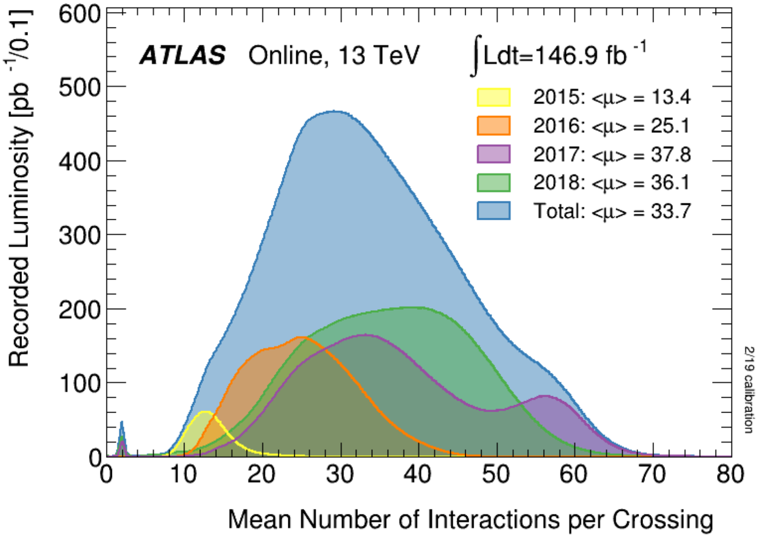

**Figure 3.2:** Luminosity-weighted distribution of the mean number of interactions per bunch crossing for collision data taken at $\sqrt{s} = 13\,\text{TeV}$ in the years 2015 to 2018 [54].

## 3.2 The ATLAS experiment

In this section we zoom in on the ATLAS experiment which is a general-purpose experiment, meaning it was designed to search for various different signatures. The wide physics scope requires a nearly hermetic geometry and good sensitivity to the known particles. With a 44 m long, 25 m wide cylindrical shape, coaxial with the beam pipe, ATLAS covers a solid angle of nearly $4\pi$ radians around the interaction point (IP). Multiple layers of subdetectors allows ATLAS to efficiently identify and reconstruct almost all particles of the Standard Model. Only neutrinos escape undetected, and their presence must be deduced by a lack of transverse momentum conservation.

The design, operation, data analysis, and continuous upgrades of this vast and complex experiment have required a huge collaborative effort spanning over three decades. Currently, the collaboration comprises about 3000 physicist from 181 different institutes representing 38 countries of all continents.

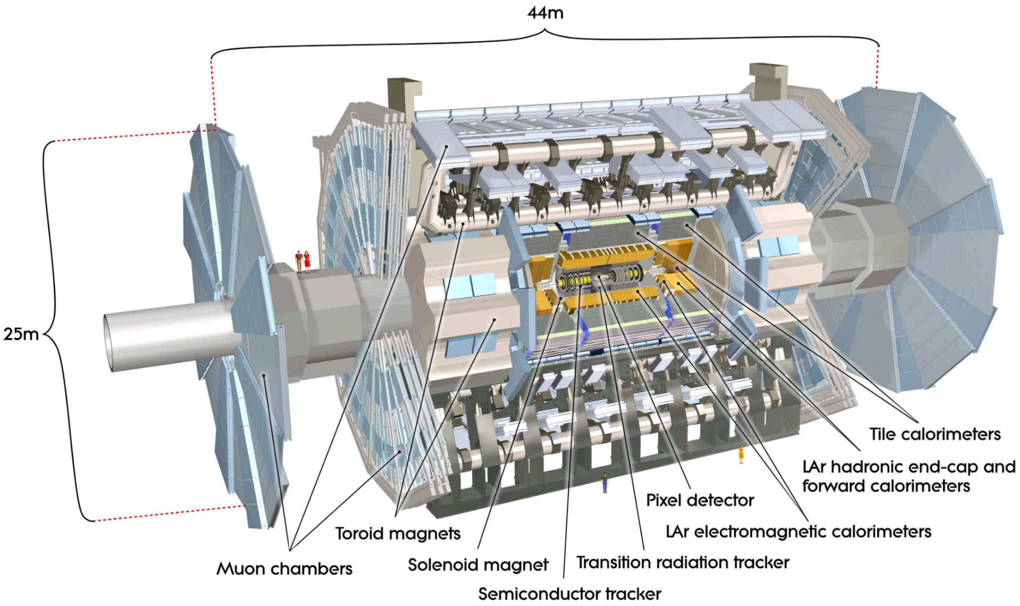

**Figure 3.3:** Illustration of the ATLAS detector layout with one side cut away, to reveal the layered structure [50].

An illustration of the ATLAS detector layout is shown in Figure 3.3. The following section presents an overview of the detector with emphasis on the components most relevant for jet reconstruction. For a more complete description, the reader is referred to [50].

### 3.2.1 Coordinate system and handy variables

The ATLAS detector uses a right-handed coordinate system with the origin located in the geometric center which is also the nominal interaction point. The $x$ axis points to the center of the LHC, the $y$-axis upwards towards the surface of the Earth, and the $z$-axis is oriented along the beam pipe. This is shown in Figure 3.4. The figure also shows the azimuthal angle $\phi$ which is measured around the $z$-axis such that $\phi = 0$ is along the $x$-axis. The polar angle $\theta$ is measured with respect to the $z$-axis having $\theta = 0$ along the beam pipe. Due to its shape, ATLAS also uses cylindrical coordinates $(r, \phi)$ in the transverse plane.

Since the initial momentum along the beam axis of the colliding partons is unknown, it

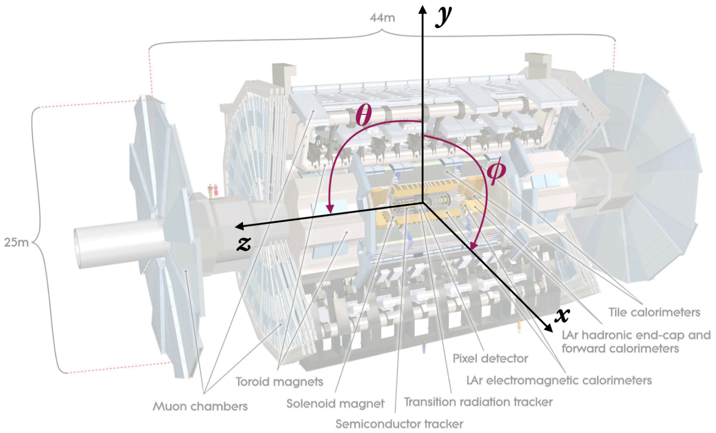

**Figure 3.4:** Coordinate system of the ATLAS detector. Inspired by [55].

is often convenient to use kinematic variables which are invariant under Lorentz boosts in the $z$-direction. The Lorentz invariant spatial coordinate, *pseudorapidity*, is defined from the polar angle as $\eta = -\ln[\tan(\theta/2)]$, such that $\eta = 0$ is aligned with the $y$-axis and $\eta = \pm\infty$ along the $z$-axis. Pseudorapidity is useful for describing locations in the detector and coverage with respect to the beam axis.

A related kinematic variable is the *rapidity* which is defined as $y = \frac{1}{2}\ln[(E+p_z)/(E-p_z)]$, where $E$ is the energy and $p_z$ is the momentum $z$-component. It is used for describing massive particles, but for massless or ultra-relativistic particles the rapidity equals the pseudorapidity.

### 3.2.2 Magnets

The ATLAS detector relies on magnetic fields to determine the momentum of charged particles by the curvature of their trajectory. The inner detector, responsible for the tracking of charged particles, is surrounded by a superconducting solenoid, providing a magnetic field of 2 Tesla. Since the solenoid and the beam are aligned, the bending radius of an outgoing charged particle can be directly translated to its transverse momentum $p_{\mathrm{T}}$. The solenoid is designed to be thin, in order to limit the amount of non-sensitive material in front of the calorimeters.

Muons typically leave a nearly straight trajectory in the inner detector before going straight

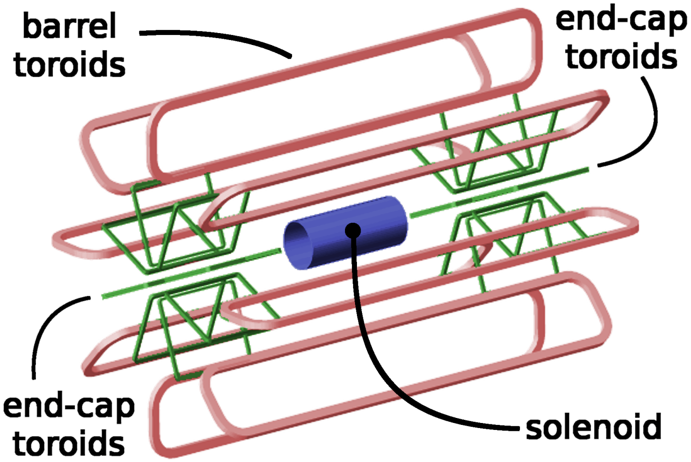

**Figure 3.5:** Sketch of the ATLAS magnet system [56] [57].

through the calorimeters. With the magnets available, it requires a much longer track, or lever-arm, to measure their momentum. Therefore, the Muon Spectrometer (MS) forms the outermost layer of the detector. The magnetic field in the MS is produced by a system of three air-core toroid magnets; one covering the central *barrel* region and one in each of the *end-cap* regions. The large toroid creates a magnetic field of 1 T in the region $|\eta < 2.4|$ and smaller end-cap magnets provide a field of 0.5 T in $1.6 < |\eta < 2.7|$. A sketch of the geometry is shown in Figure 3.5.

### 3.2.3 Inner detector

The Inner Detector of ATLAS is used for measuring the trajectory of charged particles. The tracking detectors enable ATLAS to reconstruct vertices in the event and momentum of charged particles. For particles at high $|\eta|$, only a small fraction of the momentum is perpendicular to the magnetic field of the solenoid, and the bending radius becomes to large to measure. Therefore, the inner detector extends to $|\eta| = 2.5$.

Given that particles emerge from the IP, the track density is highest in the center of the detector. Therefore, a better spatial resolution, and thus detector granularity, is required of the innermost detector layers. Due to the fact that the resolution requirements decrease and the price of instrumentation increases with radial distance from the IP (ergo, detector volume), four layers of different tracking technologies are installed. A schematic overview of the Inner Detector is shown in Figure 3.6 and a description of each subdetector follows:

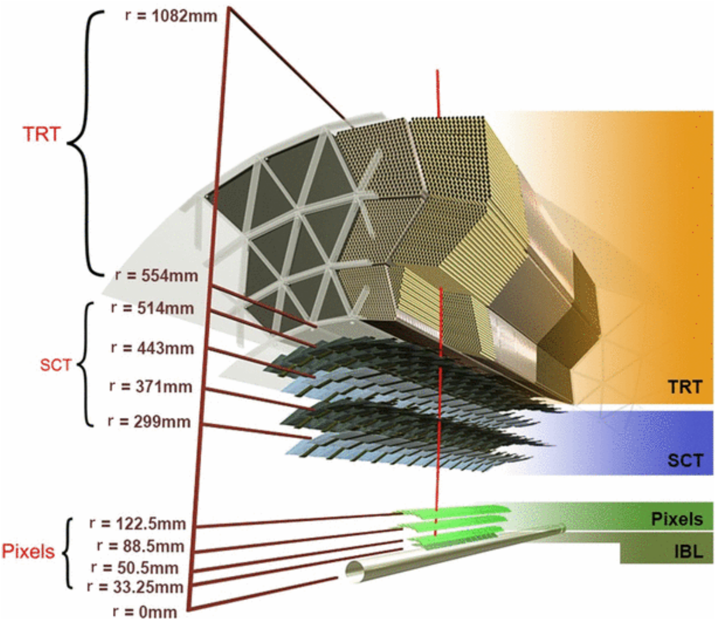

**Figure 3.6:** A schematic representation of the barrel part of the inner detector [58].

### 3.2.3.1 The Insertable B-layer

The Insertable B-layer (IBL) is the innermost component of the ATLAS detector. It comprises a single barrel shaped layer of pixel sensors with a size of $50 \times 250\,\mu\mathrm{m}^2$. The IBL was installed during the shutdown between Run 1 and Run 2 to compensate for radiation damage done to the existing Pixel detector and decrease the distance between the IP and first detector layer from 50 mm to 33 mm. This allows for a very precise vertex reconstruction, which is absolutely mandatory in the high pile-up environment ATLAS operates. Furthermore, improved vertex reconstruction allows for better identification of $b$ quarks, whose relatively long life time means that they can create a measurably displaced secondary vertex as they decay.

### 3.2.3.2 The Silicon Pixel Detector

The Silicon Pixel Detector consists of three cylindrical barrel layers and three end-cap disks at both ends. The pixel layer covers a radial distance of 50 mm to 123 mm from the IP. Each pixel contains a semiconductor sensor made from silicon, and measures $50 \times 400\,\mu\mathrm{m}^2$ in size. Combined with the IBL, the pixel detector provide the necessary high-resolution vertex and track reconstruction.

#### 3.2.3.3 The Semiconductor Tracker

The Semiconductor Tracker (SCT) surrounds the Pixel detector, extending the radius of the inner detector to about $514\,\mathrm{mm}$. The SCT is based on the same technologies as the Pixel detector, but employs larger sensors, called silicon microstrips. The strips measure $126 \times 80\,\mu\mathrm{m}^2$ each, and are arranged on four barrels and nine end-cap disks.

#### 3.2.3.4 The Transition Radiation Tracker

The Transition Radiation Tracker is the outermost part of the inner detector, covering the largest radial distance from $554\,\mathrm{mm}$ to $1082\,\mathrm{mm}$. Unlike the SCT and pixel detectors, the TRT is a gaseous ionisation detector composed of cathode tubes (or *straws*). The straw are nominally filled with xenon with an anode wire running through the center from which signal is read out. The straws are arranged parallel to the beam line along the barrel part of the detector, and radially to the beam at the end-caps. Thus the TRT provides two-dimensional hit information in $R - \phi$. Combining the hit information from the TRT with the three-dimensional information of the pixel detectors, extends the lever-arm of the track and thereby improves the spatial and momentum resolution.

The detection technology of the TRT has several advantages; gas detectors are radiation resistant, and can cover a large tracking volume at a limited cost compared to pixels. Furthermore, the TRT is able to identify electrons by making use of the *transition radiation* that is emitted when a charged particle cross from one detector material to another. Since the amount of transition radiation is proportional to the particle's relativistic gamma factor $\gamma = E/m$, it is much larger for electrons than muons and pions for a given momentum.

### 3.2.4 Calorimeters

Calorimeters measure particle energies by fully absorbing the incident particle. ATLAS uses *sampling* calorimeters where alternating layers of absorber material and active material in turn induce the particle to shower and measure the energy of the secondary particles. The ATLAS calorimeters are segmented both longitudinally and laterally to provide direction information. Two types of calorimeter technologies are employed:

- Liquid argon (LAr) calorimeters, mainly used for electromagnetic calorimetry that measure photons and electrons through their electromagnetic interactions.

- Tile calorimeters used for the hadronic calorimetry which mainly measure hadrons through their strong interactions.

An overview of the ATLAS calorimeter system it shown in Figure 3.7.

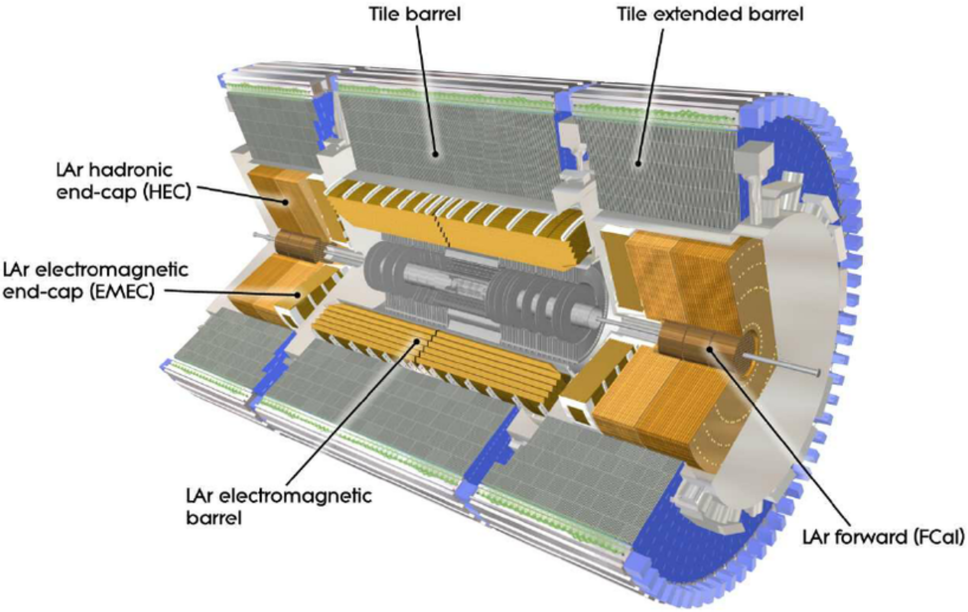

**Figure 3.7:** Cut-away view of the ATLAS calorimeter system [50].

#### 3.2.4.1 Electromagnetic calorimeter

The EM calorimeter measures energy deposited by charged particles and photons. Charged particles mainly loose energy through *bremstrahlung* as they traverse a dense medium, whereas photons deposit energy through $e^+e^-$ pair production. The electrons/positrons from pair-production emit more photons which in turn create more electrons/positrons, thus creating an electromagnetic showers.

The EM-calorimeter of ATLAS is a lead-liquid argon sampling detector, where showers primarily form in the lead absorption plates, and liquid argon works as the active medium producing ionisation electrons. It consists of a barrel part (EMB) and two end-cap parts (EMEC) surrounding the inner detector and the solenoid magnet, and provide coverage up to $|\eta| = 3.2$.

The layers of lead plates, liquid argon gaps, and electrodes are arranged into accordian shaped modules as illustrated in Figure 3.8. This geometry allows the read-out to take place in front and at the back of the calorimeter, ensuring complete coverage in $\phi$.

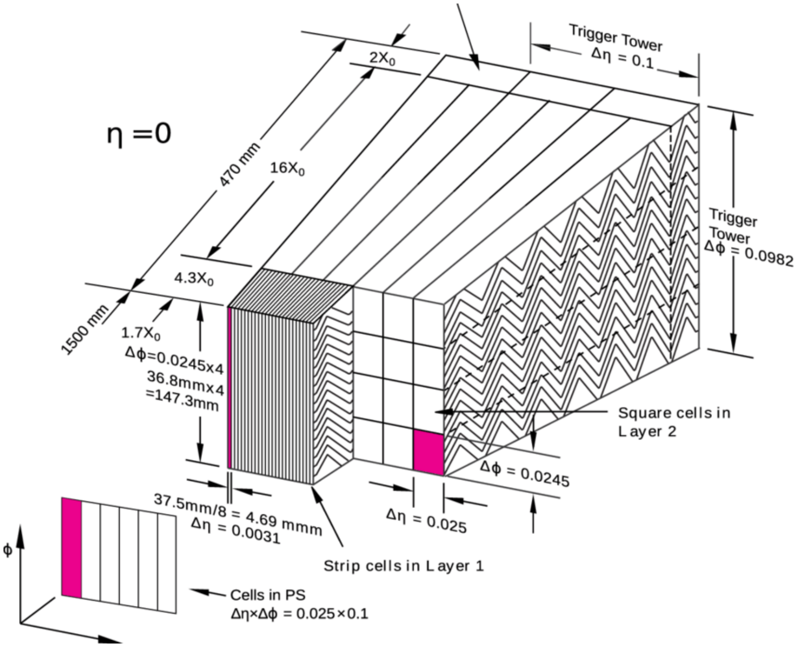

**Figure 3.8:** Sketch of a barrel module of the LAr calorimeter [50], showing how the detector granularity decreases radially. The thickness of each layer is indicated in terms of radiation lengths $X_0$.

The LAr calorimeters are divided into three layers with radially coarser granularity. The innermost layer in the barrel region ($|\eta| < 2.5$) has very fine segmentation along $\eta$, providing direction information on photons which don't produce tracks in the inner detector. In addition, the fine granularity allows for discrimination between single photons and pairs of collimated photons from the decay of a boosted, neutral meson (typically $\pi_0 \rightarrow \gamma\gamma$). The second layer is where the bulk of the energy is deposited, and a third layer is used to measure the energy leakage to the hadronic calorimeter.

Figure 3.8 indicates the thickness of each layer in *radiation lengths* $X_0$. One $X_0$ corresponds to the mean distance traveled before an electron has lost $1/e$ of its energy through bremstrahlung, or to $7/9$ of the mean free path before a high energy photon undergoes pair production. With the three layers combined, the EM calorimeter is more than $22X_0$ thick, in order to ensure minimal leakage of electromagnetic energy.

### 3.2.4.2 Hadronic calorimeter

The hadronic calorimeter is designed to contain the hadronic showers, which are caused by nuclear interactions, such as spallation, neutron capture, and nuclear recoil. The characteristic length of nuclear interaction, the *absorption length* $\lambda_h$, is defined as the length required to reduce the number of relativistic hadrons by a factor of $1/e$. For a pion traveling through lead the absorption length is $\mathcal{O}(10)$ times larger than the electromagnetic radiation length. This means, the hadronic calorimeters needs to be thicker than the EM calorimeters and the absorption material denser.

The ATLAS hadronic calorimeter is composed of two technologies: A Tile calorimeter covering $|\eta| < 1.7$ with a barrel and an extended barrel part, and LAr calorimeter covering the forward region $|\eta| > 1.7$. The Tile calorimeter uses steel as absorbers and scintillating tiles as the active material. The scintillators are read out via photomultiplier tubes, as shown in Figure 3.9. The average thickness of the tile calorimeter is $7.4\lambda_h$.

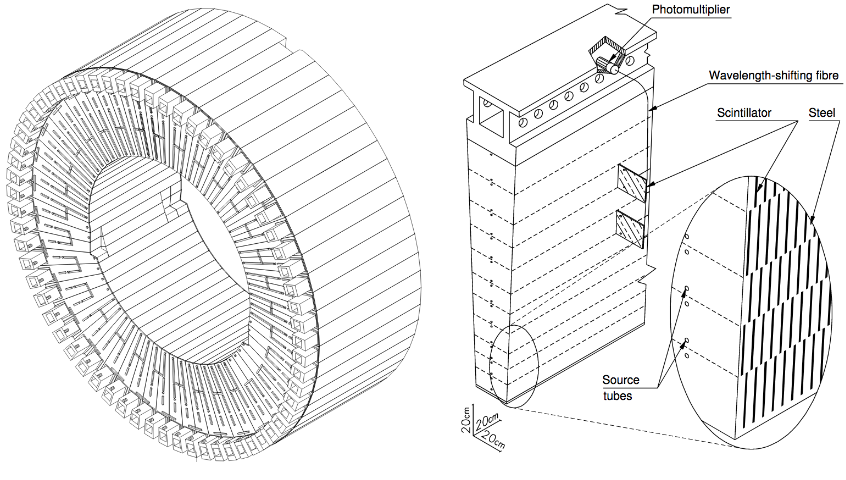

**Figure 3.9:** Illustration of the Tile calorimeter, showing an overview of the layout on the left, and a zooming in on a single tile on the right [50].

The end-caps of the hadronic calorimeter (HEC) use copper plates as absorbers and liquid argon as the active material, due to the radiation hardness of this technology. The HEC extends the coverage of the hadronic calorimeter up to $|\eta| = 3.2$ and has a thickness of roughly $12\lambda_h$.

#### 3.2.4.3 Forward calorimeter

A forward calorimeter (FCal) is placed in the center of both hadronic endcaps, to provide hadronic and EM calorimetry in the range $3.1 < |\eta| < 4.9$. The FCal uses liquid argon as active material. An inner layer is mase for electromagnetic calorimetry using copper plates as the absorbing material, and an outer layer performs the hadronic calorimetry with tungsten plates as absorbers.

### 3.2.5 Muon spectrometer

Muons and neutrinos are the only Standard Model particles, that are expected to (regularly) travel all the way through the calorimeters. Therefore, the Muon Spectrometer (MS) is located outside the calorimeters as the outermost layer of the detector. Similarly to the inner detector, the MS measures the momentum of charged particles based on the deflection of their tracks in a magnetic field. As described in Section 3.2.2, the large toroid magnets of ATLAS are responsible for creating the magnetic bending field.

The MS is composed of gaseous chamber arranged in three layers that are cylindrical in the barrel region and perpendicular disks at the end-caps. Several gas chamber technologies are used depending on their purpose. The position of each component is pointed out in Figure 3.10.

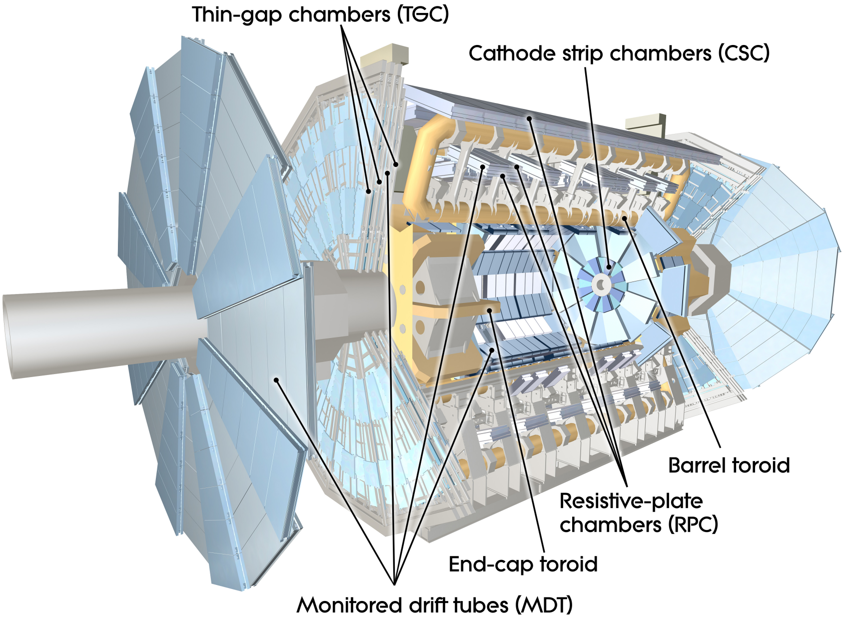

**Figure 3.10:** A cut-away view of the ATLAS Muon Spectrometer (MS) with the location of the different detector technologies indicated [50].

In the region $|\eta| < 2.0$, track measurements are done by Monitored Drift Tubes (MDT). An MDT is a straw tube in which gas is ionised by the passing muon, and the ionisation electrons are collected by an anode wire at the center of the straw.

For $2.0 < |\eta| < 2.7$ there are also two layers of MDTs, but the innermost layer is made of Cathode Strip Chambers (CSC), allowing for a finer detector granularity. The CSC are multi-wire proportional chambers, with the cathode segmented into strips, and the direction of the strip is perpendicular to one of the wires.

The muon trigger system relies on the Resistive Plate Chambers (RPC) and the Thin Gap Chambers (TGC). The RPCs covers up to $|\eta| = 1.05$, where each RPC has two parallel metal plates which are separated by a thin layer of gas that the crossing muon ionises. The ionisation electrons drift towards one of the metal plates from which the signal is read out. The region beyond $|\eta| > 1.05$ is covered by TGCs, which have a layer of anode wires between the two parallel plates.

### 3.2.6 LUCID

LUCID (LUminosity Cherenkov Integrating Detector) is a dedicated luminosity measurement detector, placed very close to the beam pipe, 17 m from the interaction point on both sides [59]. It detects Cherenkov light of charged particles coming from the collision debris, thereby providing online monitoring of the instantaneous luminosity.

### 3.2.7 Trigger system

When the LHC is running, bunch crossings occur every 25 ns, corresponding to an event rate of 40 MHz. It is not technically feasible to process and store the resulting amount of data, so a trigger system is used to identify potentially interesting events, and prompt the data acquisition system to read out all signals in the detector. The trigger system operates with two levels:

- The first level, called the Level-1 (L1) trigger, is designed to be simple but fast. It is, therefore, implemented on custom hardware. The purpose of the first level is to select high momentum physics objects, such as electrons, photons, muons, and jets. L1 trigger decisions are based on signals from the calorimeters and the muon trigger chambers. The two systems are often referred to separately as the L1Calo and the L1Muon.

  The L1 trigger reduces the event rate from 40 MHz to 100 kHz. The amount of information in each event, passed on to the next trigger level, is also reduced. That is done by defining regions of interest (RoI), which are areas in $(\eta - \phi)$-space where large energy deposits or high-momentum muon tracks occurred.

- The second level is called the High Level Trigger and is implemented in software. At this level various physics objects (electrons, muons, photons, jets, and $E_T^{\text{miss}}$) are reconstructed from the RoIs. The HLT trigger decisions are then based on the reconstructed kinematics, reducing the event rate to about 1 kHz. A summary of the HLT trigger rates is shown in Figure 3.11.

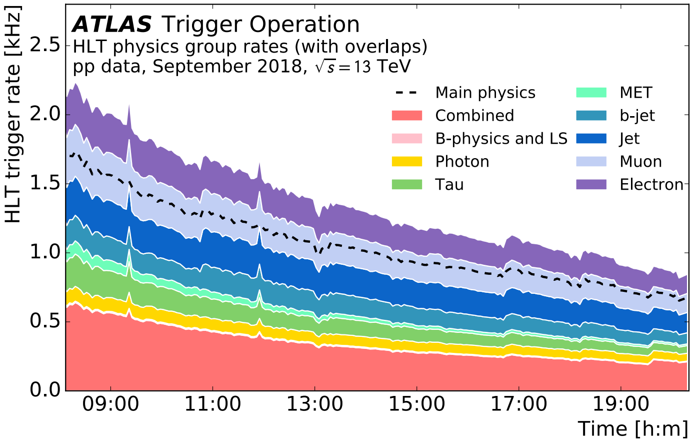

**Figure 3.11:** Trigger rates at the HLT for each of the ATLAS physics groups. The rates decrease exponentially as function of time, because of the decreasing luminosity during an LHC fill.

During Run-2, ATLAS recorded data based on approximately 1500 combinations of L1 and HLT trigger criteria, also known as the *trigger menu*. The rate of the different triggers vary enormously, depending especially on the $p_{\mathrm{T}}$ threshold. In order to control the event acceptance rate, the triggers that fire most frequently are *prescaled*. That means, that an event passing one of these triggers has a probability of $1/n_p$ to be kept, where $n_p$ is the prescale factor. Since we generally expect the known physics phenomena to occurs more frequently, it makes sense to save bandwidth for the more rarely occurring triggers. However, the loss of statistical precision caused by the prescaling, lead to a lower sensitivity to especially low-$p_{\mathrm{T}}$ and low-mass BSM phenomena.

#### 3.2.7.1 Phase-1 upgrade of the L1Calo

During the current shut down of LHC (2019 to 2020), several detector components are being replaced to cope with the high pile-up levels expected in Run-3 due to the increase in instantaneous luminosity. These efforts are commonly know as the Phase-1 upgrades.

In Run-2 the inputs to the L1Calo system were *Trigger Towers* formed by analog summation of calorimeter cells across longitudinal layers in a region of $\Delta\eta\phi = 0.1 \times 0.1$. The Phase-1 upgrade will provide digital optical signals to the L1Calo system, allowing for three types of trigger towers of different granularities to be sent to the L1Calo.

Higher granularity information from the LAr will improve the identification of electrons, photons, and taus, while the availability of coarser granularity information will enable processing of the full calorimeter on a single module [60] [61]. To process the digital signals, three new sub-systems will be added to the L1Calo: The electromagnetic feature extractor (eFEX), the jet feature extractor (jFEX), and the global feature extractor (gFEX).

### *eFEX*

The Phase-1 upgrade increases the granularity of the LAr signals to ten *SuperCells* per trigger tower. SuperCells are formed as the sum of four or eight calorimeter cells from only one layer in the LAr calorimeter, thereby providing also depth segmentation. The eFEX processors are designed to look for electron, photon, and tau signatures using SuperCells from the LAr and trigger towers from the Tile calorimeter. A total of 24 eFEX boards is required to process all data from the calorimeter region of $|\eta| < 2.5$.

### *jFEX*

The jFEX processors are designed to trigger on jets, missing transverse momentum $E_T^{miss}$, and total transverse momentum $E_T$. The granularity of SuperCells is not required to reconstruct jets. Therefore, jFEX will receive *jTowers* which are similar to the Trigger Towers of Run-2 with a granularity of $0.1 \times 0.1$. Each jFEX module reads out the full calorimeter $\eta$ range ($|\eta| < 4.9$) of one $\phi$-octant, meaning eight jFEX modules are required to cover the whole solid angle of the calorimeter.

### *gFEX*

The gFEX will receive *gTowers* which are similar to jTowers, but have an even coarser granularity of $0.2 \times 0.2$, and no layer information. The coarser data format allows the gFEX to read out the full $\eta$ and $\phi$ range on a single board. This enables the gFEX to trigger on globally computed $E_T^{miss}$ and perform event-wide pile-up subtraction. Furthermore, the gFEX will be able to trigger on large-radius jets which will improve the sensitivity of ATLAS to hadronically decaying $W$ bosons, top quarks, Higgs bosons, and new heavy resonances.

# Part II

# Jet Physics in ATLAS

When Murray Gell-Mann originally proposed that hadrons and mesons consisted of fractionally charged subcomponents, it might have been with a certain degree of irony that he adopted the spelling 'quark' from the James Joyce' *Finnegan's Wake*;

*Three quarks for Muster Mark!*
*Sure he hasn't got much of a bark*
*And sure any he has it's all beside the mark.*
*But O, Wreneagle Almighty, wouldn't un be a sky of a lark*
*To see that old buzzard whooping about for uns shirt in the dark*
*And he hunting round for uns speckled trousers around by Palmerstown Park?*

as he perhaps imagined all physicist would now start hunting around in the dark for these peculiar entities which could never be observed in isolation.

However, as quantum chromodynamics developed, it became clear that although quarks were not to be observed in isolation, they might still leave a distinct and detectable signature - a collimated spray, or "jet", of hadrons in the direction of the original quark. But Gell-Mann was right for about 15 years. I was not until 1975, when high enough centre-of-mass energies became available at at SLAC's $e^+e^-$ storage ring SPEAR, that hadron jets were discovered. Even then did he probably not imagine that in a few decades jets would be central to testing QCD and even prove to be powerful tools to search for new heavy particles beyond the Standard Model.

In this part I will discuss how jets are measured experimentally with the ATLAS detector. The first two chapters review the definition and calibration of jets. I mainly focus on the two most common types of jets in ATLAS, which are also used in the two analyses presented later on. Lastly I'll account for the numerous techniques used to distinguish different types of jets based on their substructure.

# Chapter 4

# Jet Reconstruction

The first experimental evidence of quark jets came from the $e^+e^-$ collider SPEAR at SLAC in 1975. With a maximum beam energy of 4 GeV, the presence of jets had to be inferred by studying global event variables such as sphericity and thrust in order to demonstrate that the hadrons in the final state were not isotropically distributed [62]. At the LHC, quarks are typically produced with such large energies that the hadron shower is collimated enough for jets to be seen in event displays with our bare eyes. However, criterion-based definitions are required to process the very large number of events, both for the obvious sake of time and to avoid arbitrariness where the presence or number of jets is unclear.

There exists many ways of defining and reconstructing jets, and their usefulness depends on both the detector design (geometry, calorimeters, trackers) and the physics of interest. Generally, all reconstruction algorithms require a method to identify interesting regions or objects in the event and a method to actually build jets from the objects selected by the first method. In this section I will cover some of the most common jet definitions with emphasis on the techniques commonly used in ATLAS.

## 4.1 Inputs to jet algorithms

In the busy environment of proton-proton collisions, there is lots of activity in the calorimeters not coming from the hard-scattering interaction. Signals coming from pile-up (PU) and the underlying event (UE) blurs the picture of the interaction that we are actually interested in. Therefore it is beneficial, both in terms of resolution and computing time, to condense the event to a selection of interesting regions or objects, to pass as inputs to the jet algorithm. Several jet inputs are used in ATLAS for different purposes. Some are based solely on calorimeter signals and others combine those with track information. Here

I briefly explain the two most common input definitions:

### 4.1.1 Topological clusters

Due to the fine segmentation and layering of the ATLAS calorimeters, the jet definitions have traditionally relied on calorimeter information alone. Topologically connected calorimeter cells with a signal above a certain threshold make out the objects passed to the jet finding algorithm. By constructing so-called *topoclusters* [63], detector regions of high energy density are localised and fluctuations due to e.g. noise or pile-up are suppressed. Topoclusters are seeded by cells with an energy deposit significantly above the average noise fluctuations $\sigma_{\text{noise}}$. The cluster grows in three dimensions by adding neighboring cells with an energy deposit satisfying a softer significance criterion. The default scheme has three steps:

1) Cells with $E > 4\sigma_{\text{noise}}$ are selected as seed cells.
2) All neighboring cells with $E > 2\sigma_{\text{noise}}$ are added to the corresponding cluster.
3) All neighboring cells with $E > 0$ are added to the corresponding cluster.

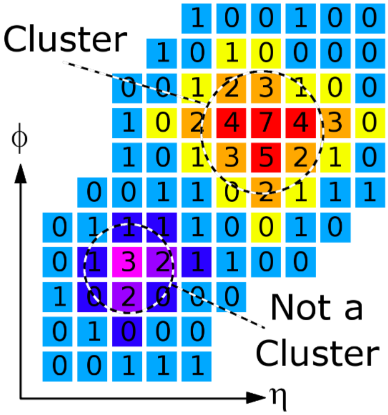

**Figure 4.1:** Sketch of the topoclustering. Red means the cell is a seed, orange means the cell was added in the second step, and yellow means third. The blue and purple cell are not clustered.

The clusters are calibrated to better reflect the true energy of the particle that created them. Initially they are brought to the *electromagnetic* (EM) scale, where the cluster energies are defined by the the baseline calorimeter scale that correctly measures energy depositions from electromagnetic showers. However, the calorimeter response is lower for hadronic interactions, by amounts depending on the location of the shower. Therefore they can be further calibrated with the *local-cell weighting* (LCW) method, which is derived from MC simulations of single pions (charged and neutral). With LCW, clusters are classified as either electromagnetic or hadronic, and a corresponding energy correction is applied. Further corrections are applied to compensate for the varying response across the calorimeters, due to energy deposits in dead material and noise threshold effects, eventually improving the energy resolution of the reconstructed jet.

At last an *origin correction* is applied to accounts for the finite size of the LHC beam spot, by modifying the topocluster's four-momentum to point back to the primary vertex of the hard scattering rather than the center of the detector. Without changing the energy of the cluster, this improves the $\eta$-resolution of the final jet.

### 4.1.2 Particle Flow

Particle flow (PFlow) objects combine information from the inner detector and the calorimeters [64]. By selecting high quality tracks from charged particles and topoclusters not associated to a selected track, PFlow objects exploit the best of both parts of the detector. For low $p_{\mathrm{T}}$ particles the tracker gives better angular and $p_{\mathrm{T}}$ resolution in addition to the ability to trace back individual particles to their vertex. For high $p_{\mathrm{T}}$ particles the calorimeters give the best energy resolution and it also captures neutral particles. The algorithm first selects high quality tracks coming from the primary vertex with $p_{\mathrm{T}} < 40$ GeV, and tries to match them to clusters based on the distance metric

$$\Delta R' = \sqrt{\left(\frac{\eta}{\sigma_\eta}\right)^2 + \left(\frac{\phi}{\sigma_\phi}\right)^2} \tag{4.1}$$

where $\sigma_\eta$ and $\sigma_\phi$ represent the width of the topocluster defined as one standard deviation of the cluster cell angular distances from the cluster's barycenter. The track is matched to the cluster with smallest $\Delta R'$ unless no cluster is found with $\Delta R' < 1.64$, in which case it is a assumed that the particle that produced the track did not produce a topocluster. For each track/topocluster system, the probability that the particle energy was deposited in more than one cluster is evaluated and the additional cluster can be added accordingly.

For every cluster matched to a track, the energy corresponding to the track $p_{\mathrm{T}}$ is subtracted from the cluster depending on the its position and the track $p_{\mathrm{T}}$. All selected tracks and remaining topocluster then constitute the PFlow objects passed to the jet algorithm. This definition of the input objects has been found to improve both angular and $p_{\mathrm{T}}$ resolution of jets which is key to measuring missing transverse energy. Furthermore, it reduces the pile-up contribution in jets.

More jet inputs that combine track information with calorimeter cluster are being studied, such as Track Calo Clusters (TCC) [65] and Unified Flow Objects (UFO) that merges PFlow and TCC inputs.

## 4.2 Jet finding

Once a set of inputs is defined, the next step is to determine which ones should be clustered together in jets and how. An intuitive strategy could be to define a cone of fixed size and sum up all momenta inside it. However, such an algorithm is not insensitive to arbitrarily soft and collinear splittings - it is not what is called *infrared and collinear safe*. A good jet finding algorithm must be reproducible by calculation, in order to have theoretical predictions that can be compared to data. If additional infinitely soft emissions or small-angle splittings can change the conclusion, the result is not reliable. Algorithms in the category of sequential recombination algorithms are both infrared and collinear safe, and have thus become the preferred choice for jet finding. Sequential jet finding algorithms can be expressed in a generalised form by introducing the distance $d_{ij}$ between two clusters $i$ and $j$, as well as the distance $d_{iB}$ between cluster $i$ and the beam axis $B$ [66]:

$$d_{ij} = \min(p_{Ti}^{2p}, p_{Tj}^{2p})\frac{\Delta R_{ij}^2}{R^2}, \quad d_{iB} = p_{\mathrm{T}i}^{2p} \tag{4.2}$$

where $\Delta R_{ij} = (y_i - y_j)^2 + (\phi_i - \phi_j)^2$, and $p_{\mathrm{T}i}, y_i$ and $\phi_i$ are respectively the transverse momentum, rapidity and azimuthal angle of cluster $i$. Jets are then constructed by following the recipe:

1) The distances $d_{ij}$ and $d_{iB}$ are computed for all possible pairs and the minimum of is identified.
2) If the smallest of the distances is a $d_{ij}$, the two objects $i$ and $j$ are combined.
3) Else, the object $i$ is declared a jet and removed from the cluster collection.
4) The distances are recalculated and the procedure repeated until no more clusters remain.

The radius parameter $R$ determines the maximal distance two objects can be apart in order to be considered for combination. The standard jet size used in ATLAS is $R = 0.4$, whereas $R = 1.0$ is typically used to target jets from hadronic decays of heavy, boosted particles, such as $W, Z$ and top quarks. A rule of thumb for massive particles is that the jet size roughly obeys $R \sim 2m/p_{\mathrm{T}}$, which means that a $W$ boson with $p_T > 160$ GeV should be contained in a jet cone of $R = 1.0$

The parameter $p$ governs the relative importance of energy versus geometrical distance and can be positive, negative, or zero, depending on the jet finding algorithm. The absolute value of $p$ matters little as it is the sign that governs the order of combination. The three most widely used options are $p = 1, 0, -1$:

#### 4.2.0.1 $p = 1$: The $k_t$ algorithm

With $p > 0$ the softest constituents are clustered first. This means that the jet axis moves around as higher $p_{\mathrm{T}}$ objects are added. As the algorithm is adaptive to soft particles, the shape of the jet can be rather random.[1]

#### 4.2.0.2 $p = 0$: Cambridge/Aachen algorithm

With $p = 0$ the algorithm is independent of all $p_{\mathrm{T}}$ measures and only determined by the angular separation between objects. Small-angle pairs are combined first, and the jet axis moves around as high-$p_{\mathrm{T}}$ objects are added.

#### 4.2.0.3 $p = -1$: The anti-$k_t$ algorithm

The version most often used in ATLAS, is the “anti-$k_t$” algorithm [66] with $p = -1$, which clusters the hardest constituents first. Thus the jet axis is mostly fixed from the beginning, and the radius parameter $R$ determines the angular width of the jet. This means that hard jets become circular and only softer jets can have more complex shapes.

The different behavior of the three algorithms can seen in Figure 4.2, where the truth-level particles (see Section 4.3) of a simulated event is clustered using each of the algorithms. Random soft particles have been added uniformly to the event, and the colors illustrate the region in which these random particles are clustered.

## 4.3 Alternative jet definitions

We have now seen that the outcome of the jet reconstruction depends on how we cluster the event with jet finding algorithms, but also how we determine the inputs to those algorithms. Defining what constitutes a jet is clearly nontrivial, but in order to make meaningful com-

---

[1] The name, $k_t$, comes from the original formulation of sequential algorithms, where the transverse momentum was notated by $k_t$

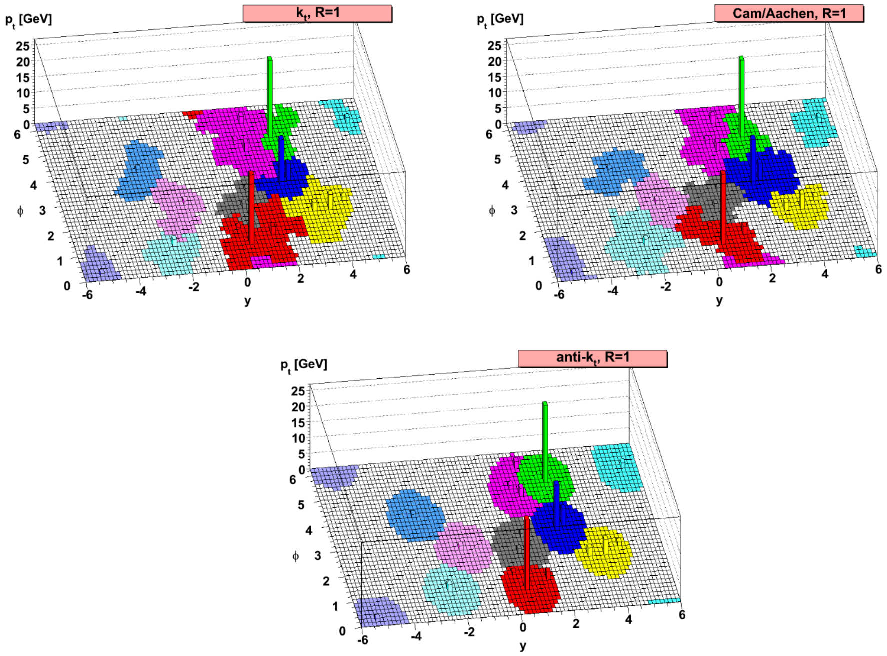

**Figure 4.2:** Example of a truth-level event clustered with three different jet finding algorithms. The colours illustrate the area within which infinitesimally soft particles are clustered [66].

parisons between experimental data and theoretical predictions, we need a definition to provide some kind of "true" reference scale of the jet properties.

In principle the jet can be defined at any stage of the jet formation, as indicated in Figure 4.3: The original parton is accelerated by the hard-scattering interaction, it radiates gluons to produce what we call a *parton jet*, and the partons then hadronise to form a *particle jet*. The measured signals in the calorimeter (and potentially the tracker) make out the *reconstructed jet*.

So far we have been occupied with the reconstructed jet, but ideally, we would be interested in the properties of the original parton or the parton jet. Those concepts are, however, ambiguous, due to partons divergent branching probabilities. Instead, we typically use the particle level jet as a definition of the "true" reference scale. Like for the reconstructed jet, there is no universally correct definition of the particle-level jet, but several ways it can be reconstructed:

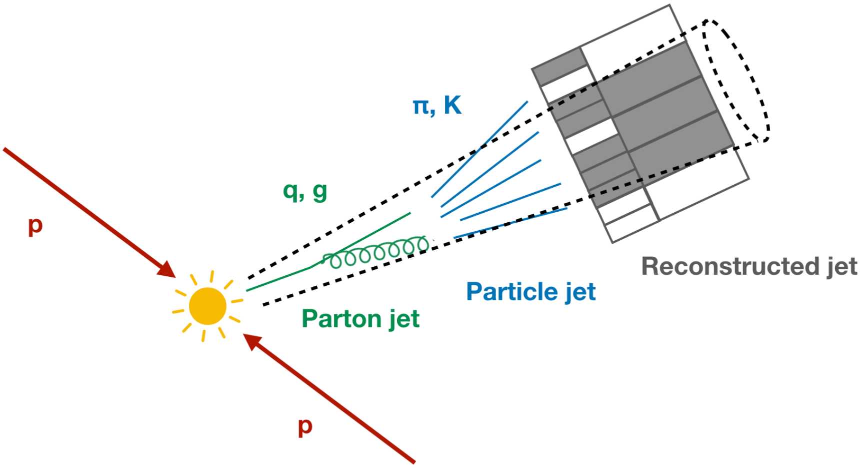

**Figure 4.3:** Sketch of the various definition of a jet.

### 4.3.1 Truth jets

With simulated events, we can define a good approximation to the particle-level jet, called the *truth jet*. Truth jets are reconstructed by clustering stable particles originating from the hard-scatter interaction, requiring them to have a life time of $c\tau > 10\,\mathrm{mm}$. Muons and neutrinos, which do not deposit a significant amount of energy in the calorimeters are excluded, as well as particles from pile-up. Truth jets are clustered with the same algorithm as the reconstructed jets they are compared to and selected with the same $p_{\mathrm{T}}$ and $\eta$ thresholds. Reconstructed jets are then geometrically matched to truth jets based on the angular distance $\Delta R$, to determine the right reference objects for simulation-based calibrations.

### 4.3.2 Track jets

We can approximate the electrically charged part of the particle-level jet both experimentally and in data using *track jets*, which are reconstructed from charged-particle tracks. Track jets can be used as reference objects in calibration and uncertainty studies, taking advantage of the independence of instrumental systematic effects between the inner detector and the calorimeter. They can also be useful for the jet mass reconstruction, as we will see in Section 4.4. Track jets are reconstructed by applying the same jet reconstruction procedure to tracks as those used when constructing the topocluster jets described above, including the jet trimming algorithm, described in Section 5.1. Track jets are not calibrated.

## 4.4 Jet mass definitions

The mass of a particle is one of its most distinctive characteristics. Since large-radius jets are often used to describe hadronically decaying, massive particles, it is crucial to reconstruct their mass in order to distinguish heavy objects from jets induced by light quarks or gluons.

The mass reconstruction, described in [67], depends on both the energy and angle between the decay products, and therefore requires a detector granularity finer than the size of the jet. The angular spread in the decay products of a boosted massive particle scales as $1/p_{\mathrm{T}}$, so the jet size becomes comparable to the calorimeter granularity for a sufficiently large Lorentz boost. The tracker, has finer angular granularity, so tracking information can be used to maintain performance for jets with $p_{\mathrm{T}}$ beyond the calorimeter granularity limit. However, the calorimeters generally have a better jet energy resolution at lower $p_{\mathrm{T}}$, since they measure the energy from both the electromagnetic and hadronic components of the jet. Therefore, two mass definitions exist, which can be combined to obtain the best resolution over the full range of $p_{\mathrm{T}}$.

*Calorimeter mass:*
The calorimeter-based jet mass $m^{\mathrm{calo}}$ is defined as

$$m^{\mathrm{calo}} = \sqrt{\left(\sum_i E_i\right)^2 - \left(\sum_i \vec{p}_i\right)^2}, \tag{4.3}$$

where the index $i$ runs over all calorimeter cells constituting the jet, $E_i$ is the energy, and $\vec{p}_i$ the momentum of the constituent $i$.

*Track-assisted mass:*
The mass of a track jet only accounts for the jet's charged constituents, but by scaling it with the ratio of transverse momenta of the calorimeter and track jet, the mass of the full jet can be obtained:

$$m^{\mathrm{TA}} = \frac{p_{\mathrm{T}}^{\mathrm{calo}}}{p_{\mathrm{T}}^{\mathrm{track}}} \times m^{\mathrm{track}} \tag{4.4}$$

where $m^{\mathrm{TA}}$ is the track-assisted mass, $p_{\mathrm{T}}^{\mathrm{calo}}$ and $p_{\mathrm{T}}^{\mathrm{track}}$ is, respectively, the calorimeter and track jet transverse momentum. The track jet mass $m^{\mathrm{track}}$ is defined like the calorimeter-based mass, but where the index $i$ runs over the constituent tracks.

*Combined mass:*
As the calorimeter-based jet mass is not used explicitly in the construction of the track-assisted jet mass, the response resolution can be reduced by combining information from both definitions. Fluctuations in the calorimeter energy response impact both the calorimeter-based jet mass and $p_{\mathrm{T}}$ response. However, the $p_{\mathrm{T}}$ response is not as sensitive to the local distribution of fluctuations and therefore the jet $p_{\mathrm{T}}$ response and the calorimeter-based jet mass response are nearly independent. The approximate independence and Gaussian nature of the $p_{\mathrm{T}}$ and mass responses means that the optimal combination of the two variables is linear:

$$m^{\mathrm{comb}} = w^{\mathrm{calo}} \times m^{\mathrm{calo}} + w^{\mathrm{track}} \times m^{\mathrm{track}} \tag{4.5}$$

When $m^{\mathrm{calo}}$ and $m^{\mathrm{track}}$ are calibrated, the combined mass is also automatically calibrated if $w^{\mathrm{calo}} + w^{\mathrm{track}} = 1$. With this constraint, the minimal resolution of the combined mass is obtained with the weights:

$$w^{\mathrm{calo}} = \frac{\sigma_{\mathrm{calo}}^{-2}}{\sigma_{\mathrm{calo}}^{-2} + \sigma_{\mathrm{TA}}^{-2}}, \quad w^{\mathrm{TA}} = \frac{\sigma_{\mathrm{TA}}^{-2}}{\sigma_{\mathrm{calo}}^{-2} + \sigma_{\mathrm{TA}}^{-2}} \tag{4.6}$$

Where the resolutions of the calorimeter-based and track-assisted mass measurements, $\sigma^{\mathrm{calo}}$ and $\sigma^{\mathrm{track}}$, are defined as the central 68% inter-quantile range of the jet mass response distribution in dijet events.

Figure 4.4 shows the fractional mass resolution of the two definitions separately and combined as a function of the associated truth jet $p_{\mathrm{T}}$. The shown resolutions are computed for jets from boosted *W* and *Z* bosons decaying hadronically. It can be seen that the calorimeter mass has a lower resolution at low values of jet $p_{\mathrm{T}}$, whereas the track-assisted mass performs better beyond $p_{\mathrm{T}} > 1000$ GeV. By construction, the resolution of the combined mass measurement is always better than either of the two inputs.

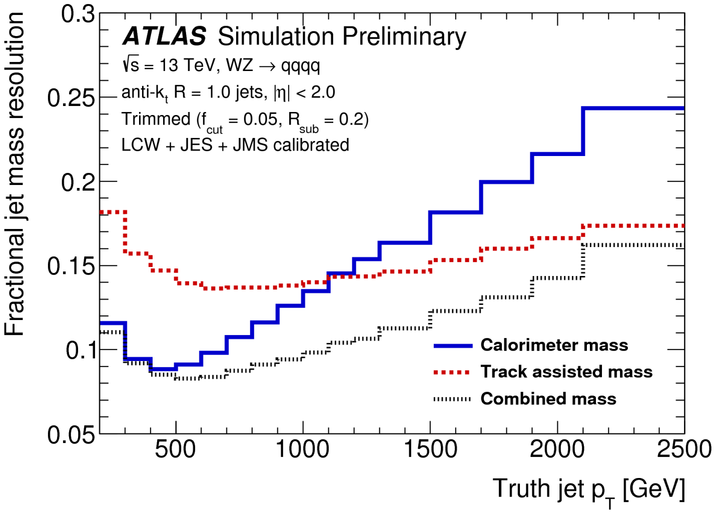

**Figure 4.4:** The jet mass resolution as function of truth jet $p_{\mathrm{T}}$ for the calorimeter-based mass definition shown as a dashed red line, the track-based definition as solid blue line, and the combined mass as a dotted black line. The shown resolutions are computed for jets from boosted $W$ and $Z$ bosons, generated via $W/Z \rightarrow qqqq$ processes in Pythia 8 [67].

# Chapter 5

# Jet Calibration

The calibration aims to translate the experimantal signature of a reconstructed jet to more useful observables, such as the particle-level truth jet energy and mass. Part of the work was already done at the stage of topoclusters, where each cluster was calibrated individually to better reflect the energy of an individual particle constituent. Many effects, some of which have already been mentioned, must still be corrected for, in order to obtain a good translation for the full jet:

- Inactive material: Energy deposited in non-sensitive material in the detector.
- Calorimeter non-compensation: Partial measurement of energy deposited by hadrons.
- Punch-through: Showers extending beyond the calorimeters.
- Pile-up: Additional energy deposits from particles not originating from the jet.
- Out-of-cone radiation: Part of the shower not included in the jet cone.
- Noise threshold effects: Energy deposits below the noise threshold.

Because of the variety of effects in play, the calibration is derived in a chain of steps that each address one or more of these effects. Every step of the calibration can vary for different jet definitions, but the principles are the same. First, pile-up contributions are mitigated, then one or two simulation-based calibrations are applied, and lastly a data-driven *in situ* calibration is derived. A schematic overview of the calibration procedure in Figure 5.1.

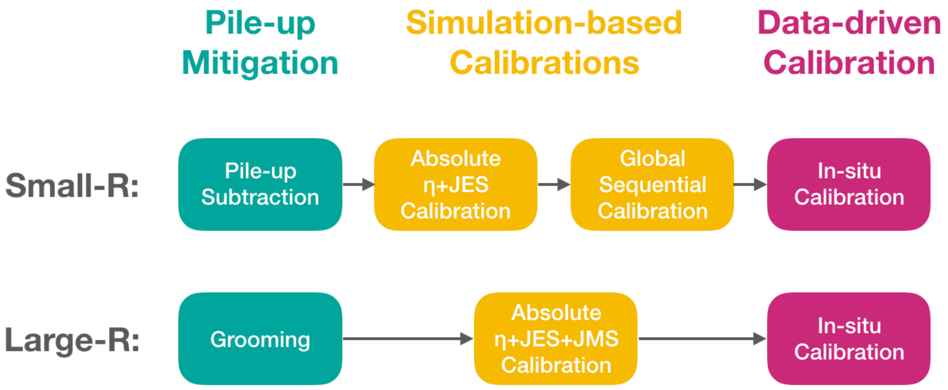

**Figure 5.1:** General overview of the jet calibration scheme. Similar steps are applied to small- and large-$R$ jets expect for the Global Sequential Calibration, which is only derived for small-$R$ jets.

In this chapter I focus on the calibration of the two most common jet types, which I will refer to as:

- **Small-$R$ jets**: Anti-kt, $R = 0.4$, build from PFlow objects or EM topoclusters.
- **Large-$R$ jets**: Anti-kt, $R = 1.0$, build from LCW topoclusters.

These two jet definitions will also occur in the analyses, presented later in the dissertation. Each step of the calibration will be explained, and potential differences between the treatment of small- and large-$R$ jets highlighted when relevant. The calibrations apply to data from the LHC Run 2. The *in situ* calibrations are derived from data collected between 2015 and 2017. Some of the *in situ* results shown for large-$R$ jets, are made with data from 2015 and 2016, as these plots have not been made public for the full dataset. A full account of the small- and large-$R$ jet calibration schemes can be found in [68] and [69], respectively.

## 5.1 Pile-up mitigation

As mentioned previously, pile-up is the common term for detector signals that arise from other interactions than the hard-scatter interaction of interest. It is the currency we pay in, when increasing the collider luminosity to get more statistics (in addition to electricity, person power and probably many other costs). It is often useful to distinguish between two types of pile-up in the calorimeters:

- In-time pile-up: Energy deposits in the jet from other interaction vertices in the same bunch crossing. This is related to the number of primary vertices ($N_{\mathrm{PV}}$) in the event.
- Out-of-time pile-up: Energy deposits from particles stemming from previous or future bunch crossings. This is caused by the fact that the calorimeter readout is longer than the time difference between two bunch crossings, and is related to the average number of interactions per bunch crossing $\langle\mu\rangle$.

### 5.1.1 Pile-up subtraction (small-*R* jets)

***Area-based subtraction***

For small-$R$ jets, pile-up is mitigated by subtracting three terms directly from the jet $p_{\mathrm{T}}$ [70]. The first term is proportional to the area of the jet, since that is a measure of how susceptible the jet is to pile-up. The active area of the jet $A$ is calculated by a technique call *ghost association* [71]. Simulated particles of infinitesimal momentum ("ghost" particles) are added uniformly to the event. The area is then proportional to the number of ghost particles associated with the jet after clustering. Once the event is clustered into a collection of jets, the $p_{\mathrm{T}}$ density $p_T/A$ is computed for each one. The median $p_{\mathrm{T}}$ density $\rho$ is then used to calculate the pile-up contribution, rather than the mean, in order to reduce the bias from the hard-scatter jets. For calculating $\rho$, the event is clustered using the $k_t$-algorithm as that is more sensitive to soft radiation. The clustering considers positive-energy topoclusters in the central part of the detector, where the detector granularity is high and the relation between pile-up conditions and $\rho$ is more pronounced. The relation is illustrated in Figure 5.2 where the $\rho$ distribution is shown for three different pile-up conditions.

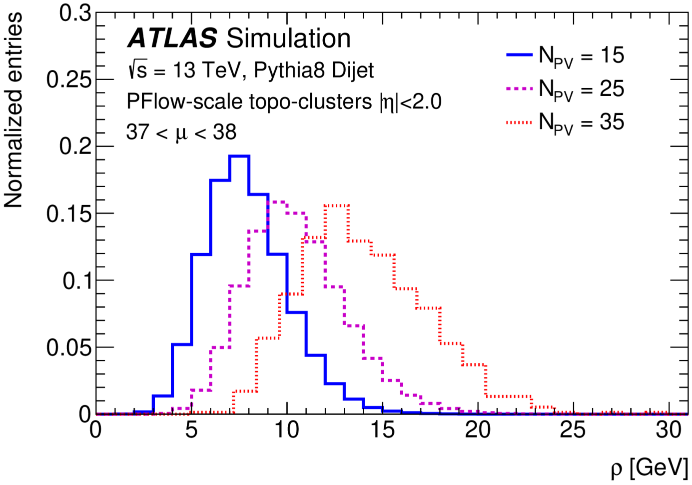

**Figure 5.2:** Distribution of median $p_{\mathrm{T}}$ density $\rho$ for events with either $N_{\mathrm{PV}} = 15$ (solid blue line), $N_{\mathrm{PV}} = 25$ (dashed magenta line), or $N_{\mathrm{PV}} = 35$ (dotted orange line) [68].

### *Residual $N_{\mathrm{PV}}$- and $\mu$-based subtraction*

Since the pile-up sensitivity differs across the detector, a residual $p_{\mathrm{T}}$ dependence on pile-up still remains after the area-based subtraction. Therefore two additional terms are subtracted based on this residual $p_{\mathrm{T}}$ dependence on $N_{\mathrm{PV}}$ and $\langle\mu\rangle$. To perform the *residual subtraction*, reconstructed jets are matched to truth jets requiring $\Delta R < 0.3$. The difference between transverse momentum of the truth jet $p_{\mathrm{T}}^{\mathrm{true}}$ and the reconstructed jet $p_{\mathrm{T}}^{\mathrm{reco}}$ is evaluated as a function of $N_{\mathrm{PV}}$ and $\mu$ to probe the dependency on both in-time and out-of-time pile-up. For both cases, the relation is approximately linear and linear fits are performed in bins of $p_{\mathrm{T}}^{\mathrm{true}}$ and $|\eta^{\mathrm{det}}|$. The fitted slopes $\alpha$ ($N_{\mathrm{PV}}$) and $\beta$ ($\mu$) are in turn seen to depend logarithmically on $p_{\mathrm{T}}^{\mathrm{true}}$ and logarithmic fits are performed over the range $20 < p_{\mathrm{T}}^{\mathrm{true}} < 200$ GeV in each $|\eta|$ bin. The fitted values at $p_{\mathrm{T}} = 25$ GeV are taken to be the nominal values of $\alpha$ and $\beta$ reflecting the $p_{\mathrm{T}}$ region where the pile-up dependence is most significant. Finally, the $\alpha$ and $\beta$ coefficients are fitted linearly across the $|\eta|$ bins to reduce the effect of statistical fluctuations and allow smooth sampling as function of $|\eta|$. Thus the final corrected $p_{\mathrm{T}}$ is given by

$$p_{\mathrm{T}}^{\mathrm{corr}} = p_{\mathrm{T}}^{\mathrm{reco}} - \rho \times A - \alpha \times (N_{\mathrm{PV}} - 1) - \beta \times \langle\mu\rangle \tag{5.1}$$

where $p_T^{\mathrm{reco}}$ is the $p_{\mathrm{T}}$ of the reconstructed jet before any pile-up removal. The result of the area-based subtraction and the residual $N_{\mathrm{PV}}$- and $\mu$-based subtraction is shown in

Figure 5.3, where the $p_{\mathrm{T}}$-dependence on $N_{\mathrm{PV}}$ and $\mu$ is plotted as a function of $|\eta^{\mathrm{det}}|$ before and after the two steps.

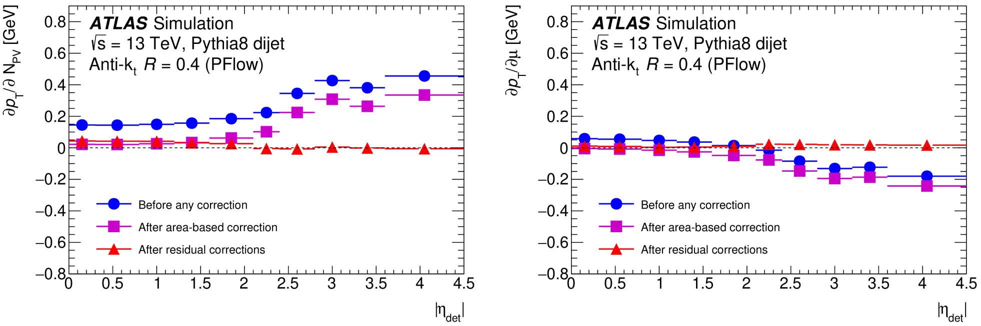

(a)

(b)

**Figure 5.3:** Dependence of the jet $p_{\mathrm{T}}$ on the number of primary vertices $N_{\mathrm{PV}}$ (a) and on the number of bunch crossings $\mu$ (b) as function of $|\eta_{\mathrm{det}}|$. Errors are smaller than the markers on the plot [68].

The difference between the nominal logarithmic fits over the range $20 < p_{\mathrm{T}}^{\mathrm{true}} < 200$ GeV and fits across the full $p_{\mathrm{T}}^{\mathrm{true}}$ range are taken as a $p_{\mathrm{T}}$-dependent systematic uncertainty on the residual pile-up dependence. In addition, three systematics are introduced to account for MC mismodeling of $\rho$, $N_{\mathrm{PV}}$, and $\mu$. The latter two uncertainties are taken as the difference between MC and data. The uncertainty in $\rho$ is estimated from the difference between various MC generators and topologies, as described in Section 5.3.

### 5.1.2 Grooming (large-$R$ jets)

Large-radius jets are especially susceptible to pile-up which affects the $p_{\mathrm{T}}$ and mass resolution. So-called "grooming" techniques are designed to reduce the contribution from pile-up and other soft and wide-angle emissions at the level of jet constituents. The purpose of removing low-energy clusters rather than modifying the mass and $p_{\mathrm{T}}$, is to also improve the resolution of variables related to the substructure of the jet. Jet substructure variables are used to characterise the radiation pattern inside the jet, and are important for identifying the kind of particle that initiated the jet. Since several interests are at stake (improve $p_{\mathrm{T}}$ and mass resolution, tagging efficiency, and stability against pile-up) several grooming techniques have been developed and are compared in combination with various jet inputs in [72]. No single configuration performs better on all metrics, so here I will focus on two standard algorithms in ATLAS, called *Trimming* and *Reclustering*, for which detailed calibrations are derived.

*Trimming*
In the Trimming algorithm, the constituents of the large-*R* jet are reclustered into smaller-radius subjets using the $k_t$ algorithm with radius parameter $R_{\mathrm{sub}}$. Subjets with $p_{\mathrm{T}}$ smaller than a fraction $f_{\mathrm{cut}}$ of the original jet $p_{\mathrm{T}}$ are removed and the four-momentum recalculated. The $k_t$ algorithm is chosen due to its sensitivity to soft particles. Since a large fraction of energy from the original particle is typically contained in one or few subjets, and the signal from pile-up, noise, and the underlying event is typically much softer, trimming is an effective way of reducing such contaminations. The parameter values chosen for the standard large-*R* jet definition are $R_{\mathrm{sub}} = 0.2$ and $f_{\mathrm{cut}} = 5\%$.

*Reclustering*
Jet Reclustering is a technique to build large-radius jets by passing jets of smaller radius to the jet finding algorithm as inputs [73]. By using anti-$k_t$ jets with $R = 0.4$, one can exploit the fact that the standard small-*R* jets are well understood and calibrated. Thus, the calibrations and corresponding uncertainties can be propagated to the reclustered (RC) jets without requiring a dedicated calibration effort. This gives more flexibility to the analyses which can optimise the jet radius to their particular signal without having to derive their own calibration. Another big advantage, and the reason Jet Reclustering is mentioned in this section, is that pile-up removal is built into the procedure. Firstly, through the advanced pile-up mitigation which small-*R* jets are subjected to, as described earlier in this section. Secondly, because additional grooming can be applied to the small-*R* jet inputs. Typically, a modified form of trimming is applied, requiring that each input jet carries at least a fraction $f_{\mathrm{cut}}$ of the total large-*R* jet $p_{\mathrm{T}}$.

## 5.2 Simulation-based calibrations

### 5.2.1 Absolute jet energy scale, mass scale, and eta calibration

A simulation-based calibration of the jet energy, mass, and $\eta$, is derived from PYTHIA 8 simulations of multijet events, in order to correct for the biases listed in the beginning of this section. The aim of the simulation-based calibrations is to restore the reconstructed the jet four-momentum to that of the *truth jets*.

The energy response, defined as $E^{\mathrm{reco}}/E^{\mathrm{truth}}$, varies across the detector, especially at the boundaries between different detector technologies and granularities. A similar behavior is seen in the rapidity bias $\Delta\eta = \eta^{\mathrm{reco}} - \eta^{\mathrm{truth}}$. Both are measured in bins of truth jet energy $E^{\mathrm{truth}}$ and detector pseudo rapidity $\eta^{\mathrm{det}}$ which is calculated relative to the geometrical centre of the ATLAS detector. The average energy response $R_E = \langle E^{\mathrm{reco}}/E^{\mathrm{truth}}\rangle$ is determined as the mean of a Gaussian fit to the response distribution in each bin and then parameterised as a function of $E^{\text{reco}}$ through numerical inversion. The reason for calculating the response in bins of $E^{\text{truth}}$ and then parameterising to get it as function of $E^{\text{reco}}$ is that the response is that for fixed $E^{\text{truth}}$ the response is Gaussian.

The energy response for PFlow jets is shown as a function of detector pseudorapidity $\eta_{\text{det}}$ and $E^{\text{reco}}$ in Figure 5.4 for a few representative bins of $E^{\text{reco}}$ and $\eta_{\text{det}}$. The characteristic structure in $\eta_{\text{det}}$ reflects the calorimeter geometry, where the barrel-endcap and endcap-forward transition regions can be clearly seen at $|\eta_{\text{det}}| \sim 1.4$ and $|\eta_{\text{det}}| \sim 3.1$, respectively.

The calibration factor $c_{\text{JES}}$ is taken as the inverse of the average energy response.

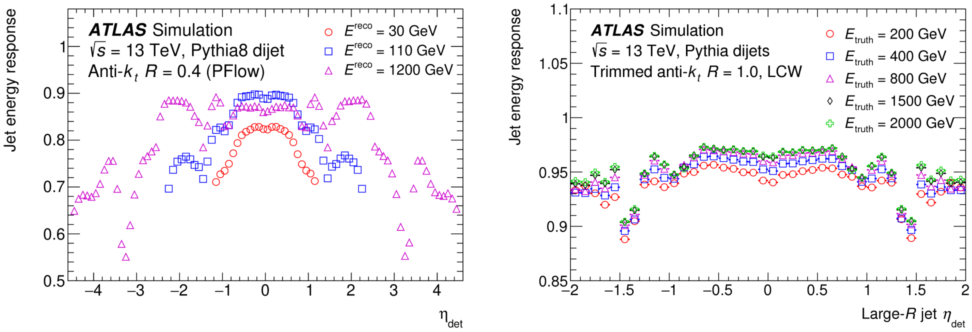

(a) (b)

**Figure 5.4:** Jet energy response for (a) small-R PFlow jets [68] and (b) large-R jets [69].

For large-$R$ jets the jet mass is also reconstructed. The jet mass is also sensitive to detector geometry and must be calibrated. The average jet mass response $R_{\text{m}} = \langle m^{\text{reco}}/m^{\text{truth}} \rangle$ is corrected through a similar procedure as the energy response. The JMS calibration is applied to the mass in addition to the JES calibration, as a function of $E^{\text{reco}}$, $\eta_{\text{det}}$, and $\log(m^{\text{reco}}/E^{\text{reco}})$. The jet energy is kept fixed while the $p_{\text{T}}$ is allowed to vary. Thus the jet kinematics, with both the JES and JMS calibration applied become:

$$E_{\text{corr}} = c_{\text{JES}} E_{\text{reco}}, \quad m_{\text{corr}} = c_{\text{JES}} c_{\text{JMS}} m_{\text{reco}},$$
$$\eta_{\text{corr}} = \eta_{\text{reco}} + \Delta\eta, \quad p_{\text{T}}^{\text{corr}} = c_{\text{JES}} \frac{\sqrt{E_{\text{reco}}^2 - c_{\text{JMS}}^2 m_0^2}}{\cosh(\eta_{\text{reco}} + \Delta\eta}) \tag{5.2}$$

### 5.2.2 Global Sequential Calibration (small-$R$ jets)

The previous calibration step corrects the jet kinematics on average, but the response can still vary from one jet to another depending on flavour, particle composition, and shower development. These fluctuations increase the jet energy resolution (JER) defined as the width of the Gaussian fit to the response. The Global Sequential Calibration (GSC) is a series of multiplicative corrections, applied to small-$R$ jets to improve the jet resolution without changing the average energy response.

The GSC consists of six steps which use observables related to energy deposits in the calorimeter, track information, and activity in the muon segments:

- The ratio of $p_{\mathrm{T}}$ calculated from ghost associated tracks to the total jet $p_{\mathrm{T}}$, $f_{\mathrm{charged}}$.
- The fraction of the jet energy measured in the first layer of the hadronic Tile calorimeter $f_{\mathrm{Tile0}}$.
- The fraction of energy measured in the third layer of the EM LAr calorimeter $f_{\mathrm{LAr3}}$.
- The number of charged tracks ghost associated to the jet $n_{\mathrm{trk}}$.
- The $p_{\mathrm{T}}$ weighted average distance between jet axis and the associated tracks $w_{\mathrm{trk}}$.
- The number of muon segments traversed by a track, ghost-associated to the jet $n_{\mathrm{MS}}$.

For each observable, a correction to the jet four-momentum is derived as a function of $p_{\mathrm{T}}^{\mathrm{truth}}$ and $|\eta_{\mathrm{det}}|$. Correlations between the observables are neglected as no improvement is found from including them or changing the order in which the corrections are applied. Two of the observables used in the GSC are shown in Figure 5.5 for illustration.

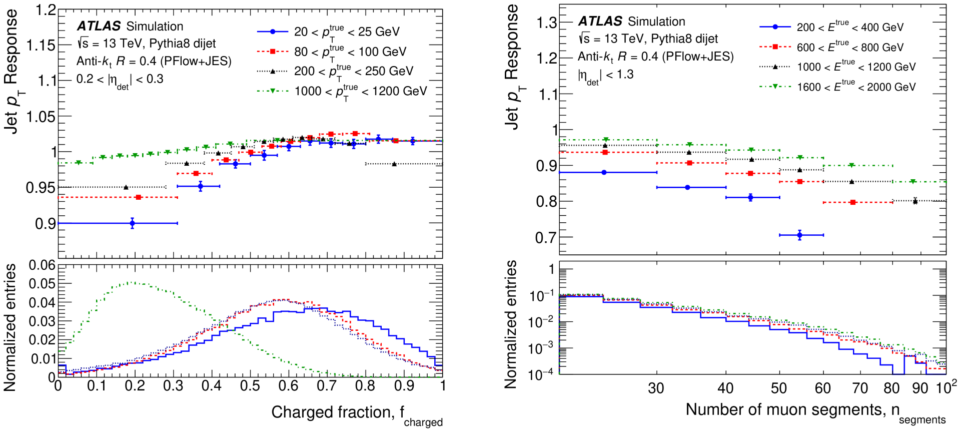

(a) (b)

**Figure 5.5:** Jet $p_{\mathrm{T}}$ response in four bins of $p_{\mathrm{T}}$, measured as a function of (a) the fraction of the jet $p_{\mathrm{T}}$ coming from charged particles, and (b) the number of muon segments with tracks associated with the jet [68].

## 5.3 *In situ* $p_{\mathrm{T}}$ calibrations

The simulation-based calibrations correct the jet energy, rapidity, and mass to the truth scale as defined by simulations. The final step of the calibration accounts for potential mismodeling in the simulations of both detector properties and physics processes. Imperfect descriptions of detector materials, detector response, jet formation, pile-up, the underlying event, particle interactions with the detector, etc. can lead to different jet responses in data and simulations. The residual *in situ* $p_{\mathrm{T}}$ calibration measures the jet $p_{\mathrm{T}}$ response in data and simulation separately and applies the ratio of the two as an additional correction factor.

Several data-driven methods are used to obtain $p_{\mathrm{T}}$ response measurements over a wide range of jet $p_{\mathrm{T}}$ and $\eta$. All *in situ* methods are based on a common principle; to use events where jet is recoiling against a well-calibrated reference object. The response $R_{\mathrm{in\,situ}}$ is defined as the average ratio of the jet $p_{\mathrm{T}}$ to to the reference object $p_{\mathrm{T}}$, measured in bins of reference object $p_{\mathrm{T}}$:

$$R_{\mathrm{in\,situ}} = \frac{\langle p_{\mathrm{T}}^{\mathrm{jet}} \rangle}{\langle p_{\mathrm{T}}^{\mathrm{ref}} \rangle} \tag{5.3}$$

By taking the response double ratio, the ratio between response in data and MC,

$$c = \frac{R_{\mathrm{in\,situ}}^{\mathrm{data}}}{R_{\mathrm{in\,situ}}^{\mathrm{MC}}} \tag{5.4}$$

effects from, for example, additional radiative jets and out-of-cone radiation cancel out. Thus the double ratio $c$ provides a robust estimate of the difference between the jet $p_{\mathrm{T}}$ response in data and simulation. It is measured in bins of reference object $p_{\mathrm{T}}$ and $\eta$, but parameterised as a function of jet $p_{\mathrm{T}}$ and $\eta$ via numerical inversion.

The *in situ* $p_{\mathrm{T}}$ calibration is very similar for small-*R* jets and large-*R* jets, but it is carried out in three stages for small-*R* jets and two stages for large-*R* jets. In both cases the first stage is the $\eta$ intercalibration. Here, the energy scale of forward jets is corrected using dijet events where the forward jet balances against a central jet. For small-*R* jets, the second step aims at correcting the lower-$p_{\mathrm{T}}$ jets by using events where the jet recoils against a photon or $Z$ boson with well-measured $p_{\mathrm{T}}$. With those two corrections applied, higher-$p_{\mathrm{T}}$ jets are corrected in a third stage by using events where one high-$p_{\mathrm{T}}$ jet is recoiling against a system of low-$p_{\mathrm{T}}$ jets, which are now well-calibrated. For large-*R* jets, however, the *multijet balance* uses a system of fully calibrated small-*R* jets as reference object, and so it is done in the same stage as the $\gamma$+jet and $Z$+jet balance. The measured response ratios from the

$\gamma/Z$+jet and MJB analyses are then combined to form a smooth and continuous calibration curve across the full $p_{\mathrm{T}}$ range.

In each analysis, there are systematic uncertainties arising from mismodeling of physics processes, uncertainty on the reference object $p_{\mathrm{T}}$, and uncertainty on the $p_{\mathrm{T}}$ balance due to the event topology. Systematics on the reference object are taken from the ATLAS recommendations. The uncertainty from mismodeling is estimated by comparing different event generators, and the uncertainty from the event topology is estimated by varying the event selections. All uncertainties are propagated to the combined results as explained in more details in Section 5.3.4.

### 5.3.1 Dijet $\eta$-intercalibration

The dijet $\eta$-intercalibration is intended to extend the calibration to the forward regions of the detector of $0.8 < |\eta| < 2.5$ for large-*R* jets and $0.8 < |\eta| < 4.5$ for small-*R* jets. In both cases, the $p_{\mathrm{T}}$ balance of the dijet system is characterised by the asymmetry defined as:

$$\mathcal{A} = \frac{p_{\mathrm{T}}^{\mathrm{probe}} - p_{\mathrm{T}}^{\mathrm{ref}}}{p_{\mathrm{T}}^{\mathrm{avg}}} \tag{5.5}$$

where $p_{\mathrm{T}}^{\mathrm{avg}} = (p_{\mathrm{T}}^{\mathrm{probe}} + p_{\mathrm{T}}^{\mathrm{ref}})/2$. For large-$R$ jets, the reference jet is required to be central ($|\eta| < 0.8$), whereas for small-$R$ the jets are only required to be in different $\eta$ regions in order to maximise statistics. The asymmetry is approximately Gaussian, thus the mean $\langle\mathcal{A}\rangle$ is determined by a Gaussian fit to the core of the distribution. A relative jet response is then defined in terms of the asymmetry as

$$R = \left\langle \frac{p_{\mathrm{T}}^{\mathrm{probe}}}{p_{\mathrm{T}}^{\mathrm{ref}}} \right\rangle = \frac{2 + \langle\mathcal{A}\rangle}{2 - \langle\mathcal{A}\rangle} \tag{5.6}$$

and measured in bins of $p_{\mathrm{T}}^{\mathrm{avg}}$ and probe jet $\eta_{\mathrm{det}}$. Also here, $\eta_{\mathrm{det}}$ is defined by the detector coordinates, since this calibration step is intended to correct for properties related to the detector geometry. The relative responses of small- and large-*R* jets are shown as a function of $\eta_{\mathrm{det}}$ for one of the $p_{\mathrm{T}}^{\mathrm{avg}}$ bins in Figure 5.6. In the region $|\eta_{\mathrm{det}}| < 0.8$, the average response is unity by construction for both data and simulation. Beyond $|\eta_{\mathrm{det}}| > 0.8$ it can be seen that, in simulation, forward jets are already corrected from the simulation-based $\eta$-intercalibration.

To ensure a clean dijet topology, events are required to not have a third jet with a significant $p_{\mathrm{T}}$ such that $p_{\mathrm{T}}^{\mathrm{J3}}/p_{\mathrm{T}}^{\mathrm{avg}} < 0.25$ for small-*R* jets and $p_{\mathrm{T}}^{\mathrm{J3}}/p_{\mathrm{T}}^{\mathrm{avg}} < 0.4$ for large-*R* jets. The two leading jets are also required to be back to back with $\Delta\phi > 2.5$ rad for both small and large-$R$ jets. Uncertainties on the response ratio, arising from the event topology, are evaluated by varying these cuts.

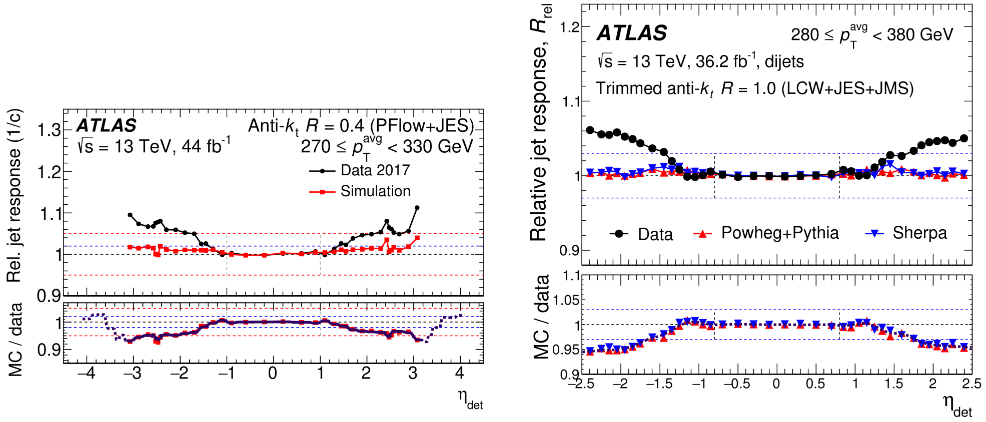

(a)

(b)

**Figure 5.6:** The relative $p_{\mathrm{T}}$ response as function of $\eta_{\mathrm{det}}$ for (a) small-$R$ jets [68] and (b) large-$R$ jets [69]. The response is shown in one representative bin of $p_{\mathrm{T}}^{\mathrm{avg}}$ for each jet type. It is measured in both data and simulation (with two different generators for large-$R$ jets) and the lower panels show the response ratio of simulation to data.

### 5.3.2 $Z$+jet and $\gamma$+jet balance

Following the relative $\eta$-intercalibration, the absolute jet $p_{\mathrm{T}}$ response is measured up to about $p_{\mathrm{T}} = 1\,\mathrm{TeV}$ using events with a jet recoiling against a photon or a leptonically decaying $Z$ boson. The response is measured separately for three different reference objects - photon, $Z \rightarrow e^+e^-$ and $Z \rightarrow \mu^+\mu^-$ - providing independent and precise constraints on the jet energy. Only the central region of the detector ($|\eta| < 0.8$) is used for this calibration and the $\eta$-intercalibration allows the correction to be translated to the forward part of the detector. A cut is placed on $\Delta\phi$ between the jet and reference object $Z$ og $\gamma$ to reduce the effect of initial or final state radiation.

For the small-$R$ jet calibration the reference object is balanced against the full hadronic recoil in the event. This approach is robust to both pile-up and underlying event, which cancel directionally on average over a large collection of events, and is less affected by jet definitions since these become relevant only in the application of the calibration.

For large-$R$ jets, direct balance between reconstructed jet and reference object is used, since part of the full hadronic recoil is removed by the trimming, described in Section 5.1.

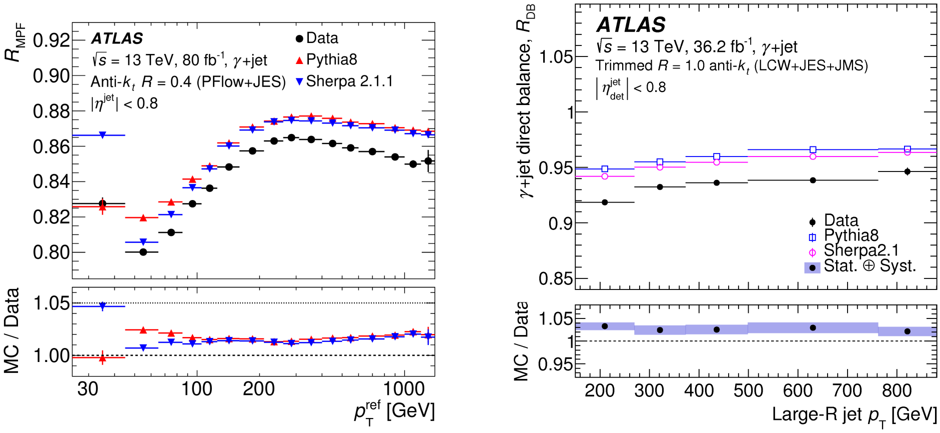

(a) (b)

**Figure 5.7:** Jet $p_{\mathrm{T}}$ response measured in $\gamma$+jet events for (a) small-$R$ jets [68] and (b) large-$R$ jets [68].

### 5.3.3 Multijet balance

The $Z$+jet and $\gamma$+jet balance methods only constrain the JES up to about 1 TeV. To measure the response of higher $p_{\mathrm{T}}$ jets, events are used where the probe jet is recoiling against a system of multiple low $p_{\mathrm{T}}$ jets. Thereby, the multijet balance extends the calibration up to $p_{\mathrm{T}} = 2.4\,\mathrm{TeV}$ for small-$R$ and $p_{\mathrm{T}} = 3.0\,\mathrm{TeV}$ for large-$R$ jets. In the case of small-$R$ jets, the energy scale of the low $p_{\mathrm{T}}$ jets in the reference system is corrected according to the combined result of the $Z$+jet and $\gamma$+jet balance. For large-$R$ jets, the reference system is built out of fully calibrated small-$R$ jets.

### 5.3.4 Nominal combination of *in situ* $p_{\mathrm{T}}$ calibrations

The response ratios measured by the four *in situ* methods are combined to form a continuous and smooth calibration curve across the full range of jet $p_{\mathrm{T}}$. The different statistical and systematic uncertainties of each measurement are propagated to the combined results taking into account their correlations. The combination is carried out via the following steps:

**Interpolation:** Each set of measurements is interpolated using second degree polynomial splines which are then evaluated at small (1 GeV) $p_{\mathrm{T}}$ bins.

**Averaging:** For every small $p_{\mathrm{T}}$ bin, a weighted average of the *in situ* methods contributing in that bin is computed based on a $\chi^2$-minimisation. The weights account for the

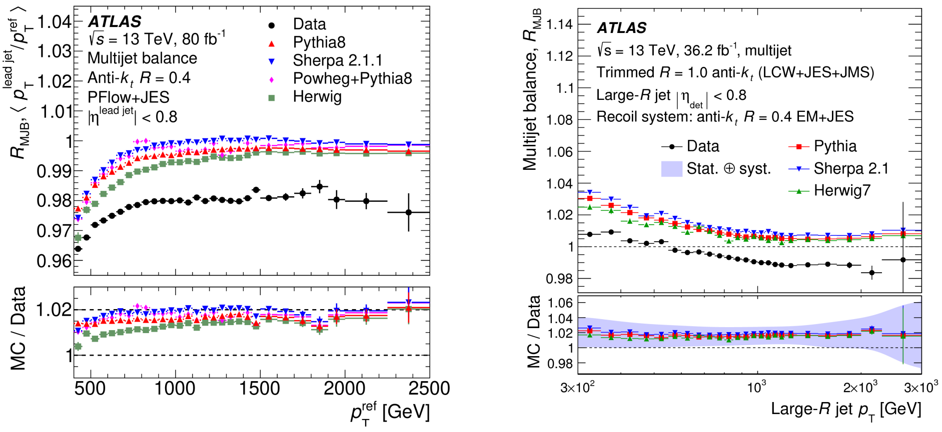

(a) (b)

**Figure 5.8:** Response of leading jet $p_{\mathrm{T}}$ measured in multijet events, for (a) small-$R$ jets [68] and (b) large-$R$ jets [69]. In both cases the reference system of low-$p_{\mathrm{T}}$ jets is reconstructed with $R = 0.4$.

uncertainties, their correlations, and the width of the original bins.

**Monte Carlo pseudo experiments:** To propagate the uncertainties to the combined curve, the whole procedure is repeated multiple times, while coherently shifting the response ratios measured by the *in situ* methods by one standard deviation of a given uncertainty. By comparing the combined curve obtained with the shifted and the nominal inputs, the uncertainties are determined.

**Uncertainty combination:** The many individual uncertainties are combined to a single *in situ* uncertainty, taking into account their correlations. Uncorrelated terms are added in quadrature, while terms that are significantly correlated are treated as fully correlated and added linearly.

**Uncertainty scaling:** The reduced $\chi^2$ is evaluated in each small $p_{\mathrm{T}}$ bin, and is defined as $\sqrt{\chi^2/N_{\mathrm{dof}}}$, where $N_{\mathrm{dof}}$ is the number of degrees of freedom given by the number of *in situ* methods contributing to the average in that bin. To account for potential disagreements between the measurements, every uncertainty source is scaled by a factor of $\sqrt{\chi^2/N_{\mathrm{dof}}}$, if that factor is larger than 1.

**Smoothing:** Finally, a smoothing procedure is applied to the response ratio curve and all associated uncertainties. The smoothing is done using a variable-size sliding window with a Gaussian kernel, thereby removing spikes that are unphysical, and discontinuities at the first and last bins of each method.

The result of the combination for both small- and large-$R$ jets, is shown in Figure 5.9 along with the individual response ratio measurements as a function of $p_{\mathrm{T}}$. To complete the calibration, the inverse of the solid curve is applied as a correction factor to data.

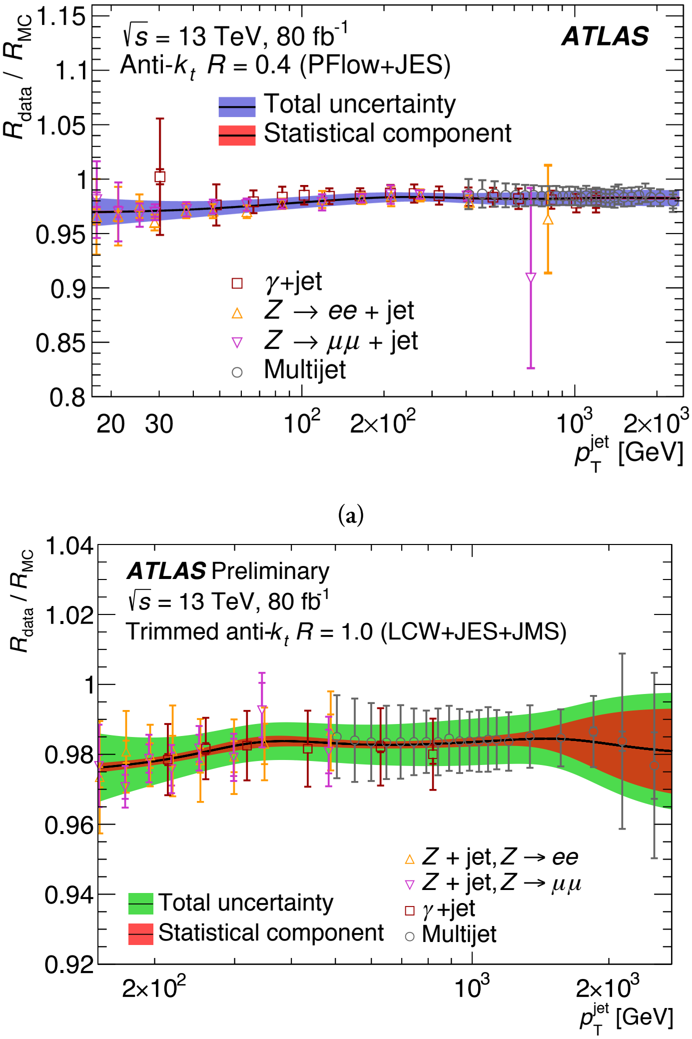

(a)

(b)

**Figure 5.9:** Combined data-to-simulation $p_{\mathrm{T}}$ response ratio for (a) small-$R$ jets [68] and (b) large-$R$ jets [74]. The solid black curve is the result of combining three *in situ* methods: $\gamma$+jet (red, open squares), $Z$+jet (pink and orange triangles triangles), and multijet balance (gray, open circles). The purple/green bands illustrates the total uncertainty propagated to the combined curve for small/large-R jets, and the red bands correspond to the statistical components.

The relative weights given to each *in situ* measurement when taking the average is shown as a function of $p_{\mathrm{T}}$ in Figure 5.10. For both jet types, the $Z$+jet method dominates in the low $p_\mathrm{T}$ range ($p_\mathrm{T} < 500\,\mathrm{GeV}$). The multijet balance starts to take over at 500 GeV for large-$R$ jets, where the $\gamma$+jet balance has the highest weight for small-$R$ jets. In both cases, the multijet balance provides the only measurements and thus has a weight of one from about 1 TeV.

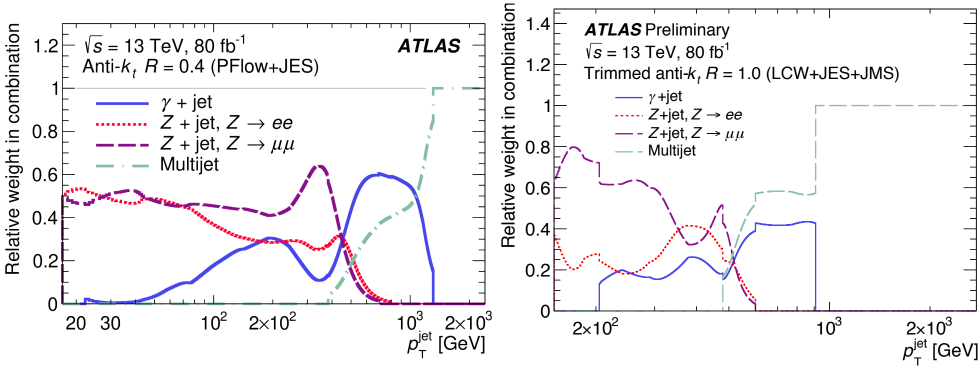

(a)

(b)

**Figure 5.10:** The weights applied in to the different *in situ* methods in the combination of the jet $p_\mathrm{T}$ response ratios as function of $p_\mathrm{T}$ for (a) small-$R$ jets [68] and (b) large-$R$ jets [74]. For each 1 GeV $p_\mathrm{T}$ bin, the $\gamma + jet$ weight is shown in purple, $Z$+jet in red, and multijet balance in green.

In Figure 5.11 the reduced $\chi^2$, illustrating the local tension between methods in the combinations, is shown as a function of $p_\mathrm{T}$. In the case of small-$R$ jets, there are a few spikes which exceed 1 and so the systematic uncertainties are scaled by $\sqrt{\chi^2/N_\mathrm{dof}}$ in those regions. No scaling og uncertainties is done for large-$R$ jets.

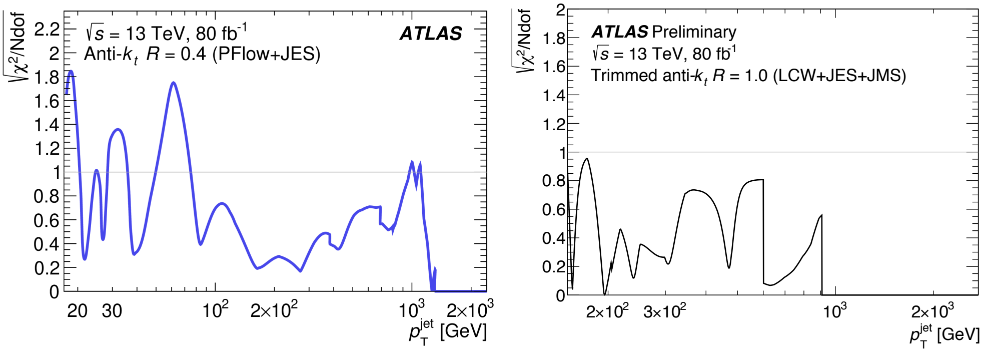

(a)

(b)

**Figure 5.11:** The $\sqrt{\chi^2/N_\mathrm{dof}}$ of the weighted average as a function of the large-$R$ jet $p_\mathrm{T}$ for (a) small-$R$ jets [68] and (b) large-$R$ jets [74]. The reduced $\chi^2$ illustrates the compatibility of the methods being combined.

### 5.3.5 Alternative fit-based *in situ* combination

The combination procedure, described above is used for the nominally recommended JES calibration. However, a different procedure was developed for a search of low-mass dijet resonances using trigger-level jets [75] with data collected in 2016.

The search for lighter resonances at LHC generally suffer from restrictions on the data-taking rate. The limited bandwidth necessitates that single-jet triggers with a $p_{\mathrm{T}}$ threshold below 380 GeV are prescaled, whereby dijet events with an invariant mass below 1 TeV are largely discarded. To access the invariant mass spectrum below 1 TeV, the dijet trigger-level analysis (TLA) makes use of a data taking strategy, where only a subset of the event information is recorded. This allows for prescaling can be avoided and much more data to be recorded. The strategy has previously been used by the CMS collaboration for a dijet resonance search [76] and within the LHCb collaboration [77].

Due to the frequency of low-$p_{\mathrm{T}}$ triggers, the data sample analysed by the TLA is very large. The small statistical uncertainties makes the search more sensitive to fluctuations in the jet energy calibration. In the 2016 data set, the nominal *in situ* combination procedure, based on splines, introduced a feature in the calibration curve for jet $p_{\mathrm{T}}$ of about 300 GeV, as can be seen in Figure 5.12. The kink corresponded to the location where there was a disagreement between the $\gamma$+jet measurement and the $Z$+jet measurement. So for the calibration of trigger-level jets, the steps of interpolation, averaging and smoothing were replaced by a single polynomial fit. A fourth order polynomial in $\log(p_{\mathrm{T}})$ was fitted to the three sets of measurements simultaneously. The fit function $f$ was chosen to have good agreement to the nominal calibration curve and uncertainties of similar magnitude:

$$\begin{aligned} f(p_{\mathrm{T}}) = a_{n1} \cdot (\log p_{\mathrm{T}})^{-1} + a_0 + a_1 \cdot \log p_{\mathrm{T}} + a_2 \cdot (\log p_{\mathrm{T}})^2 && (5.7) \\ + a_3 \cdot (\log p_{\mathrm{T}})^3 + a_4 \cdot (\log p_{\mathrm{T}})^4 + \text{high-}p_{\mathrm{T}}\text{ constraint} && (5.8) \end{aligned}$$

A comparison between the nominal calibration and the fit-based calibration is shown in Figure 5.12. From the ratio panel, it can be seen that the largest difference is around the fluctuation at 300 GeV.

The spline-based combination is still preferred as the nominal procedure, because it avoids assuming a functional form. However, local $p_{\mathrm{T}}$ dependent fluctuations of the detector response are not physical either. In the high-statistics era we are entering with the ongoing upgrades of the LHC, even small fluctuations might be significant for other analyses than the TLA. Therefore, the fit-based combination procedure, which guarantees a smooth calibration curve, is expected to become more widely applied.

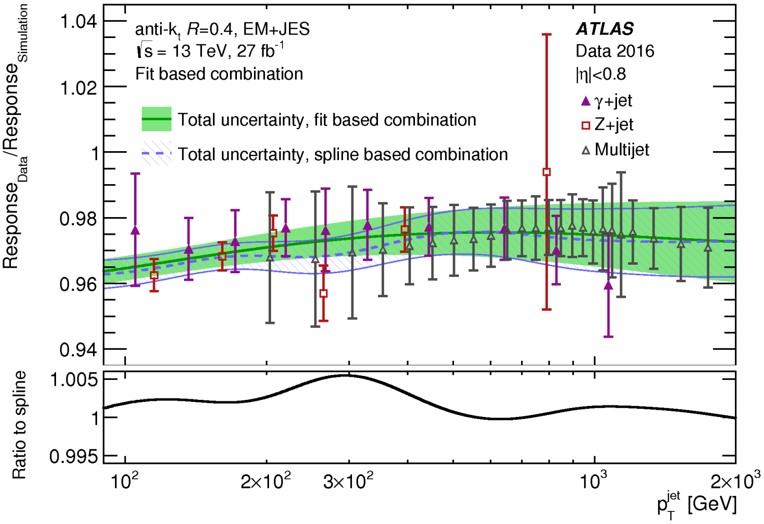

**Figure 5.12:** Ratio of the small-$R$ (EM) jet $p_{\mathrm{T}}$ response measured in simulation and data with three different *in situ* methods; $\gamma$+jet (purple, solid triangles), $Z$+jet (red, open squares), multijet balance (grey, open triangles). The green band shows the result of the fit-based combination which is compared to the nominal combination overlaid as a dashed band. The lower panel shows the ratio between the center of the two bands, illustrating that the main difference is observed around 300 GeV [75].

### 5.3.6 Systematic uncertainties

Numerous individual components contribute to the total uncertainty of the jet energy scale. The majority stem from the *in situ* methods, from pile-up effects, and flavour dependence. Terms derived from the *in situ* methods cover effects related to the physics modeling and simulation, topology and calibration of the reference systems, the event selections, and the statistical limitations.

For the small-$R$ jet calibration, these amount to 125 individual terms, the total of which are shown in Figure 5.13 and described in detail in [68]. The uncertainty components from the $\eta$-intercalibration are labeled 'Relative *in situ* JES'. The asymmetric peaks around $\eta = \pm 2.5$ are caused by a discrepancy between data and simulation in the $\eta$-intercalibration.

The combined uncertainties from all other *in situ* measurements are labelled 'Absolute *in situ* JES'. The absolute *in situ* JES uncertainty increases drastically at large $p_{\mathrm{T}}$, where the MJB no longer has statistical power. In this region the uncertainty is derived from studies of the response to individual hadrons [78].

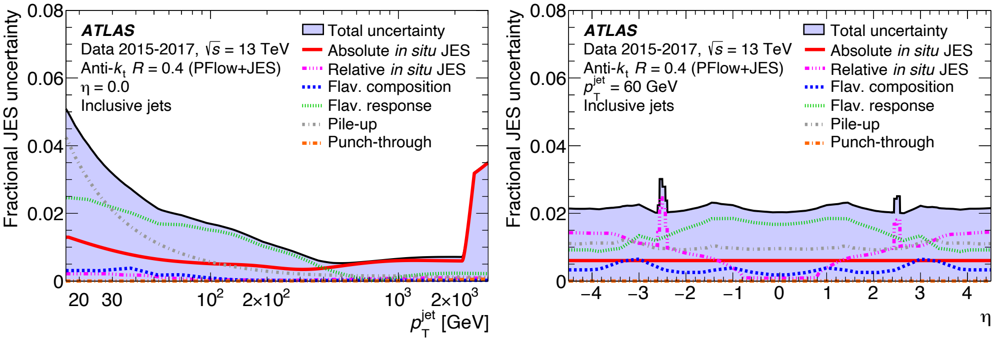

(a) (b)

**Figure 5.13:** Fractional jet energy scale systematic uncertainty components for small-$R$ PFlow jets as a function of jet $p_T$ (a) and detector $\eta$ (b). The total uncertainty, determined as the quadrature sum of all components, is shown as a filled region topped by a solid blackline. Flavour-dependent components shown here assume a dijet flavour composition [68].

The detailed information contained in the many individual uncertainty components is not needed for most analysis, however the correlations between the jet energy scale at different $p_T$ and $\eta$ can be significant. Therefore, the uncertainty components stemming from the *in situ* methods are reduced to a set of fewer nuisance parameters, providing a simplified description without much loss of correlation information. Several reduction schemes are offered based on eigenvector decomposition of the covariance matrix of the uncertainties. The largest resulting terms are then kept as a set of effective nuisance parameters. To determine how many of the orthogonal terms to keep, the covariance matrix of the reduced set of nuisance parameters is also computed and the difference between that and the covariance matrix of the full set is calculated. An additional term is added to the reduced set until the difference, which can be seen as a measure of the information lost, is below some fixed value (usually 0.05).

Since the large-$R$ multijet balance method uses small-$R$ jets as a reference system, all small-$R$ uncertainties are propagated to the large-$R$ calibration in addition to the large-$R$ specific components. In Figure 5.14 the uncertainty components of the large-$R$ jet calibration are presented. The green area represents the former uncertainty estimate for large-$R$ jets, which was based on $R_{\mathrm{trk}}$ measurements alone. The full *in situ* calibration is seen to reduce the large-$R$ jet $p_T$ uncertainty by up a factor of five. Uncertainty reductions are not produced for large-$R$ jets.

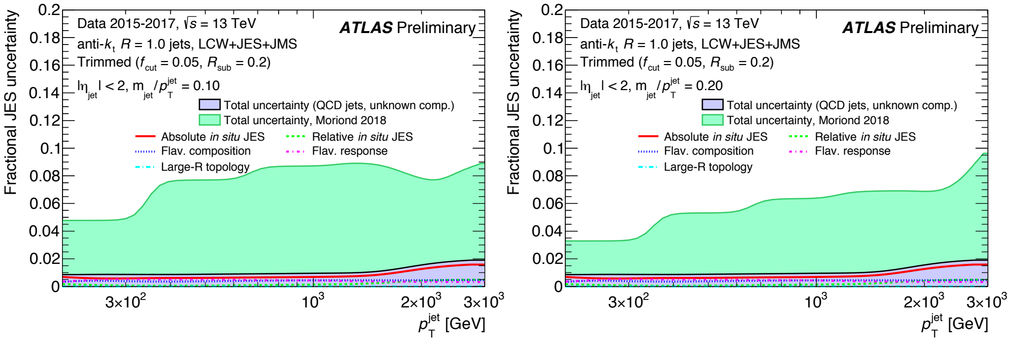

(a) (b)

**Figure 5.14:** Fractional jet energy scale systematic uncertainty components as a function of jet $p_\mathrm{T}$ for trimmed large-$R$ jets with (a) $m/p_\mathrm{T} = 0.1$ and (b) $m/p_\mathrm{T} = 0.2$. The total uncertainty, given by the quadrature sum of all components, is shown as a purple filled region topped by a solid line. Topology- and flavour-dependent components are shown under the assumption of a jet resulting from a high-energy light quark or gluon, with unknown composition. A comparison is made to the preceding uncertainties, which were based on $R_\mathrm{trk}$ measurements alone and are indicated by an additional green filled region [74].

## 5.4 *In situ* mass calibration (large-$R$ jets)

For large-$R$ jets, an *in situ* correction to the mass calibration is applied in addition to the eta and JES calibrations. This section describes the two methods that are used to derive the correction; the $R_\mathrm{trk}$ method [79] which uses the tracker to provide a measure from the jet mass, independent from the calorimeter, and the Forward Folding method [80] which fits the $W$ and top mass peaks to get the mass scale and resolution in data and simulation. Both measurements are performed after applying the full JES calibration, since that also affects the jet mass.

### 5.4.1 Calorimeter-to-tracker ratio, $R_\mathrm{trk}$

The $R_\mathrm{trk}$ method makes use of the fact that the calorimeter and tracker provide independent measurements of the jet mass. Therefore, comparing the average calorimeter-to-tracker mass ratio

$$R^m_\mathrm{trk} = \left\langle \frac{m^\mathrm{calo}}{m^\mathrm{track}} \right\rangle \tag{5.9}$$

in data and simulation, allows to validate the modeling of jet mass. The method is versatile and can be used to similarly for other jet quantities, such as $p_{\mathrm{T}}$ and substructure variables.

To estimate the modeling uncertainty, the ratio is measured for three different simulation generators. The uncertainty due tracking effects is obtained by measuring the ratio with the baseline simulation, Pythia, for three variations in the tracking that assume different sources of tracking errors (resolution, efficiency in dense environments, and alignment). Due to the large statistics of dijet samples, the measurement can be done in multiple bins of $p_{\mathrm{T}}$, mass, and $m/p_{\mathrm{T}}$. In Figure 5.15 is the calorimeter-to-tracker response is shown for data and three different generators, along with the ratio of the response in data and simulation.

Due to the large generator uncertainty, the $R_{\mathrm{trk}}$ method does not provide any additional constraint to the $p_{\mathrm{T}}$ calibration, but rather an independent cross-check of JES calibration.

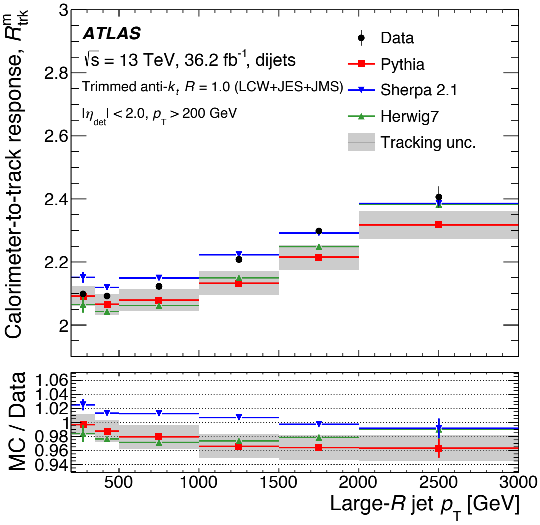

**Figure 5.15:** Measurements of the calorimeter-to-track response $R^{m}_{\mathrm{trk}}$ as function of jet $p_{\mathrm{T}}$ in data and for three different generators. The double ratio of the response measured in data and simulation is shown in the lower panel [69].

## 5.4.2 Forward Folding

A sample of $p_{\mathrm{T}}$ top quarks and $W$ bosons is obtained by selecting events where a hadronically decaying top is balancing against a leptonically decaying $W$ and $b$ quark. Since the "true" masses of these particles are known, the mass response can be obtained b fitting the $W$ and top quark mass peaks in the large-$R$ jet invariant mass spectrum of the hadronically decaying top candidate.

The event selection is based on the ATLAS $t\bar{t}$ resonance search which requires a high $p_{\mathrm{T}}$

muon and a significant missing transverse momentum.

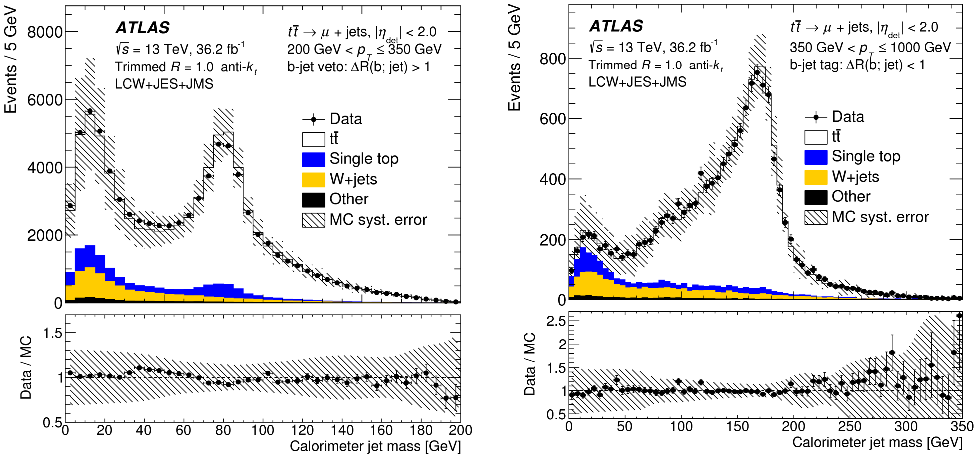

(a) (b)

**Figure 5.16:** The distribution of the large-$R$ jet mass in data samples enriched with $W$ bosons (a) and top quarks(b). The lower panel show the data-to-simulation ratio of the event yield[69].

### 5.4.3 Combination of *In situ* mass calibrations

The combination of the mass response ratios measured with the $R_{\text{trk}}$ and Forward Folding methods, is performed in the same manner as for the $p_{\text{T}}$ responses. The only difference is that the combination is done in two mass ranges separately. In Figure 5.17 the combined result can be seen for both the lower mass window of $50\,\text{GeV} < m < 120\,\text{GeV}$, corresponding to the $W$ boson mass peak, and the higher mass window $120\,\text{GeV} < m < 300\,\text{GeV}$, corresponding to the top quark mass peak. Forward folding constrains the calibration below 1 TeV by providing four measurements with small uncertainties. The $R_{\text{trk}}$ method makes use of the large data sample to extend the calibration to 2 TeV with a fine binning.

The uncertainty components contributing to the combined jet mass response curve, are shown in Figure 5.18. In both mass bins, the dominant uncertainty for $R_{\text{trk}}$, across most of the $p_{\text{T}}$ range, is related to the modeling used for the event generation. In the Forward Folding technique, the event selection introduces and equally large uncertainty in the low mass bin, and the dominant uncertainty in the higher mass bin.

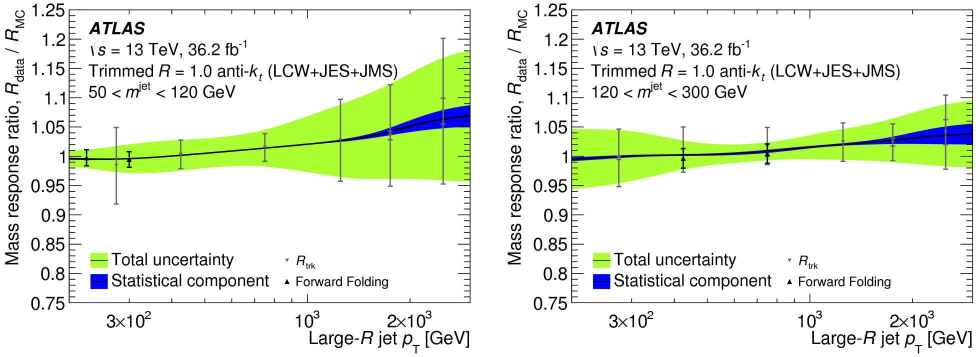

(a) (b)

**Figure 5.17:** Ratio of jet mass response in simulation and data, measured with the $R_{\mathrm{trk}}$ method shown in grey and the Forward Folding method shown in black. On the left hand plot is shown the lower mass window, corresponding to the $W$ mass peak, and on the right is shown the result in the higher mass window, corresponding to the top quark peak. The combined uncertainties are shown as a green band around the calibration curve, with the statistical component shown in blue [69].

## 5.5 Jet energy resolution

To understand the uncertainties of physics measurements and searches done with jets, precise knowledge of the jet energy resolution (JER) is required. Good energy resolution is also necessary for measuring missing transverse momentum, which is essential to many searches for physics beyond the Standard Model. Where the JES is typically taken as the mean of a Gaussian $p_{\mathrm{T}}$ response distribution in a given bin, the JER is extracted from the width of that distribution. It can be parameterised as a function of transverse momentum, using the dependence expected for calorimeter-based resolution with three independent terms:

$$\frac{\sigma(p_{\mathrm{T}})}{p_{\mathrm{T}}} = \frac{N}{p_{\mathrm{T}}} \oplus \frac{S}{\sqrt{p_{\mathrm{T}}}} \oplus C \tag{5.10}$$

The noise term $N$ accounts for electronic noise and contributions from pile-up, the stochastic term $S$ accounts for statistical Poisson fluctuations and the constant term $C$ for captures fluctuations that contribute a constant factor of the jet $p_{\mathrm{T}}$, such as signal loss in passive detector material.

For both small- and large-$R$ jets, the $p_{\mathrm{T}}$ resolution measurement relies primarily on the momentum balance between the two leading jets in dijet events. As for the dijet-$\eta$-intercalibrations,

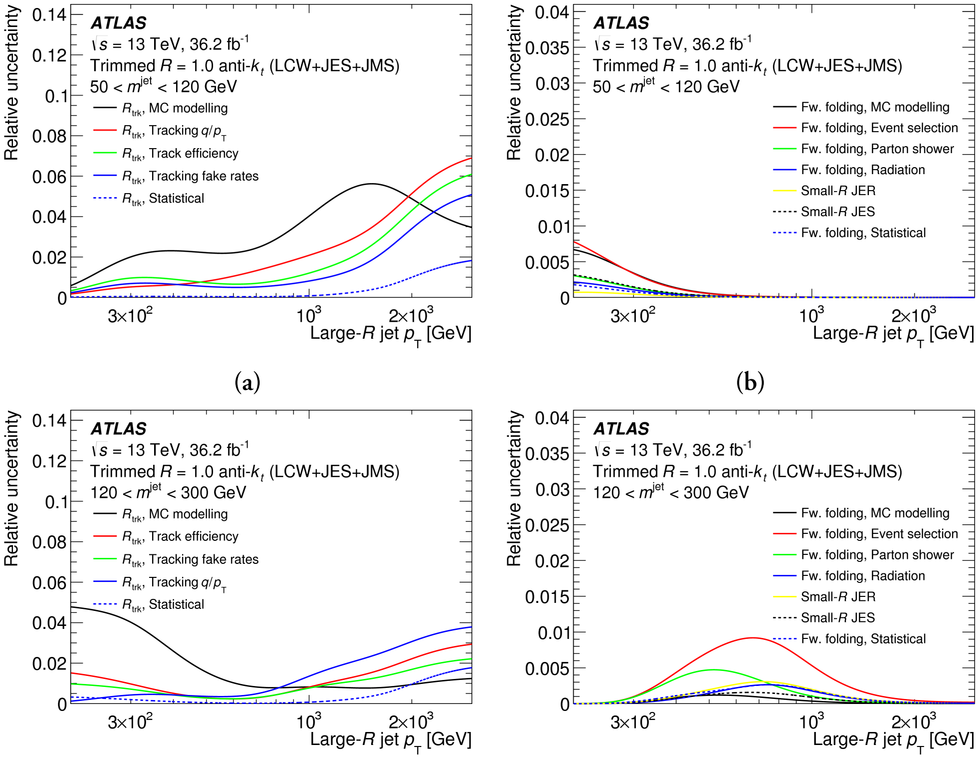

(a) (b)

(c) (d)

**Figure 5.18:** Breakdown of the various uncertainty components, which are propagated to the combined mass response ratio, as function of jet $p_{\mathrm{T}}$ [69].

deviations from exact balance are given by the asymmetry:

$$\mathcal{A} = \frac{p_{\mathrm{T}}^{\mathrm{probe}} - p_{\mathrm{T}}^{\mathrm{ref}}}{p_{\mathrm{T}}^{\mathrm{avg}}} \tag{5.11}$$

and likewise, the event selections follow those outlined in Section 5.3.1.

The measured $p_{\mathrm{T}}$ balance is affected by several particle-level effects that may lead to particle losses and additions in the measured jet $p_{\mathrm{T}}$, such as additional radiation, hadronisation and multi-parton interactions. Therefore, the width of the asymmetry distribution is a convolution of the detector resolution and those effects. To isolate the intrinsic detector resolution $\sigma_{\mathrm{det}}$, the asymmetry width is also computed for truth jets and subtracted from the measured width of reconstructed jets in quadrature:

$$\sigma_{\mathcal{A}}^{\mathrm{det}} = \sigma_{\mathcal{A}}^{\mathrm{reco}} \ominus \sigma_{\mathcal{A}}^{\mathrm{truth}}. \tag{5.12}$$

Since the resolution of both jets contribute to the width of the asymmetry, the resolution of the reference jet probe is subtracted from the asymmetry width to obtain the resolution of the reference jet:

$$\left\langle \frac{\sigma_{p_{\mathrm{T}}}}{p_{\mathrm{T}}} \right\rangle^{\mathrm{probe}} = \sigma_{\mathcal{A}}^{\mathrm{det}} \ominus \left\langle \frac{\sigma_{p_{\mathrm{T}}}}{p_{\mathrm{T}}} \right\rangle^{\mathrm{ref}}, \tag{5.13}$$

The resolution of the reference jets can be found in events where both jets are central and thus contribute equally as

$$\left\langle \frac{\sigma_{p_{\mathrm{T}}}}{p_{\mathrm{T}}} \right\rangle^{\mathrm{ref}} = \frac{\sigma_{\mathcal{A}}^{\mathrm{det}}}{\sqrt{2}} \tag{5.14}$$

For small-$R$ jets the noise term is constrained independently from the two others in Equation 5.10. Fluctuations due to pile-up are measured in an unbiased data sample collected with random trigger. The measurement is done using a method called *random cones*, where two cones are constructed by summing the energy deposits within two randomly located circular areas of a size similar to the catchment area of anti-$k_t$ jets. The $p_{\mathrm{T}}$ difference of the two cones $\Delta p_{\mathrm{T}}^{\mathrm{RC}}$ is sampled over many events to provide a measure of the random fluctuations in the energy deposition. The pile-up noise $N_{\mathrm{PU}}$ is then determined as the half width of the $\Delta p_{\mathrm{T}}^{\mathrm{RC}}$ distribution:

$$N^{\mathrm{PU}} = \frac{\sigma_{\mathrm{RC}}}{2\sqrt{2}} \tag{5.15}$$

where $\sigma_{\mathrm{RC}}$ is the 68% confidence interval, and the width is divided by $\sqrt{2}$ to obtain the fluctuations due to the single cone. The measurement is done in bins of $\eta$ and pile-up levels $\mu$.

Another contribution to the noise term of the jet energy resolution comes from electronic noise. The random cones method is insensitive to this due to the noise suppression of the topoclustering algorithm. Therefore, the electronic noise is estimated by fitting the JER in a dijet simulation sample with no pile-up.

The contributions due to pile-up and electronic noise are added in quadrature to constitute the total noise term of Equation 5.10. The full JER is then obtained by performing a fit to the dijet balance measurements with the noise term held fixed. The implementation is similar to that of the JES combination, where the full set of uncertainties are first propagated to the fit result using pseudo experiments, and then reduced by eigenvalue decomposition to a smaller number of nuisance parameters. The combined JER as function of jet $p_T$ is shown for PFlow jets in Figure 5.19.

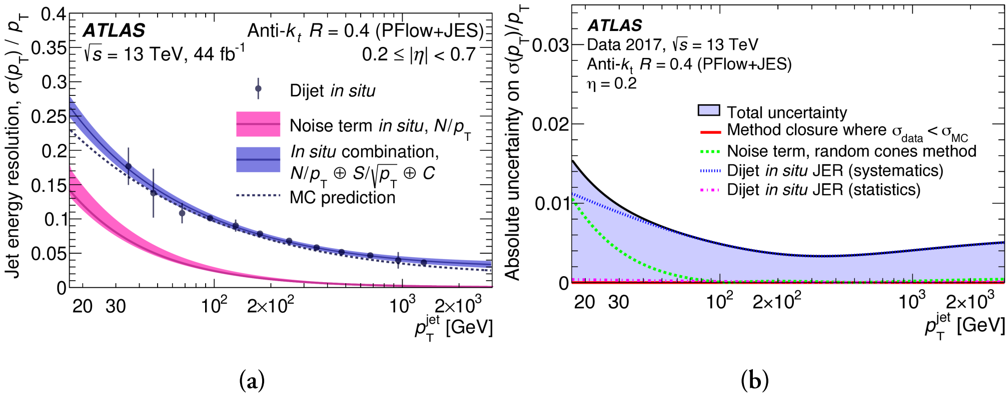

**Figure 5.19:** The relative jet energy resolution as a function of $p_T$ for small-$R$ jets. The error bars on the data points indicate the total uncertainties on the relative resolution measured in dijet events. The noise term measurement is shown separately in the pink band and the combination of the noise term and dijet measurements in purple. The expected resolution from Monte Carlo simulation is also shown for comparison. (b) Absolute uncertainty on the relative jet energy resolution as a function of jet $p_T$. Uncertainties from the two in situ measurements and from the data/simulation difference are shown separately [68].

# Chapter 6

# Jet Substructure and Tagging

Well-reconstructed and calibrated jets hold information about the kinematics of the particle that initiated the jet. In order to identify what *kind* of particles it was, we must look inside the jet.

It is essential for the ATLAS physics program to be able to identify, or “tag”, heavy particles, such as $W/Z$ bosons, top quarks, and potential new resonances. To fully exploit the available energies at the LHC for new physics searches and measurements, it is particularly important to identify the highest $p_{\mathrm{T}}$ signatures of these objects.

The higher $p_{\mathrm{T}}$ a heavy particle is created with, the more boosted the decay system becomes in the reference frame of the detector, and so the more collimated the decay products will be. But even if the decay products can not be resolved as individual jets, they can be visible by the internal structure of the resulting large-radius jet. Thus, by characterising the jet substructure we can differentiate between jets originating from light quarks, gluons, and heavy particles that decay hadronically.

In this chapter we will present some of the commonly used jet substructure variables, highlighting along the way a few examples of tagging algorithms that utilise these variables. Finally, we take a closer look at the identification of jets which include a $b$-hadron, since “$b$-tagging” relies on other techniques than the traditional jet substructure observables.

## 6.1 Jet substructure variables

The term, jet substructure variables, refers to any quantity made from the number, energies, or locations of jet constituents. These variables can be categorised as either related to the amount of radiation that the original parton emitted, here called "multiplicity-like" variables, or the extend to which the constituent are clustered into individual subjets, here called "prong-like" variables.

The jet mass is also categorised as a substructure variable. Particularly the combined mass, defined in Section 4.4, is a powerful discriminant for the classification of jets originating from heavy Standard Model particles. The reconstruction and calibration of jet mass has been described in detail in the previous two chapters and is not discussed further here.

### 6.1.1 Prong-like variables

At the energy frontier, $W$ bosons, $Z$ bosons, and top quarks are often produced with a boost so large that the decay products are captured by a single large-radius jet. The internal energy structure of the jet can reveal whether the constituents are clustered around two or more separate axes, as illustrated in Figure 6.1. There are several variables on the market, designed to identify such prongs.

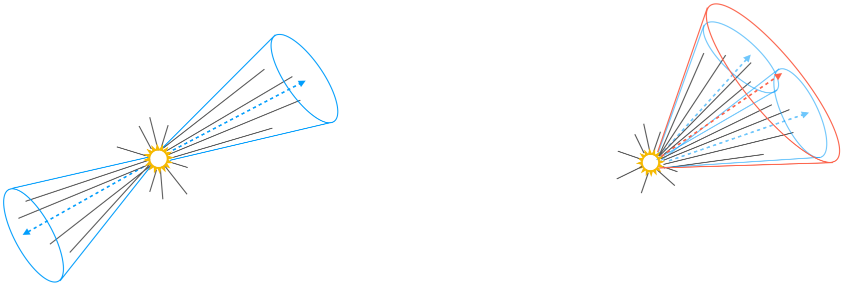

**(a)** Non-boosted decay **(b)** Highly boosted decay

**Figure 6.1:** Cartoon of two hadronic decays; In (a) the decaying particle has low momentum compared to its mass. The decay products form two jets back-to-back. In (b) the decaying particle has a large momentum compared to its mass. The decay products form a single large-radius jet with two distinguishable subjets inside.

*N-subjettiness ratios*

In order to quantify how well a jet is described by $N$ subjets, the "$N$-subjettiness" variables $\tau_N$ can be defined with respect to $N$ candidate subjet axes [81]:

$$\tau_N = \frac{1}{d_0} \sum_k p_{\mathrm{T}k} \times \min(\Delta R_{1k}, \Delta R_{2k}, ..., \Delta R_{Nk}) \tag{6.1}$$

Here $k$ runs over all the constituents (e.g. topoclusters or PFlow objects) of the jet, $p_{\mathrm{T}k}$ is the transverse momentum of constituent $k$, and $\Delta R_{Jk} = \sqrt{(\Delta\eta)^2 + (\Delta\phi)^2}$ is the Euclidian distance in the rapidity-azimuth plane between constituent $k$ and candidate subjet axis $J$. The candidate subjets are usually defined by the exclusive $k_t$ algorithm, which can be forced to return exactly $N$ jets. The normalisation factor $d_0$ is given by

$$d_0 = \sum_k p_{\mathrm{T}k} \times R \tag{6.2}$$

where $R$ is the radius parameter of the original jet.

The definition of $\tau_N$ given in Equation 6.1 is linear in each of the constituent particle momenta, which means the addition of infinitesimally soft particles does not change the value. Similarly, the value of $\tau_N$ is not changed by the addition of infinitesimally collinear splittings. This makes $N$-subjettiness an infrared and collinear safe observable.

This way, a jet where all the radiation is aligned with $N$ or fewer subjet axes will have $\tau_N \sim 0$. If a large amount of the radiation is not aligned with the $N$ candidate subjet axes, the jet will have $\tau_N \gg 0$, indicating that the jet is better described by at least $N+1$ subjets. However, $\tau_N$ alone is not and ideal discriminator, since even light quark jets can have $\tau_1 \gg 0$. Instead it is the ratios $\tau_N/\tau_{N-1}$ which are typically used to quantify to what degree the jet can be regarded as "$N$-prong". One example is the ratio $\tau_{32} = \tau_3/\tau_2$ which is the strongest single discriminating variable for identifying jets that are initiated by a top quark.

*Energy correlation ratios*

The degree to which the jet constituents are clustered can also be quantified independently of candidate subjets. The method is based on $N$-point energy correlation functions (ECF), defined as

$$\mathrm{ECF}(N,\beta) = \sum_{i_1<i_2<\ldots<i_N\in J} \left(\prod_{a=1}^{N} p_{\mathrm{T}}^{i_a}\right) \left(\prod_{b=1}^{N-1} \prod_{c=b+1}^{N} \Delta R_{i_b i_c}\right)^{\beta} \tag{6.3}$$

where the sum runs over all constituents in the jet $J$. Each term consists of $N$ transverse momenta $p_{\mathrm{T}}$ multiplied with $\binom{N}{2}$ Euclidian distances $\Delta R_{ij}$ raised to the exponent $\beta$. This definition gives, for example, the three point $\mathrm{ECF}(3,\beta)$

$$\mathrm{ECF}(3,\beta) = \sum_{i<j<k\in J} p_{\mathrm{T}i} p_{\mathrm{T}j} p_{\mathrm{T}k} (R_{ij} R_{ik} R_{jk})^{\beta} \tag{6.4}$$

From the definition, we see that a jet that has fewer than $N$ constituents, will give $\mathrm{ECF}(N, \beta) = 0$. More importantly, this means that if the jet has $N$ subjets, $\mathrm{ECF}(N+1, \beta)$ should be significantly smaller than $\mathrm{ECF}(N, \beta)$. Therefore, the ratio

$$r_N^\beta = \frac{\mathrm{ECF}(N+1, \beta)}{\mathrm{ECF}(N, \beta)} \tag{6.5}$$

forms a useful observable for determining if a system has $N$ subjets. Similarly, to the $N$-subjettiness variables, better discrimination power is obtained with ECF double ratios as, for example,

$$C_N^\beta = \frac{r_N^\beta}{r_{N-1}^\beta} = \frac{\mathrm{ECF}(N+1, \beta)\mathrm{ECF}(N-1, \beta)}{\mathrm{ECF}(N, \beta)^2} \tag{6.6}$$

Like the $N$-subjettiness variables, the energy correlation functions are infrared and collinear safe for all $\beta > 0$. ATLAS studies have found that ECF ratios like $C_2^\beta$ are the best performing variables for $W$ boson tagging [82]. With $\beta < 1.0$ the correlators are even able to probe small-scale collinear splittings, making $C_1^{\beta=0.2}$ a useful observable for quark/gluon discrimination.

### 6.1.2 Multiplicity-like variables

The ECF ratios with $\beta < 1.0$ exemplify that the radiation pattern inside the jet can tell more than how many prongs it contains. It also allows us to discriminate between different types of one-prong jets, in particular quark- and gluon initiated jets. For this purpose, simpler observables than the $C_1^\beta$ can, however, be constructed.

The difference between quark and gluon jets arises from the showering phase. Gluons carry both colour and anti-colour while quarks only carry a single colour charge, meaning that gluon radiation off a gluon happens more frequently than gluon radiation off a quark. Therefore, the gluons on average undergo more splittings than the quarks. As a result gluon jets tend to be wider and have more constituents. The following two substructure variables are based on these properties.

*Track multiplicity*
The number of tracks associated with the jet functions as a proxy for the number of constituent particles, and is the most powerful single feature for quark/gluon tagging [83].

The track multiplicity $n_{\text{trk}}$ is computed using the ghost association method [71], which was previously explained in the context of pile-up subtraction, see Section 5.1.

Unlike the observable $C_1^\beta$ which is infrared and collinear safe, $n_{\text{trk}}$ does increase in value by additional soft and collinear radiations. This makes simulations of $n_{\text{trk}}$ more sensitive to the modeling of the shower phase, which is computed non-perturbatively. The modeling uncertainty on $n_{\text{trk}}$ used for quark/gluon tagging, is derived from data.

*Jet width*
The $p_{\text{T}}$ weighted width of the jet has also been shown to be an effective variable for discriminating between quarks and gluons. The commonly used definition in ATLAS, is based on the jet constituents, but could equally well be computed from the associated tracks:

$$w = \sum_{i \in J} \frac{p_{\text{T}i}}{p_{\text{T}J}} \Delta R_{iJ} \tag{6.7}$$

Here the sum runs over the constituents $i$ of the reconstructed jet $J$, where $p_{\text{T}i}$ is the transverse momentum of the constituent and $p_{\text{T}J}$, the transverse momentum of the jet. Again, $\Delta R_{iJ}$ is the Euclidian distance in rapidity-azimuth between the jet axis and the constituent.

An advantage of using the jet width over track multiplicity, is that the width is an infrared and collinear safe observable, allowing for an analytical description.

## 6.2 *b*-jet tagging

The ability to identify jets that contain *b*-hadrons (*b*-jets) from light quark or gluon jets, is crucial for many Standard Model measurements, studies of the Higgs boson properties, and searches for new physics phenomena.

Several algorithms of varying complexity are used for *b*-tagging in ATLAS. They rely on either one or more of the unique properties of *b*-hadrons; the long life time, the high mass, and the large decay multiplicity. Details about the strategy and performance of *b*-tagging in ATLAS, can be found in [84].

The most important feature of *b*-hadrons is the life time of approximately $\langle c\tau \rangle = 450\,\mu\text{m}$, giving a mean decay length of the order of millimeters at the typical energies with which a $b$-quark is produced at the LHC. This means that the *b*-hadron often decays at a measurable distance from the primary vertex, creating a secondary vertex, displaced from the interaction point.

The principle of $b$-tagging is illustrated in Figure 6.2, where the $b$-jet contains a secondary which is not present in the two light jets. The sketch also illustrates the impact parameter $d_0$ of one of the tracks associated with the $b$-jet. The impact parameter is defined at the point of closest approach of the trajectory to the $z$-axis. A large value of $d_0$ indicates the presence of a displaced vertex.

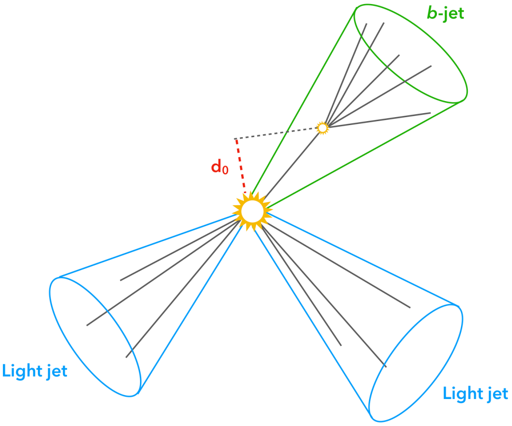

**Figure 6.2:** Sketch highlighting the difference between $b$-jets (green) and light quark jets (blue). In the $b$-jet a displaced, secondary vertex can be seen. The impact parameter $d_0$ of one of the track, associated to the $b$-jet, is also illustrated.

Two high-level multivariate $b$-tagging algorithms are centrally derived by the ATLAS collaboration for the use of ATLAS data analyses. They rely on various low-level algorithms which initially reconstruct the $b$-jet characteristics described above; the impact parameters of individual tracks and the displaced vertex. The two high-level algorithms then combine the results of the low-level algorithms to maximise the tagging performance. One of the high-level algorithms, MV2, is based on a boosted decision tree (BDT), and the other one, DL1, an artificial neural network.

The performance of the $b$-tagging algorithms are evaluated using *working points* of single cuts on the discriminant variables. Based on a set of fixed $b$-jet efficiencies in a simulated $t\bar{t}$ sample, the rejection factor of the corresponding selection requirement is computed. The working points of the MV2 algorithm, which is used for one of the searches in this thesis, are shown in Table 6.1.

**Table 6.1:** Selection criteria and rejection factors for $c$-, $\tau$, and light-flavour jets, corresponding to the $b$-tagging efficiency working points of the MV2 algorithm.

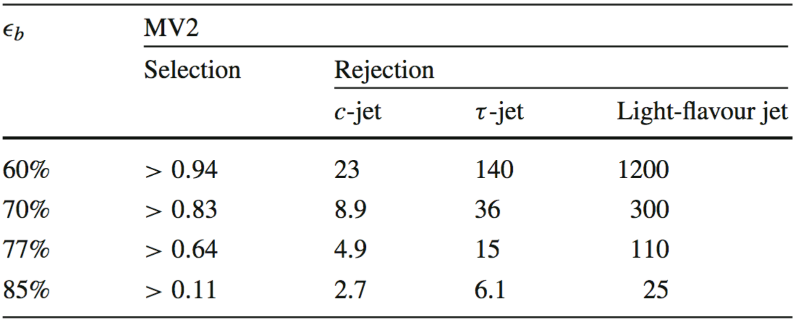

| $\epsilon_b$ | MV2 | | | |
|---|---|---|---|---|
| | Selection | Rejection | | |
| | | $c$-jet | $\tau$-jet | Light-flavour jet |
| 60% | $> 0.94$ | 23 | 140 | 1200 |
| 70% | $> 0.83$ | 8.9 | 36 | 300 |
| 77% | $> 0.64$ | 4.9 | 15 | 110 |
| 85% | $> 0.11$ | 2.7 | 6.1 | 25 |

# Part III

# Searches for New Physics in Hadronic Final States

With various jet types now reconstructed and calibrated, it is time to make use of these objects with physics analyses. Luckily jets appear in the final state of many interesting processes, both known and hypothesized.

In particle physics, we search for the hypothesized processes by looking for a deviation from the expected background of known physics processes. To do this, a good understanding of the expected background is the first and foremost requirement. We also usually need one or more ideas of what kind of new phenomena to look for, in order to establish a good analysis strategy. If no deviation is found, we can use the result to make statements about what possible phenomena we can exclude the existence of and with what certainty.

In this chapter I summarise two searches for new physics phenomena conducted using ATLAS data with either four small- or two large-radius jets. The two searches target rather different BSM scenarios and yet, they have a lot in common, as we will see.

## Chapter 7

# Pair-production of *R*-parity Violating Stop Squarks

Paired dijet resonances are expected as signatures of many Standard Model extensions. For example supersymmetry (SUSY) with *R*-parity violating (RPV) couplings, which allow the lightest supersymmetric particle to decay to two jets. The concept of supersymmetry and the properties of RPV SUSY models in particular were discussed in Section 2.4.3. While *R*-parity conserving SUSY models have long been preferred, RPV couplings have not been ruled out experimentally and could easily escape discovery if not searched for explicitly.

Based on naturalness arguments, the supersymmetric partners of the Higgs boson and top quark, the higgsino and the stop squark, are expected to have masses below 1 TeV. Thorough search programs for stop squarks at the LHC have excluded these below 1 TeV in *R*-parity conserving scenarios. However, allowing RPV couplings significantly relaxes the existing bounds on the stop squark mass. This chapter presents an analysis which searches for pair-produced massive, coloured particles decaying to two jets [85]. The results are interpreted in a SUSY simplified model where the stop squark is the lightest supersymmetric particle. In the targeted scenario, the stop squark decays through baryon-number-violating RPV couplings $\lambda''$ to two quarks, where the dominant coupling is expected to be large enough for the decay to be prompt. Two examples of this process are sketched in Figure 7.1.

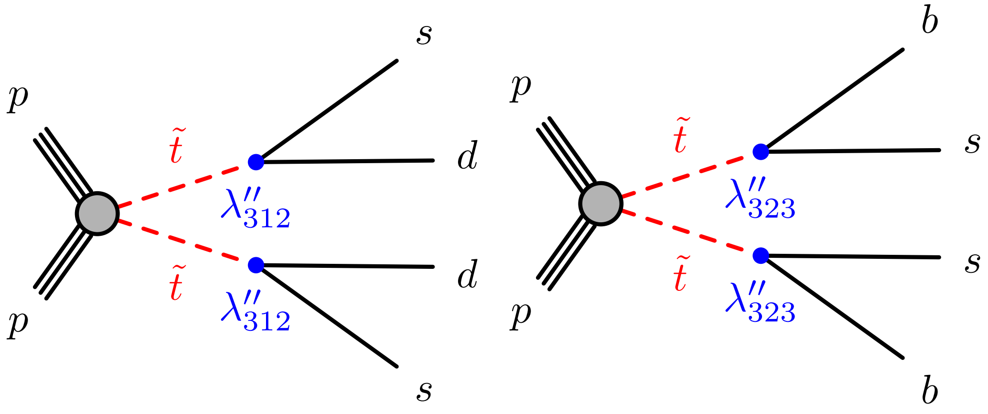

**(a)** $\tilde{t}\tilde{t} \rightarrow (\bar{d}\bar{s})(ds)$ **(b)** $\tilde{t}\tilde{t} \rightarrow (\bar{b}\bar{s})(bs)$

**Figure 7.1:** Diagrams depicting possible decays of the stop squark through the *R*-parity violating couplings $\lambda''$ indicated by blue dots. On the left (a) the stop squark decays to a down ($d$) and a strange ($s$) quark. On right (b) the stop decays to a bottom ($b$) and a strange quark [85].

In scenarios where the dominant RPV couplings involve third-generation quarks ($\lambda''_{3i3}$), a $b$-quark is expected from each of the stop decays. These are considered separately from the inclusive scenarios ($\lambda''_{3ii}$), as discussed in the following section. In the absence of a discovery, limits are derived on the possible cross sections for both categories of stop squark processes.

Additional limits are set on pair-produced massive colour-octet resonances, commonly referred to as colorons $\rho$. Colorons are predicted by a range of theories including axigluons and Kaluza-Klein excitations of gluons. They also arise as scalar partners of the SM gluino in models with extended SUSY. These scalar gluino (sgluinos) are mostly produced in pairs and can decay to either two quarks or two gluinos.

## 7.1 Analysis strategy

As mentioned in Section 3.1.3, we generally expect known phenomena to occur much more frequently than the new physics phenomena we search for. We often refer to the physics phenomena of interest as “signals” and the known processes which can mimic the signal processes of interest, as “backgrounds”. To see a statistically significant effect of a signal process, the backgrounds must be suppressed, or precisely estimated.

This analysis targets signals which lead to fully hadronic, four-jet final states with little or no missing transverse momentum. These signatures pose a challenge due to the huge background of Standard Model multijet processes. Differences in the typical topology of signal and background events are exploited to select events which are most likely to be signal and reduce the background contributions. These selections are described in Section 7.5.

In all the considered signal processes, the four leading jets originate from two equal-mass resonances. If the jets are correctly paired, a resonance with mass close to the true stop squark or coloron mass can be reconstructed from each pair. The spectrum of average mass $m_{\text{avg}}$ of the two reconstructed resonances forms a peak around the true resonance mass, as can be seen in Figure 7.2.

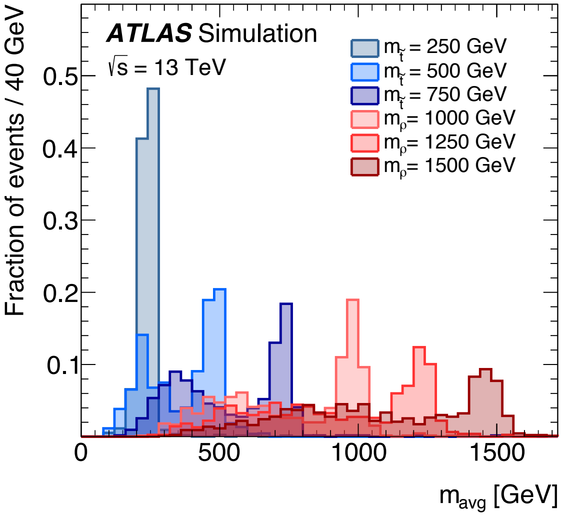

**Figure 7.2:** Distributions of the average mass of the two reconstructed resonances in signal events with a stop squark of mass $m_{\tilde{t}}$ =250, 500, and 750 GeV, or a coloron of mass $m_{\rho}$ =1000, 750, and 1500 GeV [85].

For Standard Model multijet events, the $m_{\text{avg}}$ spectrum falls off gradually without peak-like structures. Therefore, a local excess in the $m_{\text{avg}}$ spectrum is expected, if the fraction of signal events is sufficient in the data sample.

Selecting events with two $b$-jets significantly reduces the remaining multijet background. Thus, the sensitivity can be increased for the specific scenario where the stop squark decays to one $b$-quark and one lighter quark. Therefore, two event selections are defined to look for the $\lambda''_{3i3}$ and $\lambda''_{3ii}$ scenarios separately.

The search is carried out by counting the number of events in windows of $m_{\text{avg}}$ and comparing to the background-only hypothesis. The window sizes are optimised for to maximise the signal significance in simulation, and ranges from 10 GeV for a 100 GeV stop squark to a width 200 GeV for a 1500 GeV coloron. The mass window for the highest target mass considered, has no upper edge. When the mass difference between two signal samples is smaller than the experimental resolution, their selected mass windows partially overlap.

## 7.2 Data and preselections

Analysing the entire ATLAS data set is unfeasable in terms of computing and unnecessary since not all events are interesting for all analyses. Instead, the data set is initially reduced to the most relevant events by imposing requirements on the triggers, quality, and event topology. This reduction is called the baseline preselection, since it is imposed on data and MC simulations prior to optimising the final event selection.

### 7.2.1 Data sample

The search is performed in a sample of $\sqrt{s} = 13\,\text{TeV}$ $p\bar{p}$ collision data, which was collected with the ATLAS experiment from 2015 to 2016. The events were recorded using a four-jet trigger, requiring all four jets to have $p_\text{T} > 100\,\text{GeV}$ at the second level of the ATLAS trigger, Section 3.2.7. The baseline event selection, called the "preselection" and described in the following, ensures that this trigger is fully efficient. Events are also required to be recorded during stable beam conditions, and come from luminosity blocks where all detector sub-systems were operating above the 90%-level [86]. With the quality criteria and event selection combined, the final data samle corresponds to $36.7\,\text{fb}^{-1}$.

### 7.2.2 Preselections

Events are required to have at least two tracks with $p_\text{T} > 400\,\text{MeV}$ pointing back to the primary vertex. The primary vertex is determined as the one with the largest sum of $p_\text{T}$ when summing over all tracks that have $p_\text{T} > 0.5\,\text{GeV}$ and are associated with the vertex.

Jets can be reconstructed from calorimeter signals that come from non-collision sources including calorimeter noise, the beam halo and cosmic rays. These can be an important background at high-$p_\text{T}$, and so criteria were developed using early 2015 data to reject such jets based on timing and jet shape [87]. Events that contain at least on jet with $p_\text{T} > 20\,\text{GeV}$ that is classified as *tight-bad* according to the criteria in [87] are rejected.

To ensure that the trigger is fully efficient, events are only kept if they have four jets of $p_\text{T} > 120\,\text{GeV}$ and $|\eta| < 2.4$.

## 7.3 Simulated samples

As we have already seen in the discussion of jet calibration, Chapter 5, data simulations are crucial to obtain a thorough understanding of how the detector responds to the particles we measure. Simulations are also used at the stage of physics analyses to understand how the expected background distributions behave, and how signal events can be distinguished. Furthermore, simulations can be important for understanding the impact of systematic uncertainties in the analysis.

For this analysis, the dominant multijet background is estimated by a data-driven technique, but simulations are used to estimate the background from top-pair ($t\bar{t}$) events, to make predictions based on signal models, and to validate the data-driven background estimation.

The simulated data samples used for this analysis reflect the data taking conditions of the years 2015-2016. The minimum-bias samples, used to immitate pile-up as described in Section 2.3, were produced with Pythia using the MSTW2008LO parton distribution function (PDF) [21], and the MC generator tune A2 [88].

### 7.3.1 Signal simulation

The two different kinds of signal samples were produced using a generator called MadGraph interfaced to Pythia 8. The generation is done with the NNPDF23LO PDF [21] and the modeling of the parton shower, hadronisation and underlying event uses the A14 tune [88]. The matrix elements are calculated at leading order.

For the stop squark signal generation, the branching ratio of stop squarks into a bottom and a strange quark is set to 100%. Except for the mass of the stop squark, all non-SM particle masses are set to 5 TeV. This same sample is used for interpreting the results in terms of the scenario where the stop squarks decays to light quarks and the scenario where there is a *b*-quark from each stop squark decay, since the analysis is not sensitive to the flavour content of the jets. The cross sections for stop squark pair-production were calculated at next-to-leading order (NLO) in the strong coupling constant.

The coloron sample generation was based on a model where the couplings of the vector colour octet to all particles except light quarks were set to zero [89]. The LO cross sections from the event generator were used. The coloron samples are also used to interpret the result in the context of sgluon pair-production, where they are scaled to the sgluon cross section computed at NLO with MadGraph. The sgluons are assumed to decay into two gluons, which in this analysis are not distinguished from quark-initiated jets.

### 7.3.2 Background simulation

The backgrounds from multijet and $t\bar{t}$ events are simulated seperately. Samples of multijet processes were simulated with $2 \to 2$ matrix elements at leading order (LO) using the Pythia 8 event generator. The samples were produced with the ATLAS A14 tune [90] together with the NNPDF23LO PDF.

The production of $t\bar{t}$ events were generated with the Powheg-Box V2 [29] using the CT10 PDF set and setting the top mass to 172.5 GeV. The parton shower, hadronisation, and the underlying event processes were simulated with Pythia 6, using the CTEQ6L1 PDF and the corresponding Perugia tune [91]. The events were weighted based on the $t\bar{t}$ production cross section, as calculated at next-to-next-to leading order (NNLO).

## 7.4 Event reconstruction

The signal models considered in this analysis give fully hadronic final states which are reconstructed as jets. The jet reconstruction follows the description given in Chapter 4 for EM small-$R$ jets: The jets are built from calorimeter topoclusters which are calibrated to the electromagnetic scale. The anti-$k_t$ algorithm with a radius parameter of $R = 0.4$ is used for the jet finding. The reconstructed jets are then calibrated according to the scheme presented for small-$R$ jets in Chapter 5.

To identify jets that are likely to contain a $b$-hadron, the multivariate $b$-tagging algorithm, MV2, is used [92]. As described in Section 6.2, the MV2 algorithms combines information from the inner detector about the impact parameter of the tracks associated with the jet, and the presence of displaced secondary vertices in a BDT. The chosen working point gives a $b$-jet selection efficiency of 77% and a corresponding rejection factor against light jets of 110. The efficiencies of the tagger is determined using simulated $t\bar{t}$ events [84].

## 7.5 Signal regions

Following the preselection, additional selection criteria are applied to reduce the background contribution of the final event selections. Combinations of these selections categorise the data in two *signal regions* (SR). The signal regions are used in order to ensure the best sensitivity to all the considered signal scenarios; one flavour inclusive SR and one $b$-tagged SR. It is with these two data sample that the search is actually performed. Three of the selection criteria apply to both signal regions, where the fourth defines the $b$-tagged region. The criteria are based on variables which have been found to have discriminating power by previous ATLAS searches [93] [94].

The analysis targets final states consisting of two pairs of jets, where each pair originates from one of two equal-mass resonances. If the resonances are produced with a significant boost, the decay products are expected to be collimated. Therefore, the two dijet pairs are defined by minimising the sum of the distances between the two jets in each pair:

$$\Delta R_{\text{min}} = \min \left( \sum_{i} = 1, 2 |\Delta R_i - 1| \right) \tag{7.1}$$

Here $\Delta R_i$ is the angular distance between the two jets of the pair $i$. The summation is over the two dijet pairs, which consist of the four highest $p_{\text{T}}$ jets in the event. The offset of $-1$ increases the difference between the $\Delta R_{\text{min}}$ of expected signal event topologies and $\Delta R_{\text{min}}$ of SM multijet events, where the four leading jets do not necessarily appear in two collimated pairs. This difference means that the pairing metric can also be used as a discriminating variable to reduce the multijet background. The distribution of $\Delta R_{\text{min}}$ can be seen for two different signal scenarios compared to data in Figure 7.4a.

Since resonances of higher mass are generally produced with a lower boost, the criterion on $\Delta R_{\text{min}}$ depends on the average reconstructed resonance mass,

$$m_{\text{avg}} = \frac{1}{2}(m_1 + m_2) \tag{7.2}$$

where $m_1$ and $m_2$ are given by the four-vector sum of the two jets in pair 1 and 2, respectively. Events are required to satify:

$$\begin{aligned} \Delta R_{\text{min}} &< -0.002 \cdot (m_{\text{avg}}/\text{GeV} - 225) + 0.72 \quad \text{if} \quad m_{\text{avg}} \leq 225\,\text{GeV} \\ \Delta R_{\text{min}} &< +0.0013 \cdot (m_{\text{avg}}/\text{GeV} - 225) + 0.72 \quad \text{if} \quad m_{\text{avg}} \geq 225\,\text{GeV} \end{aligned} \tag{7.3}$$

The second selection criterion exploits the fact that SM multijet production usually happens through $t-$channel processes, resulting in more jets in the forward detector region. The signal processes, on the other hand, are more likely to produce jets in the central detector region. This feature is quantified by the magnitude of the cosine of the angle between resonance and the beamline $|\cos\theta^*|$, where the angle $\theta^*$ is defined in center-of-mass reference frame of the two resonances. Thus, the values of $|\cos\theta^*|$ are expected to be closer to 1 for background events and closer to 0 for signal events, as can be seen in Figure 7.4b. A requirement of $|\cos\theta * | < 0.3$ on both reconstructed resonances is imposed.

The third selection criterion relies on the fact that the two resonances have equal masses in the signal scenarios. The asymmetry between masses of the reconstructed resonances is therefore expected to be smaller for signal than for background processes. The mass asymmetry is defined as

$$\mathcal{A} = \frac{m_1 - m_2}{m_1 + m_2} \tag{7.4}$$

and is required to satisfy $\mathcal{A} < 0.05$. The distribution of $\mathcal{A}$ for data and two signal scenarios is shown in Figure 7.3c.

Finally, the $b$-tagged signal region is defined by requiring the even to have exactly one $b$-tagged jet associated with each of the two candidate resonances. Distributions of number of $b$-tagged jets is found in Figure 7.3d for data as well stop squark signal events with masses $m_{\tilde{t}} = 250$ GeV and $m_{\tilde{t}} = 500$ GeV.

As described in Section 7.1, the search performs a counting experiment in windows of $m_{\text{avg}}$, where the window width is optimised for each signal hypothesis. The signal acceptance times selection efficiency is shown as a function of the resonance mass $m$, with and without the mass window selection in Figure 7.4. The acceptance of the signal region selection is lowest for small masses, where the resonances are likely to be so boosted, that the decay products form to large-radius jets. The acceptance increases with masses as the four jets can be resolved and the jet $p_{\text{T}}$ becomes larger. However, for the highest resonance masses, the jets from each decay are more back-to-back, so the $\Delta R_{\text{min}}$ pairing does not always correctly combine the jets into resonance candidates. The high-mass signal samples have a tail extending to low $m_{\text{avg}}$ values, which degrades the efficiency of the mass window selection.

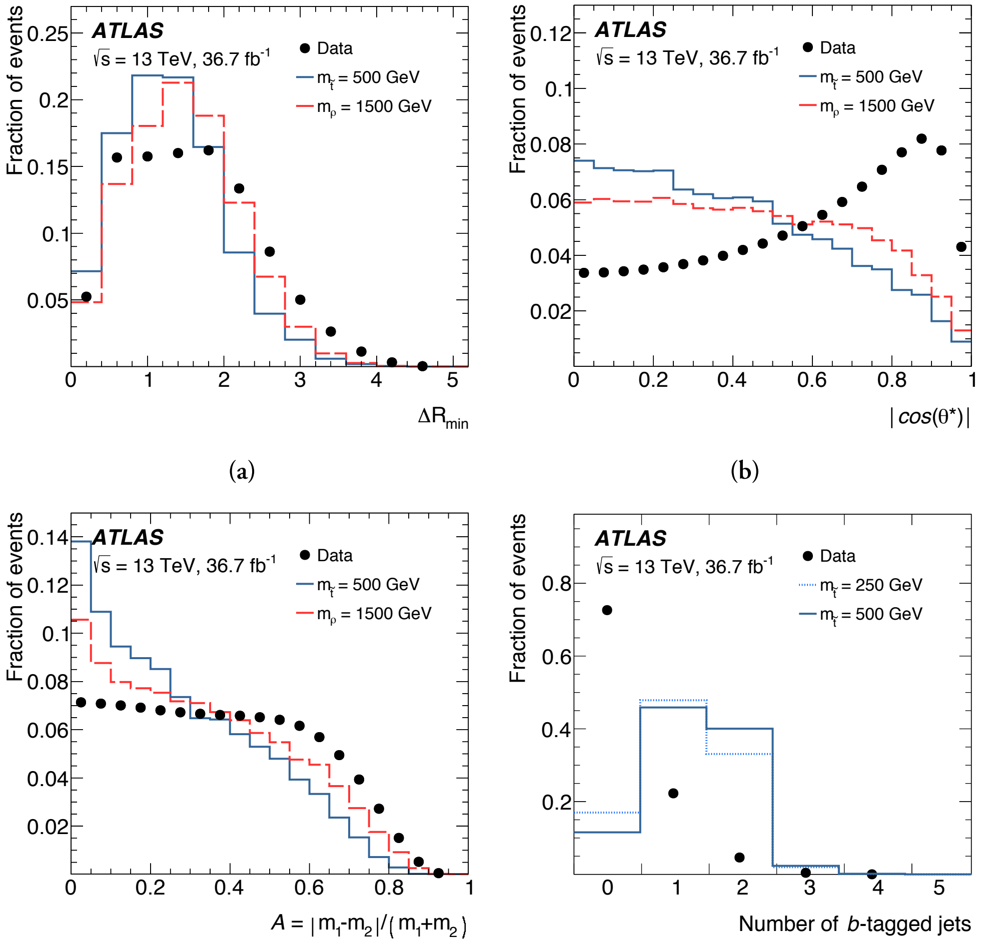

(a) (b)

(c) (d)

**Figure 7.3:** Distribution of the four discriminating variables, used to define the signal regions. The distributions of minimum sum of angular distance between two jets in a pair $\Delta R_{\text{min}}$ (a), the angle between resonance and beamline $|\cos\theta*$ (c), and the mass asymmetry $A$ (c), are all shown for data, a stop squark of mass $m_{\tilde{t}} = 500\,\text{GeV}$, and a coloron of mass $m_{\rho} = 1500\,\text{GeV}$. The number of $b$-tagged jets in an event is shown for data and stop squark masses of $m_{\tilde{t}} = 250$ and $500\,\text{GeV}$ [85].

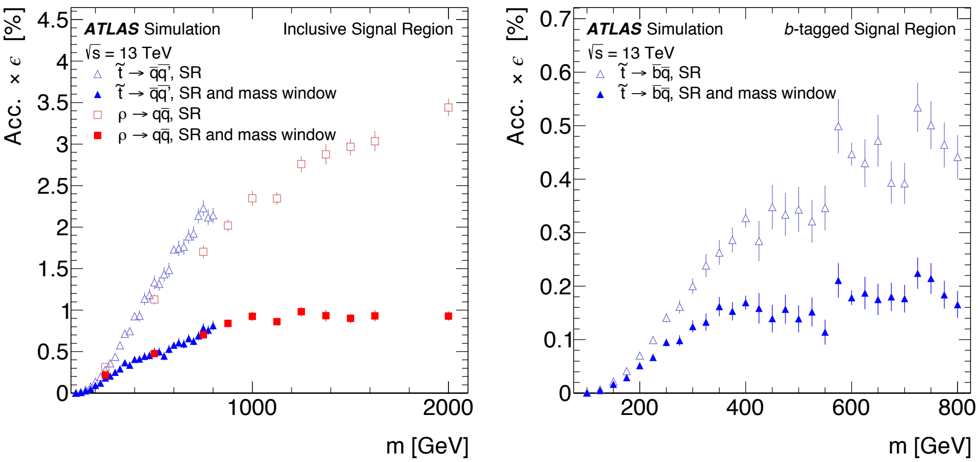

(a) (b)

**Figure 7.4:** The acceptance times efficiency of various signal samples as a function of the resonance mass $m$ for the inclusive Signal Region (a) and the $b$-tagged Signal Region (b). Top squark signals are displayed in blue triangles and colorons by red squares. Open symbols indicate that the efficiency is computed before the mass window selection is applied, and full symbols, after [85].

## 7.6 Background estimation

The event selection described above reduces the background from SM multijet processes by two orders of magnitude, yet this is still the dominant background in both signal regions. The contribution to the signal regions from multijet background events is estimated from data with a method that predicts both the normalisation and shape of the $m_{\text{avg}}$ distribution. In the $b$-tagged region, the multijet background is much smaller, so contributions from top-pair production events become significant. This $t\bar{t}$ background is estimated from simulations.

The data-driven backgroud estimation, called the "ABCD method", divides the data of each $m_{\text{avg}}$ bin into six regions based on the variables $\mathcal{A}$ and $|\cos\theta*|$, as illustrated in Figure 8.18. One is the signal region (D), where we expect the largest signal significance. Four are background-dominated control regions (A,B,C, F), expected to include a negligable amount of signal events. The last is a validation region (E) which is used to test the method and assign an uncertianty to the estimate.

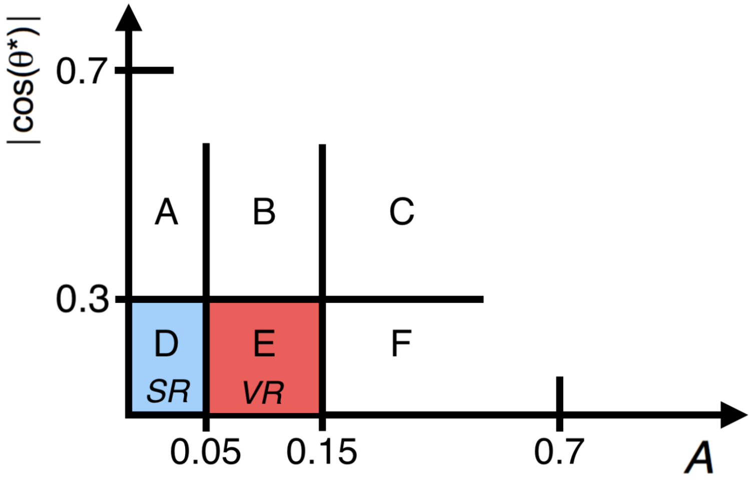

**Figure 7.5:** Overview of the signal, control, and validation regions in the $(\mathcal{A}, |\cos\theta*|)$ plane. The control region (CR) and validation region (VR) are used for the data driven background estimation [85].

Under the assumption that the two variables, $\mathcal{A}$ and $|\cos\theta^*|$, are uncorrelated, and the signal contamination in the control regions is negligible, then the amount of background in the signal region is given by $N_D = N_A \times N_F/N_C$. Likewise, the amount of background in the validation region, can be predicted as $N_E = N_B \times N_F/N_C$. The correlation is measured to be around 2% in data and simulation, except at larger values of $\mathcal{A}$. Therefore the control regions are restricted to the region $\mathcal{A} < 0.7$ and $|\cos\theta^*| < 0.7$.

For the inclusive selection, signal leakage to the control regions can be neglected, and the background estimation follows the method sketched above. Background contributions from $t\bar{t}$ events amount to less than 1% of the total background for $m_{\text{avg}} < 200\,\text{GeV}$, and are also accounted for by the data-driven method. Beyond $m_{\text{avg}} = 200\,\text{GeV}$, the $t\bar{t}$ background is negligible.

For the $b$-tagged selection, the background is relatively small, so signal contamination in region A could be significant enough to bias the background estimate in the signal region D. Therefore, the estimation is done in several steps. First, the multijet background is estimated in a data with zero $b$-tagged jets, following the same procedure as for the inclusive selection. The prediction from the signal region in the $b$-veto selection is then projected to the signal region with two $b$-tagged jets. The projection factors are deined as the ratio between the number of events in the two $b$-tagged and the zero $b$-tagged regions, $N_{2-b}/N_{0-b}$. They are computed for each bin of the $m_{\text{avg}}$ distribution in region F, where the signal contamination is negligible, and assumed to be constant in the $(\mathcal{A}, |\cos\theta^*|)$ plane.

The multijet and $t\bar{t}$ productions scale differently between the two $b$-tagged and zero $b$-tagged selections. Therefore, the $t\bar{t}$ contribution is not correctly accounted for by the data-driven method in the $b$-tagged signal region. Instead, simulated samples are used to directly predict the $t\bar{t}$ background, and to subtract the $t\bar{t}$ contribution from the data-driven estimate.

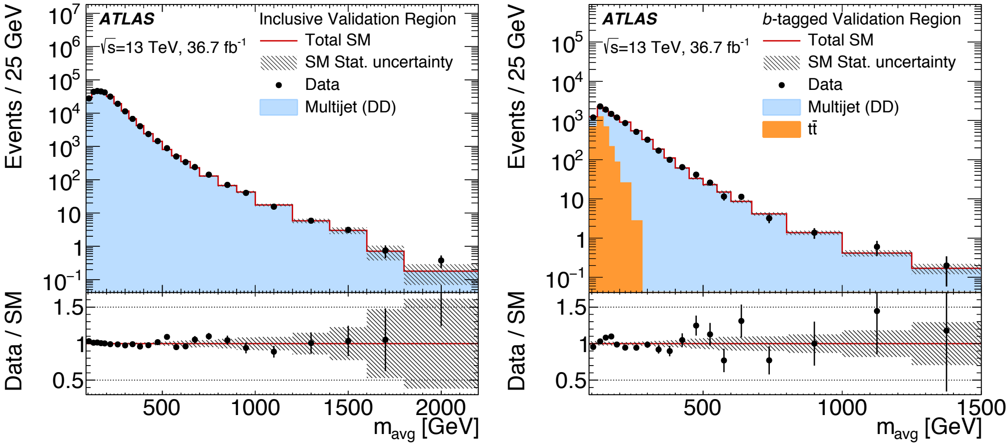

(a)

(b)

**Figure 7.6:** Distribution of the average resonance mass $m_{\text{avg}}$ as measured in the inclusive validation region (a) and the $b$-tagged validation region. The data (black points) is compared to the total estimated background (red line), of which the fraction coming from the data-driven multijet prediction is shown in blue and the fraction coming from top pair production is shown in orange. The lower panel shows the ratio between the data and the total expected background, where the hashed area illustrates the uncertianty on the ratio [85].

The background estimation method is tested in the validation region by comparing the predicted $m_{\text{avg}}$ spectrum to data. The predicted and observed spectrum are found to generally agree within the statistical uncertainties for both the inclusive and the $b$-tagged selections, as can be seen in Figure 7.6.

## 7.7 Systematic uncertainties

Whether an excess of events appears in the signal region or not, understanding our (un)certainty of the background estimation and expected signal distributions, is essential to make any conclusions. If a local deviation from the expected background is seen, the uncertainties are necessary to estimate how significant that deviation is. If the data is consistent with the background estimate, we must know the uncertainties to say with what confidence we can exclude the possibility of a given signal. This section describes the various uncertainties which might affect the signal and background predictions, and how they are evaluated.

### 7.7.1 Multijet background uncertainties

The systematic uncertainty on the multijet background estimate comes mainly from the ABCD method itself. The uncertainty is derived from the bin-by-bin difference between the background prediction and the observed data in the validation region, which was shown in Figure 7.6. To reduce the effect of statistical fluctuations, the relative difference is smoothed using kernel regression. The smoothed difference between the predicted distribution and the data spectrum (the "non-closure") is computed for each window in $m_{\text{avg}}$ and assigned as a systematic uncertainty on the multijet background.

To further validate the multijet background estimation and uncertainty, the compatibility to an alternative method is checked. The data in the validation region is fitted with a four parameter function

$$f(x, p_i) = p_0 \cdot \frac{(1-x)^{p_1}}{x^{p_2+p_3\cdot\log(x)}}, \quad x = \frac{m_{\text{avg}}}{\sqrt{s}} \tag{7.5}$$

and the bin-by-bin difference between the fit and the background prediction is taken as the uncertainty. The fit to data in the validation region is compared the data-driven (DD) multijet prediction for the inclusive and the $b$-tagged selection in Figure 7.7.

The fit extends down to 300 GeV, below which the fit quality deteriorates. The fit is repeated with two different $m_{\text{avg}}$ binnings, 10 GeV and 25 GeV, and the relative difference between the two results is taken as the fit uncertainty. The fit method and the ABCD method are found to give compatible descriptions and uncertainties of the multijet background in the validation regions over the $m_{\text{avg}}$ range where they both apply.

### 7.7.2 Top-pair background uncertainties

The uncertainty on the estimated $t\bar{t}$ background comes partially from detector-related effects. These include the uncertainty on the jet energy scale and resolution, as well as the $b$-tagging efficiency and mis-tagging rate.

Additional systematic uncertainties come from MC simulation of $t\bar{t}$ processes, used to estimate the background of the $b$-tagged signal region. The systematic uncertainty related the choice of generator is evaluated by comparing the nominal sample to samples obtained

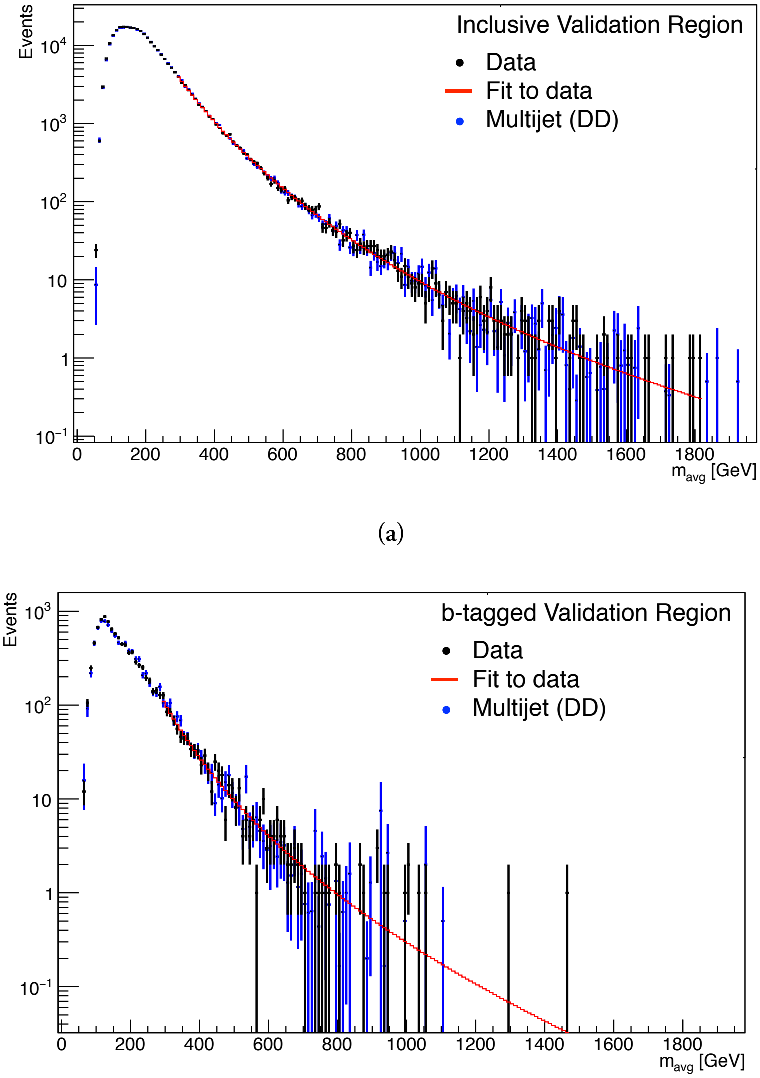

(a)

Â

(b)

**Figure 7.7:** Functional fit (red line) to the $m_{\text{avg}}$ spectrum as measured in the inclusive validation region (a) and the $b$-tagged validation region (b). The fit is shown along with the data (black points) and the data-driven (DD) multijet background prediction (blue points). The vertical lines represent the statistical uncertainties.

with different generators. Systematic uncertainties related to the showering are evaluated by modifying the shower parameters and comparing those predictions to the nominal sample.

A summary of the magnitude of backround uncertainties is shown in Figure 7.8.

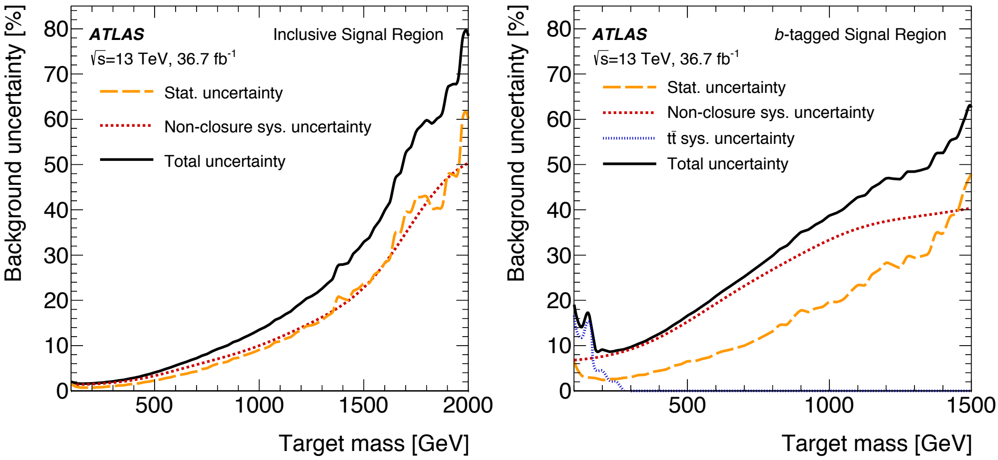

(a) (b)

**Figure 7.8:** Estimated uncertainties on the background prediction in the inclusive signal region (a) and the $b$-tagged signal region (b). The statisstical uncertainty is shown as an orange, dashed line, and the uncertainty arising from the non-closure in the validation region is shown with a dotted red line. The systematic uncertainty on the simulated top sample is shown with a blue dotted line, and is only relevant in the $b$-tagged signal region. The solid, black line shows the total sum of all uncertainties [85].

### 7.7.3 Signal uncertainties

The detector-related systematic effects from the jet energy scale and resolution also affect the signal yield by about 10% in the inclusive SR and 15% in the $b$-tagged SR. The theoretical uncertianties on the cross-section of stop squark production is derived from an envelope of cross-sections computed with multiple PDFs and varying factorisation and renormalisation scales. The theoretical uncertainty on the signal acceptance, is also evaluated by varying the factorisation and renormalisation scales, as well as the strong coupling constant in the generation and the parameters governing the parton shower and hadronisation in PYTHIA 8.

## 7.8 Results

The spectrum of $m_{\text{avg}}$, measured in the inclusive and $b$-tagged signal regions, is shown in Figure 7.9. The data is compared to the predicted background distribution and various signal scenarios. Agreement between data and expected background is observed across the spectrum.

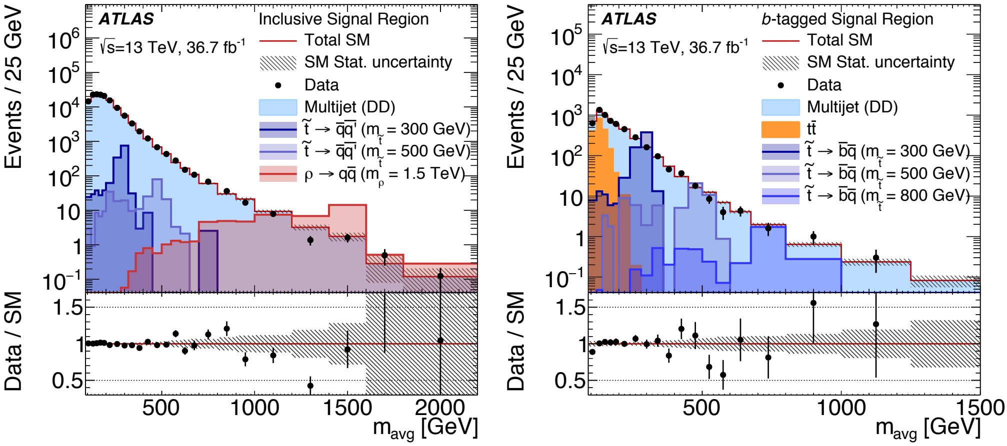

(a)

(b)

**Figure 7.9:** Distribution of the $m_{\text{avg}}$ spectrum measured in the inclusive signal region(a) and the $b$-tagged signal region (b). The data (black points) is shown along the total estimated background (red line). The estimated contribution to the total background from multijet processes is shown as the blue region and the contribution from top pair production in orange. The expected distribution from stop squark or coloron production is overlaid. The lower panel shows the ratio between the data and the total expected background, where the hashed area illustrates the uncertainty on the ratio [85].

The compatibility of the data with a stop squark or coloron signal is tested in windows of $m_{\text{avg}}$, optimised for the various signal hypotheses. Comparisons between the observed number of events, the expected number of background events, and the expected number of signal events is shown for each mass window for the inclusive signal region in Tables 7.1 7.2, and for the $b$-tagged signal region in 7.3.

The compatibility between data and a generic massive resonance, is also tested by scanning the observed $m_{\text{avg}}$ spectrum in bins of $12.5\,\text{GeV}$. The largest deviation is found in the $b$-tagged region for a mass of $463\,\text{GeV}$, corresponding to a local $p$-value of $0.05$.

Since no statistically significant excesses are observed in data compared to the expected background, the results can be used to exclude certain signal hypotheses. Limits on the possible production cross sections of stop squarks, sgluons, and colorons decaying to a pair of jets, are derived from the $m_{\text{avg}}$ spectrum in the inclusive signal region. The $b$-tagged region is used to set limits on the production of stop squarks specifically decaying to a $b$-quark and a lighter quark. A profile likelihood ratio of Poisson probabilities for signal and

**Table 7.1:** Observed numbers of events in the data $N_{\mathrm{Data}}$ the estimated numbers of background events $N_{\mathrm{Bkg}}$ and the expected numbers of stop squark signal events $N_{\mathrm{Sig}}$ in the stop squark mass windows of the inclusive signal region. Statistical and systematic uncertainties are given separately.

| $m_{\tilde{t}}$ [GeV] | Window [GeV] | $N_{\mathrm{Data}}$ | $N_{\mathrm{Bkg}}$ (± stat. ± syst.) | $N_{\mathrm{Sig}}$ (± stat. ± syst.) |
|---:|:---:|---:|---:|---:|
| 100 | [100, 110] | 5899 | 5910± 90± 70 | 519 ±23 ± 68 |
| 125 | [120, 135] | 13 497 | 13 450±120± 180 | 1890 ±50 ± 190 |
| 150 | [140, 160] | 18 609 | 18 390±130± 250 | 2540 ±50 ± 130 |
| 175 | [165, 185] | 17 742 | 17 800±130± 250 | 2280 ±50 ± 210 |
| 200 | [185, 210] | 19 844 | 19 660±140± 290 | 2250 ±50 ± 170 |
| 225 | [210, 235] | 14 898 | 15 180±120± 230 | 1620 ±40 ± 100 |
| 250 | [230, 260] | 13 689 | 13 750±110± 220 | 1440 ±80 ± 140 |
| 275 | [255, 285] | 9808 | 9860±100± 170 | 1010 ±70 ± 80 |
| 300 | [275, 310] | 8514 | 8790± 90± 160 | 789 ±52 ± 31 |
| 325 | [300, 335] | 6180 | 6330± 80± 120 | 600 ±50 ± 50 |
| 350 | [320, 365] | 5802 | 5900± 70± 120 | 509 ±39 ± 19 |
| 375 | [345, 390] | 4113 | 4250± 60± 90 | 324 ±25 ± 31 |
| 400 | [365, 415] | 3531 | 3590± 60± 90 | 274 ±14 ± 18 |
| 425 | [385, 440] | 3108 | 3010± 50± 80 | 198 ±23 ± 10 |
| 450 | [410, 465] | 2281 | 2230± 40± 60 | 154 ±17 ± 27 |
| 475 | [430, 490] | 1906 | 1920± 40± 60 | 116 ±12 ± 8 |
| 500 | [455, 515] | 1495 | 1513± 35± 49 | 94 ±10 ± 8 |
| 525 | [475, 540] | 1318 | 1327± 33± 46 | 71 ± 7 ± 4 |
| 550 | [500, 565] | 1050 | 1048± 29± 39 | 48.5± 5.4± 2.2 |
| 575 | [520, 590] | 924 | 912± 27± 36 | 44 ± 4 ± 4 |
| 600 | [545, 620] | 745 | 744± 25± 31 | 36.9± 1.6± 2.3 |
| 625 | [565, 645] | 645 | 626± 22± 28 | 30.3± 2.8± 3.4 |
| 650 | [585, 670] | 536 | 554± 21± 26 | 23.3± 2.1± 1.9 |
| 675 | [610, 695] | 438 | 473± 19± 24 | 20.3± 1.6± 0.9 |
| 700 | [630, 720] | 404 | 422± 18± 22 | 15.4± 1.2± 0.9 |
| 725 | [655, 745] | 341 | 335± 16± 18 | 13.6± 1.0± 0.9 |
| 750 | [675, 770] | 306 | 310± 16± 18 | 12.4± 0.9± 0.9 |
| 775 | [700, 795] | 265 | 243± 14± 14 | 9.7± 0.7± 0.7 |
| 800 | [720, 820] | 238 | 205± 12± 13 | 8.5± 0.6± 0.6 |

background is computed to determine the 95% confidence level for compatibility of the data with the signal-plus-background hypothesis ($\mathrm{CL}_{\mathrm{s+b}}$). Similarly, the 95% confidence level for compatibility of the data with the background-only hypothesis ($\mathrm{CL}_{\mathrm{b}}$) is computed. From the ratio of these two quantities, the confidence level for the presence of a signal ($\mathrm{CL}_{\mathrm{s}}$)is determined. Systematic uncertainties are treated as nuisance parameters and are assumed to follow Gaussian distributions.

The observed and expected 95% CL upper limits on the allowed cross sections are shown in Figure 7.10. For stop squark decays into two quarks, the masses between 100 GeV and 410 GeV are excluded. This exclusion also applies to the pair-production of other squarks, decaying, for example, to a down- and an up-quark. If the stop squark decays into a *b*-quark and a lighter quark, masses ranging from 100 GeV to 470 GeV and from 480 GeV

**Table 7.2:** Observed numbers of events in the data $N_{\mathrm{Data}}$ the estimated numbers of background events $N_{\mathrm{Bkg}}$ and the expected numbers of coloron signal events $N_{\mathrm{Sig}}$ in the coloron mass windows of the inclusive signal region. Statistical and systematic uncertainties are given separately.

| $m_\rho$ [GeV] | Window [GeV] | $N_{\mathrm{Data}}$ | $N_{\mathrm{Bkg}}$ (± stat. ± syst.) | $N_{\mathrm{Sig}}$ (± stat. ± syst.) |
|---|---|---|---|---|
| 500 | [455, 515] | 1495 | 1513 ±35 ± 15 | 23 000 ±1900 ±1200 |
| 625 | [565, 645] | 645 | 626 ±22 ± 35 | 7050 ± 370 ± 350 |
| 750 | [675, 770] | 306 | 310 ±15 ± 30 | 2510 ± 170 ± 120 |
| 875 | [790, 900] | 166 | 144 ±10 ± 16 | 1020 ± 56 ± 23 |
| 1000 | [900, 1025] | 79 | 96 ± 9 ± 8 | 416 ± 25 ± 17 |
| 1125 | [1010, 1155] | 46 | 58 ± 7 ± 5 | 154 ± 8 ± 5 |
| 1250 | [1120, 1280] | 27 | 36 ± 5 ± 3 | 73 ± 4 ± 4 |
| 1375 | [1235, 1410] | 9 | 17 ± 3 ± 3 | 51.0± 2.0± 1.2 |
| 1500 | [1345, 1535] | 13 | 14 ± 3 ± 1.6 | 12.9± 0.8± 0.4 |
| 1625 | [1455, 1665] | 7 | 8.7± 2.6± 0.6 | 12.9± 0.8± 0.4 |
| 1750 | [1565, 1790] | 6 | 4.8± 2.0± 2.6 | 2.8± 0.1± 0.1 |
| 1875 | [1680, 1920] | 4 | 5.3± 2.2± 3.5 | 1.3± 0.1± 0.1 |
| 2000 | [1790, ∞] | 2 | 2.1± 1.2± 0.4 | 0.6± 0.1± 0.1 |

to 610 GeV.

As seen in Figure 7.4, the signal acceptance drops rapidly below stop squark masses of about 200 GeV, due to the trigger and jet requirements. Therefore, and the analysis sensitivity does not surpass the 8 TeV result, which was specifically optimised for low-mass signals. Pair-produced scalar gluons with decays into two gluons are excluded up to a mass of 800 GeV. Pair-produced colorons coupling only to light quarks are excluded up to a mass of 1500 GeV. The results improve upon previous Run 1 searches and extend the constraints on stop squark masses.

## 7.9 Outlook

Since my role in this analysis was to perform the background fits, I will elaborate a bit here on their potential applicability.

The ABCD method was preferred for the background estimation, due to its ability to cover the full $m_{\mathrm{avg}}$ range and because the fit method is induces an additional uncertainty from the choice of a functional form. However, a fit could be used to give a less model-dependent background description that is more flexible for different signal shapes.

The prospect of estimating the background directly from a fit to the SR, was studied for future reference. Agreement was observed between the estimate given by the fit and the prediction of the ABCD method, as can be seen in Figure 7.11.

A new iteration of the RPV stop search, using the full Run-2 dataset, is currently under

**Table 7.3:** Observed numbers of events in the data $N_{\text{Data}}$ the estimated numbers of background events $N_{\text{Bkg}}$ and the expected numbers of stop squark signal events $N_{\text{Sig}}$ in the stop squark mass windows of the *b*-tagged signal region. Statistical and systematic uncertainties are given separately.

| $m_{\tilde{t}}$ [GeV] | Window [GeV] | $N_{\text{Data}}$ | $N_{\text{Bkg}}$ (± stat. ± syst.) | $N_{\text{Sig}}$ (± stat. ± syst.) |
|---|---|---|---|---|
| 100 | [100, 110] | 256 | 285 ±18 ± 51 | 308 ±18 ± 52 |
| 125 | [120, 135] | 803 | 798 ±28 ± 107 | 1090 ±40 ± 140 |
| 150 | [140, 160] | 809 | 789 ±23 ± 132 | 1510 ±40 ± 130 |
| 175 | [165, 185] | 544 | 555 ±16 ± 47 | 1300 ±40 ± 140 |
| 200 | [185, 210] | 592 | 554 ±13 ± 47 | 1220 ±40 ± 110 |
| 225 | [210, 235] | 414 | 436 ±11 ± 35 | 893 ±28 ± 90 |
| 250 | [230, 260] | 416 | 385 ±10 ± 32 | 750 ±60 ± 120 |
| 275 | [255, 285] | 302 | 283 ± 8 ± 24 | 480 ±50 ± 60 |
| 300 | [275, 310] | 242 | 250 ± 8 ± 23 | 390 ±40 ± 50 |
| 325 | [300, 335] | 181 | 179 ± 6 ± 17 | 273 ±33 ± 34 |
| 350 | [320, 365] | 169 | 161 ± 6 ± 16 | 225 ±25 ± 20 |
| 375 | [345, 390] | 110 | 111 ± 5 ± 12 | 147 ±16 ± 22 |
| 400 | [365, 415] | 80 | 96 ± 4 ± 11 | 114 ± 9 ± 12 |
| 425 | [385, 440] | 85 | 79 ± 4 ± 10 | 76 ±14 ± 11 |
| 450 | [410, 465] | 71 | 54.2± 3.0± 7.1 | 48 ± 9 ± 10 |
| 475 | [430, 490] | 67 | 46.8± 2.7± 6.5 | 40 ± 7 ± 5 |
| 500 | [455, 515] | 38 | 35.8± 2.3± 5.3 | 26 ± 5 ± 5 |
| 525 | [475, 540] | 31 | 35.1± 2.3± 5.5 | 21.7± 3.9± 2.8 |
| 550 | [500, 565] | 20 | 30.2± 2.1± 5.0 | 12.4± 2.5± 2.3 |
| 575 | [520, 590] | 14 | 26.3± 2.0± 4.6 | 17.5± 2.7± 3.5 |
| 600 | [545, 620] | 14 | 19.5± 1.6± 3.5 | 11.4± 0.9± 1.5 |
| 625 | [565, 645] | 15 | 15.8± 1.4± 3.0 | 9.3± 1.5± 1.4 |
| 650 | [585, 670] | 14 | 14.6± 1.3± 2.9 | 6.9± 1.2± 1.1 |
| 675 | [610, 695] | 13 | 13.6± 1.3± 2.8 | 5.5± 0.8± 0.6 |
| 700 | [630, 720] | 6 | 12.1± 1.2± 2.6 | 4.3± 0.6± 0.5 |
| 725 | [655, 745] | 5 | 9.9± 1.1± 2.2 | 4.4± 0.6± 0.8 |
| 750 | [675, 770] | 4 | 8.4± 0.1± 1.9 | 3.4± 0.5± 0.5 |
| 775 | [700, 795] | 8 | 6.9± 0.9± 1.6 | 2.4± 0.3± 0.5 |
| 800 | [720, 820] | 7 | 5.3± 0.7± 1.3 | 1.7± 0.3± 0.2 |

development. The possibility of using a fit method for mass points above 500 GeV and the ABCD method to look for lower mass resonance is being explored. The motivation arises from the fact that the $\Delta R_{min}$ pairing does not always correctly assign the resonance candidates at high masses. Therefore the signal exhibits a tail extending to lower $m_{\text{avg}}$ values which degrades the efficiency of the mass window selection. Alternative pairing methods for the higher mass resonances induces a correlation between the mass asymmetry $\mathcal{A}$ and $\cos\theta^{*}$. This correlation means that the ABCD can not be used and the fit method is preferrable.

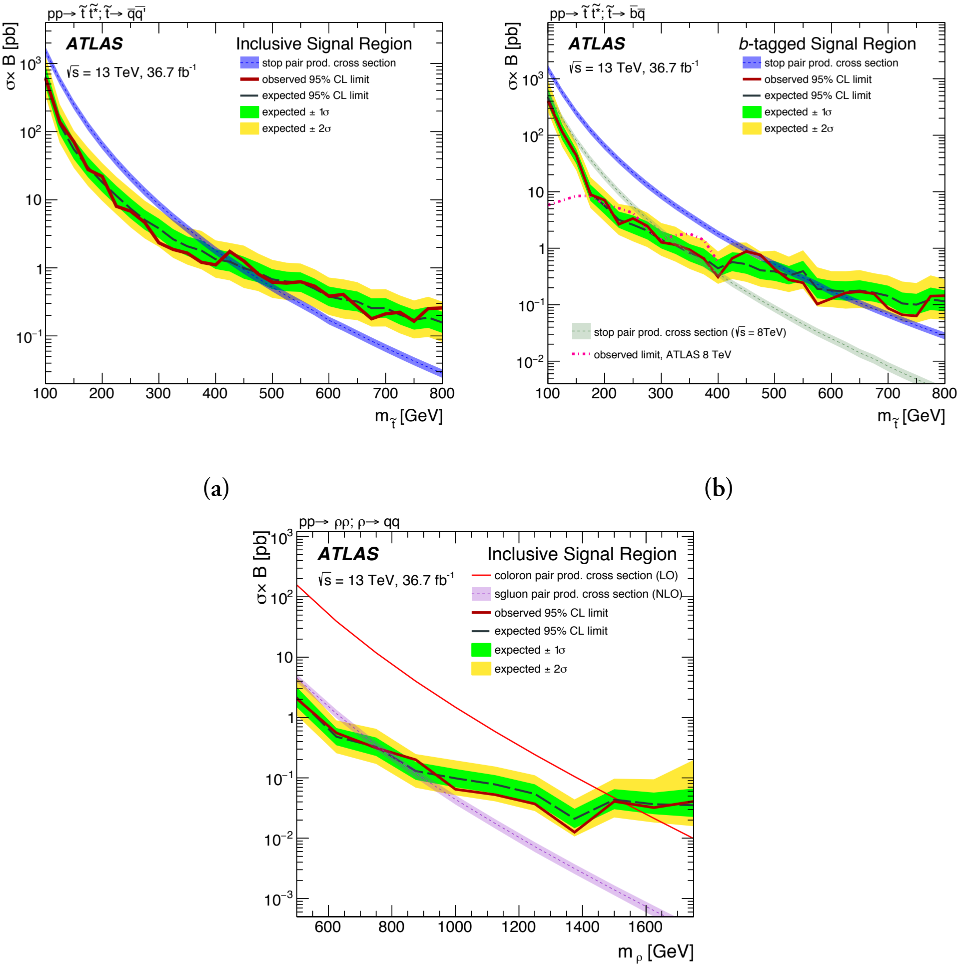

(a)

(b)

(c)

**Figure 7.10:** The observed (red line) and expected (dashed, black line) 95% confidence limit (CL) on the cross section times branching ratio, $\sigma \times B$, for pair-production of a stop squark decaying to (a) $qq$, (b) $bs$, and (c) pair-production of a colorons decaying to $qq$ or ssguons to $gg$. The green and yellow band indicate the $\pm 1\sigma$ and $\pm 2\sigma$ ranges around the expected limits. The CLs are compared to the corresponding theoretical cross-sections, where the width of the band corresponds to the $\pm 1\sigma$ variation due to theoretical uncertainties in the signal production cross-sectiongiven by renormalisation and factorisation scale and PDF uncertainties [85].

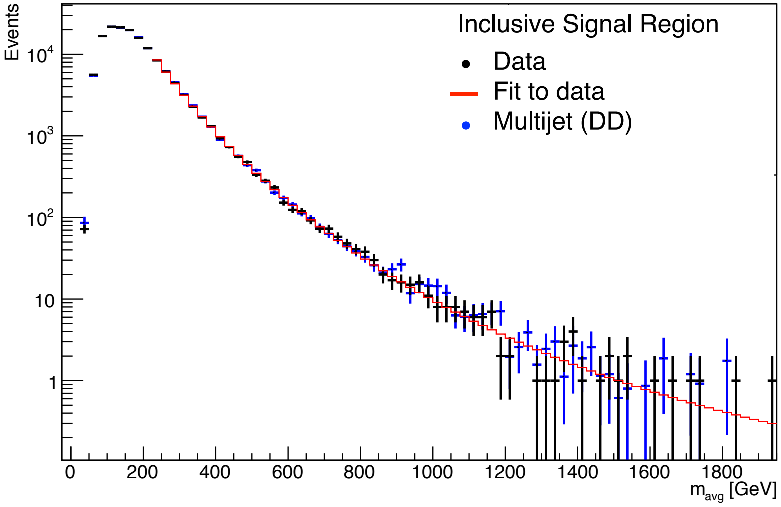

(a)

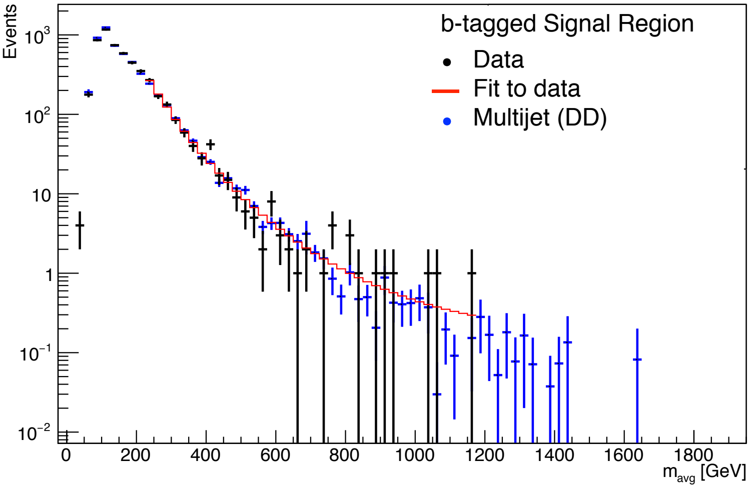

(b)

**Figure 7.11:** Functional fit (red line) to the $m_{\text{avg}}$ spectrum as measured in the inclusive signal region (a) and the $b$-tagged signal region (b). The fit is shown along with the data (black points) and the data-driven multijet background prediction (blue points). The vertical lines represent the statistical uncertainties.

# Chapter 8

# Dark Jet Resonances

Diverse efforts to uncover the nature of dark matter have been ongoing for decades through attempts of both direct and indirect detection. So far, we have not seen any significant hints towards an explanation of physics beyond the Standard Model. The focus of searches have long been on the promising category of dark matter candidates known as Weakly Interacting Massive Particles, or WIMPs for short, which were discussed in Section 2.4.2. While searches for WIMPs continues with increasingly sensitive detectors, it is worth to also consider models which yield different signatures, that could be missed by the WIMP searches.

One possibility is to introduce a confining hidden sector, where the lightest stable hadron is a dark matter candidate. Such models of composite dark matter, also referred to as "dark QCD", have several advantages which were highlighted in Section 2.4.4.

Here we consider scenarios where the hidden visible sector are connected via a TeV scale mediator, that preferrably decays to two dark quarks which are much lighter. The energy of these dark quarks will then be much larger than the confinement scale of the dark sector, causing them to shower and then hadronise. The produced dark mesons may decay back to visible SM particles, and be detected as "dark jets". This process is illustrated in Figure 8.1.

Several categories of dark QCD signatures were also described in Section 2.4.4. In this chapter I present an ongoing ATLAS search for a dijet resonance that links the Standard Model to a confined hidden sector very similar to the QCD sector of the Standard Model. The aim of the analysis is to demonstrate the possibility to distinguish QCD-like dark jets from the Standard Model background using jet characteristics and substructure variables.

The analysis is conducted in a "blinded" manner. That means we do not study data where

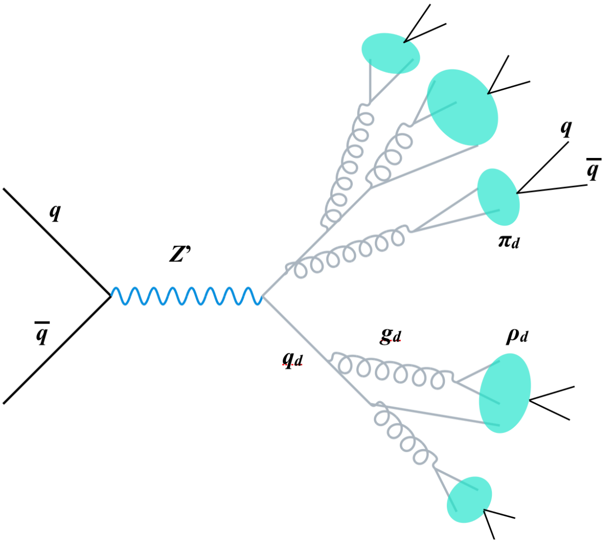

**Figure 8.1:** Schematic illustration of the formation of "dark jets". A mediator $Z'$ decays to two dark quarks $q_d\bar{q}_d$, which radiate dark gluons $g_d$. As the energy of the partons reach the confinement scale of the hidden gauge group, they form dark hadrons. The dark hadron promptly decay back to Standard Model quarks $q\bar{q}$.

we would expect to see an effect of the phenomena we are searching for, until the analysis procedure is finalised and approved by an internal ATLAS review. Instead, the methods are developed and tested based on simulated data and selections of collision data where it is safe to say, if a signal could appear it should already have been discovered by previous searches. Since the presented analysis is still blinded, I do not show any preliminary results of data where we can expect to see signal.

The benchmark signal models that we use for testing and optimising the analysis strategy are described in Section 8.1 and the data simulation in Section 8.4. The event reconstruction is outlined in Section 8.5 followed by a discussion of the pre-selection and final selection of events in Sections 8.3 and 8.6. The methods used for background estimation are presented in Section 8.7 and the expected systematic uncertainties are discussed in Section 8.8. Finally considerations for future iterations of the analysis are presented in Section 8.9.

## 8.1 Benchmark signal models

The analysis is tested and optimised for different realisations of confined hidden particle sectors, which were proposed in [44]. Four sets of benchmark model parameters are studied in attempt to cover more of the diverse phenomenologies a dark QCD-like sector could generate. All four models are described by a non-Abelian gauge group $SU(N_\mathrm{d} = 3)$ with confinement scales $\Lambda_\mathrm{d}$ of order $\mathcal{O}$(GeV) which is significantly larger than the confinement scale of the Standard Model, $\Lambda_\mathrm{QCD}$ of order $\mathcal{O}$(100 MeV).

In order to produce dark quarks from proton-proton collisions, these model require a mediator between the hidden and the visible sector. The mediator can be either a vector boson or a bi-fundamental scalar, but must be charged under both the SM SU(3) and the dark $SU(N_\mathrm{d})$ gauge group. In the following we assume the mediator is a vector boson $Z'$.

In all four models, the lightest dark mesons $\pi_\mathrm{d}$ and $\rho_\mathrm{d}$ are the dominant components the dark jets. The $\rho_\mathrm{d}$ mesons decay promptly to $\pi_\mathrm{d}$ which in turn decay promptly to SM particles. The lightest dark baryon is stable and could be a dark matter candidate. However, with $N_\mathrm{d} = 3$ the dark baryons are expected to constitute only 10% of the dark jets, which is considered negligible by the authors and not included in the model files. Therefore, only $\pi_\mathrm{d}$ and $\rho_\mathrm{d}$ are considered in the simulation of signal events, such that the fraction of invisible constituents in the dark jets is zero for all four models.

The parameters of the four benchmark models are summarised in Table 8.1. An important difference to notice is the size of the confinement scale $\Lambda_\mathrm{d}$ which results in a larger running QCD coupling $\alpha_\mathrm{d}$ in two of the models. A comparison is shown in Figure 8.2 where it is also seen that the coupling is always stronger than in the Standard Model.

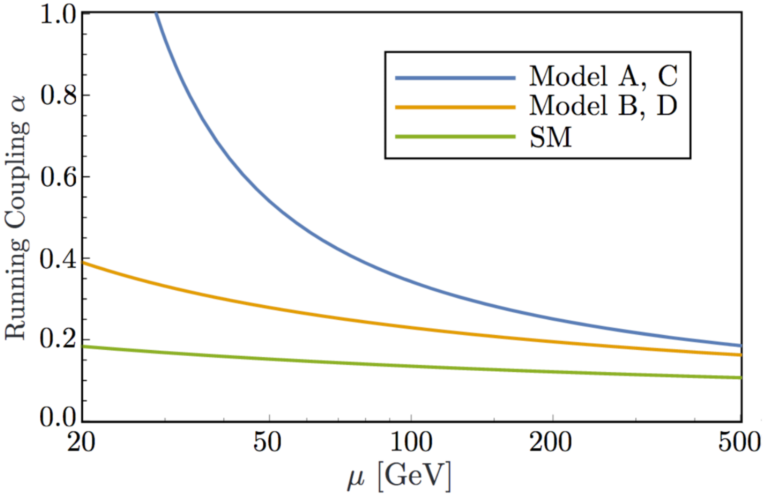

**Figure 8.2:** Running coupling of the four benchmark models compared to the strong coupling of the Standard Model, according to [44].

Another striking difference between the parameter sets, is the decay channels of the dark pion. For models A and B the pion decays to a SM quark pair via the mediator $Z'$ with a width governed by the relation:

$$\Gamma(\pi_\mathrm{d} \to q\bar{q}) = \frac{3\kappa^4 f_{\pi_d}^2 m_q^2}{32\pi M_{Z'}^4} m_{\pi_d} \tag{8.1}$$

Here $\kappa = 1$ is the couplings between the mediator, quark, and dark quark, and $f_{\pi_d}$ is the pion decay constant. This leads to prompt decays, i.e. decay lengths less than 1 mm, if the pion mass $m_{\pi_d}$ is several GeV and the mediator mass is several hundred GeV.

Prompt decays of the dark pion can also be enforced by extending the hidden gauge group to $SU(N_d) \times U'(1)$, such that the dark quarks is also charged under $U'(1)$. This symmetry is introduced for models C and D, such that the dark pion decays promptly to a pair of dark photons. The dark photons can then decay to SM particles through kinetic mixing with the SM photon,

$$\mathcal{L}_{\text{kin.mix.}} = \frac{1}{2}\epsilon F^{\mu\nu} F'_{\mu\nu} \tag{8.2}$$

where $F$ and $F'$ are the field strength tensors of the SM $U(1)$ and the dark $U'(1)$, respectively and $\epsilon$ is a dimensionless parameter. By setting the dark photon mass $m_{\gamma'}$ to be of the order $\mathcal{O}(1\ \text{GeV})$, prompt dark photon decays can be achieved if $\epsilon \gtrsim 10^{-5}$. According to [95] such parameter values for dark photons have not yet been excluded.

**Table 8.1:** Parameter choices for the four benchmark models considered in this analysis, as proposed in [44]. Common for all four models is the dimension $N_d = 3$ of the gauge symmetry SU($N_d$) and the meson decay channel $\rho_d \to \pi_d \pi_d$.

| | $n_f$ | $\Lambda_d$ (GeV) | $m'_q$ (GeV) | $m_{\pi_d}$ (GeV) | $m_{\rho_d}$ (GeV) | $\pi_d$ decay mode |
|---|---|---|---|---|---|---|
| $A$ | 2 | 15 | 20 | 10 | 50 | $\pi_d \to c\bar{c}$ |
| $B$ | 6 | 2 | 2 | 2 | 4.67 | $\pi_d \to s\bar{s}$ |
| $C$ | 2 | 15 | 20 | 10 | 50 | $\pi_d \to \gamma'\gamma'$,<br>$m_{\gamma'} = 4.0\,\text{GeV}$ |
| $D$ | 6 | 2 | 2 | 2 | 4.67 | $\pi_d \to \gamma'\gamma'$,<br>$m_{\gamma'} = 0.7\,\text{GeV}$ |

The decay of the dark photon also differs between model C and D due to the different dark photon masses. This turns out to be relevant for the dijet mass resolution in Section 8.5. The dark photon decays are sumamrised in Table8.2.

**Table 8.2:** Overview of the dark photon decay channels and branching ratios for model C and D.

| BR for $\gamma' \rightarrow$ | Model C | Model D |
|---|---|---|
| $u\bar{u}$ | 0.06 | - |
| $d\bar{d}$ | 0.22 | - |
| $c\bar{c}$ | 0.22 | - |
| $s\bar{s}$ | 0.06 | - |
| $e^+e^-$ | 0.17 | 0.15 |
| $\mu^+\mu^-$ | 0.17 | 0.15 |
| $\pi^+\pi^-$ | - | 0.7 |

## 8.2 Analysis strategy

The dominant background to the Dark Jet Resonance Search comes from Standard Model QCD processes. A characteristic feature of such multijet events, is that the invariant mass of the two leading jets $m_{\text{JJ}}$ forms a smoothly falling spectrum. Conversely, the invariant mass of the two dark jets from the decay of a narrow width mediator should form a mass peak around the mediator mass. This means that we would see a resonant structure in the $m_{\text{JJ}}$ spectrum over the SM background, if the signal and background events occurred with similar probabilities. If that was the case we would, of course, already have seen the resonance in other dijet or diboson searches. Therefore, it is safe to assume that signal events are much more rare than the background event. So, in order to see the resonant bump we must suppress the background distribution with an event selection that favors signal events. The basic principle of the analysis strategy is to first reduce the relative amount of background in the data sample, and then look for a bump over smoothly falling background in the $m_{\text{JJ}}$ spectrum, as illustrated in Figure 8.3.

### 8.2.1 Event selection strategy

Variations from SM QCD can occur at all stages of the dark jet formation: The parton showering, the parton fragmentation to dark mesons, and the subsequent decay of dark mesons to SM particles. These variation lead to different radiation patterns inside the jet, which is typically quantified by so-called jet substructure variables.

The stronger QCD coupling of the dark sectors is responsible for the most striking difference in phenomenology between the benchmark models and the Standard Model; namely that the dark quarks radiate more during the parton shower stage of the jet formation.

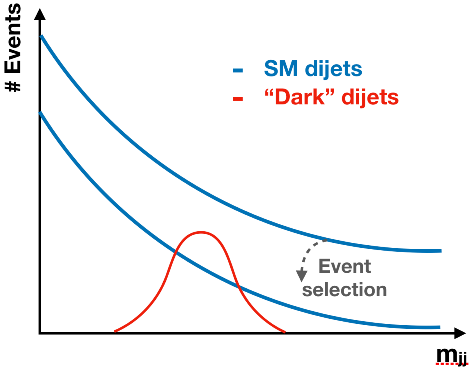

**Figure 8.3:** Illustration of the Dark Jet Resonance search strategy.

Thus dark jets are wider and have larger particle multiplicity. The reader might recall from Section 6.1 that this is the same characteristic which lets us distinguish between gluon and quark jets.

Due to the similar requirements of a dark jet tagger, we initially studied four different jet substructure variables, which had previously been found to perform well in quark/gluon-tagging: The number of tracks $n_{\mathrm{trk}}$ associated with the jet which serves as a proxy for the constituent particle multiplicity, the jet width, the two-point ECF ratio $C_1$, and the fraction of jet energy deposited in the electromagnetic calorimeter $R_{EM}$. In accordance with the findings of quark/gluon jet studies, we concluded that the track multiplicity, is the best single observable for discriminating between dark jets and QCD jets. A comparison between the distribution of $n_{\mathrm{trk}}$ for the multijet background events and the four signal models is shown in Figure 8.4.

Figure 8.4 illustrates that variations of the underlying parameters and decay modes of our benchmark models lead to different phenomenology among the types dark jets. Not only does the $n_{\mathrm{trk}}$ distribution of signal jets differ from QCD jets, it also differs depending on the signal model and the mediator mass. While $n_{\mathrm{trk}}$ is the best discriminating variable for all the signal scenarios combined, it is not true for each one individually. Particularly for model B, $n_{\mathrm{trk}}$ is not the strongest variable for discriminating from the background, but rather $R_{EM}$. However, a cut on $R_{EM}$ would reduce the sensitivity to the other three models, which can be seen in Figure 8.5.

The varying phenomenology of the targeted signals, could call for defining several event selections, optimised for each possibility. But, since the underlying parameters of dark QCD are not well-constrained by theory or any former experiments, we have refrained from fully optimising the event selection for the specific parameter sets tested here, and

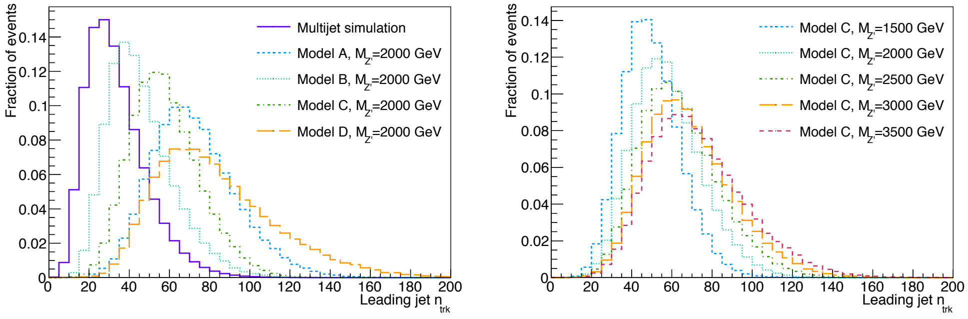

(a) (b)

**Figure 8.4:** The distribution of the jet track multiplicity $n_{\mathrm{trk}}$ for (a) the multijet background and all the four benchmark models with $M_{Z'} = 2000\,\mathrm{GeV}$, and (b) Model C with each of the simulated resonance mass points.

keep the search as broad as is sensible.

Since it is the first time ATLAS attempts a jet substructure-based search for a dark QCD-like sector, the strategy has been to keep the analysis simple, demonstrate the feasibility of it, and leave extensions and optimisations of the search to future iterations. For the sake of simplicity, and to make the search more inclusive, we chose to base the event selection on only $n_{\mathrm{trk}}$, as that is the single most discriminating feature overall. A detailed description of the final event selection is given in Section 8.6, and a discussion of the potential for doing a multivariate analysis is given in Section 8.9.

### 8.2.2 Resonance finding strategy

To seperate the potential signal component from the background component of the final event selection, we make use of the differenc in the expected shape of the $m_{\mathrm{JJ}}$ distribution. As opposed to the RPV stop search, which can be categorised as a counting analysis, the dark jet search is a shape analysis. A smooth parameterisation of the background shape is obtained directly from data by use of a functional fit. The idea is then to look for a localised excess in data above the background estimate. More information on the background estimation is presented in Section 8.7.

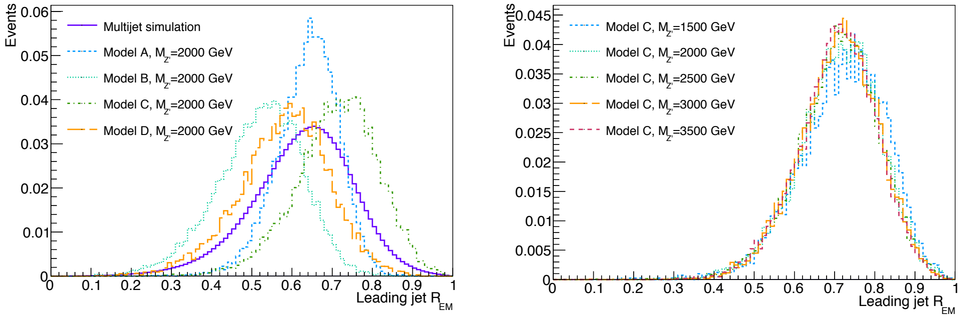

(a) (b)

**Figure 8.5:** The distribution the jet energy fraction deposited in the electromagnetic calorimeter $R_{EM}$ for (a) the multijet background and all the four benchmark models with $M_{Z'} = 2000\,\text{GeV}$, and (b) Model C with each of the simulated resonance mass points.

## 8.3 Data and preselections

Like in the search for RPV stop squarks, described in Section 7.2, the data is filtered through the trigger system and a baseline preselection before the actual analysis is done. The criteria closely follow the preselection used in the recently published ATLAS search for a diboson resonance in final states with two large-radius jets [96].

### 8.3.1 Data sample

The search is performed with an LHC data sample of $\sqrt(s) = 13\,\text{TeV}$ $p\overline{p}$ collisions collected with the ATLAS experiment from 2015 to 2018. Events are required to be recorded during stable beam conditions, and come from luminosity blocks where all detector subsystems were operating above the $90\%$-level. This corresponds to a total integrated luminosity of $138\,\text{fb}^{-1}$.

For this analysis, we are interested in events with two wide jets of fairly high $p_{\text{T}}$, so the lowest unprescaled, large-$R$ jet trigger for each data period is used. At the first level of the two-level ATLAS trigger system (see Section 3.2), events are required to have two (small-radius) jets with transverse energy of at least $100\,\text{GeV}$ at the electromagnetic scale. At the second stage, at least one trimmed and calibrated large-$R$ jet is required to satisfy a $p_{\text{T}}$ threshold of $p_{\text{T}} > 460\,\text{GeV}$.

### 8.3.2 Data quality cuts

All events are required to have a primary vertex with at least two associated tracks. The primary vertex is determined as the one with the largest sum of $p_{\mathrm{T}}$ over all tracks that have $p_{\mathrm{T}} > 0.5$ GeV and are associated with the vertex.

Furthermore, events are also required to be recorded during stable beam conditions, and during luminosity blocks where all detector sub-systems were operating above the 90%-level. Events are rejected if they are marked as corrupted by either the LAr calorimeter, Tile calorimeter or the Semiconductor Tracking Detector (SCT). Events are also vetoed if they are marked as incomplete or contain a noise burst in the LAr calorimeter [86].

To reduce contributions from non-collision sources, jets that might be reconstructed from calorimeter noise, the beam halo and cosmic rays, are identified according to [87]. Events that contain a small-*R* jet classified as *bad-loose* are rejected.

### 8.3.3 Monte Carlo quality cuts

The overlaying of pile-up events to the simulated hard-scatter interaction can cause spurious events, where a jet from a low-$p_{\mathrm{T}}$ slice migrates to a higher $p_{\mathrm{T}}$ bin. These events end up with a very large weight, and dominate the $p_{\mathrm{T}}$ spectrum in the high tail. Thus, the $m_{\mathrm{JJ}}$ spectrum is also distorted to have too many events in the high end of the distribution which are not physical.

In order to mitigate this effect, we remove events where the average $p_{\mathrm{T}}$ of the leading and sub-leading jet is within 30% of the leading jet truth $p_{\mathrm{T}}$:

$$0.7 < p_{\mathrm{T}}^{\mathrm{avg}}/p_{\mathrm{T}}^{\mathrm{truth}} < 1.3, \quad p_{\mathrm{T}}^{\mathrm{avg}} = \frac{p_{\mathrm{T}}^{\mathrm{lead}} + p_{\mathrm{T}}^{\mathrm{sub}}}{2} \tag{8.3}$$

### 8.3.4 Topological selection

Finally we require the events to have two large-*R* jets, reconstructed and calibrated offline according to Chapters 4 and 5 with $p_{\mathrm{T}}^{\mathrm{lead}} > 500$ GeV, $p_{\mathrm{T}}^{\mathrm{sub}} > 400$ GeV, $m_{\mathrm{JJ}} > 1300$ GeV, and $|\eta| < 2.0$. The latter requirement guarantees a good tracking efficiency, which is important for our final event selection. The $p_{\mathrm{T}}$ and $m_{\mathrm{JJ}}$ cuts ensure that the analysis is performed in a region where the trigger we use is $\sim 100\%$ efficient.

A comparison between the collision data and simulated data following the entire preselection is shown in Figure 8.6. Apart from the sub-leading jet $p_{\mathrm{T}}$, variations in the highstatistic regions are less than 10%. The disagreement at low $p_{\mathrm{T}}$ for sub-leading jets motivated the $p_{\mathrm{T}}$ cut at 400 GeV, while we are still investigating the source of this disagreement.

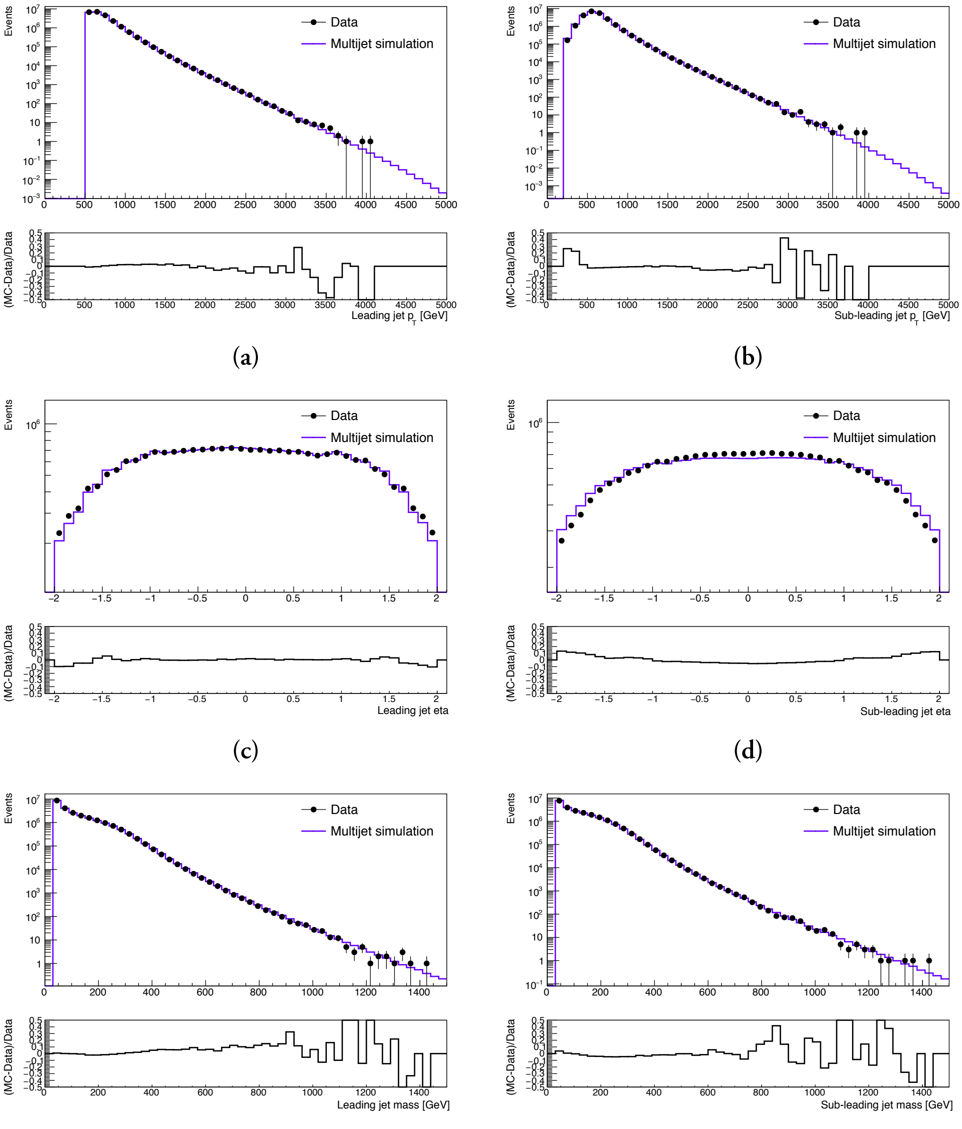

(a) (b)

(c) (d)

(e) (f)

**Figure 8.6:** Data to Simulation comparisons following the quality and topological preselection cuts. Data points are shown as black points with a vertical line representing the statistical uncertainty. The solid purple line shows the multijet samples simulated with PYTHIA 8. In the bottom panel, the relative difference in each bin is shown.

## 8.4 Simulated data samples

The multijet background of this search is estimated empirically from the $m_{JJ}$ distribution observed in data. However, MC simulations of both signal and background events are used to validate the background estimation method and to optimise the event selection.

The simulated data samples used for this analysis reflect the data taking conditions of all years of data we analyse, meaning 2015-2018. The samples were mainly produced with the NNPDF23LO parton distribution functions, and using the MC generator tune A14 [90]. The generator tune is of particular importance to this analysis, since the parameters enter in the parton shower and hadronisation processes, and those in turn govern the jet signatures we are looking for. The A14 tune is preferred due to better modeling of substructure observables than e.g. the AZNLO tune which is often used in Higgs analyses, e.g. [97]. This property illustrated in Figure 8.7 by example of the jet charged particle multiplicity in Run 1 data.

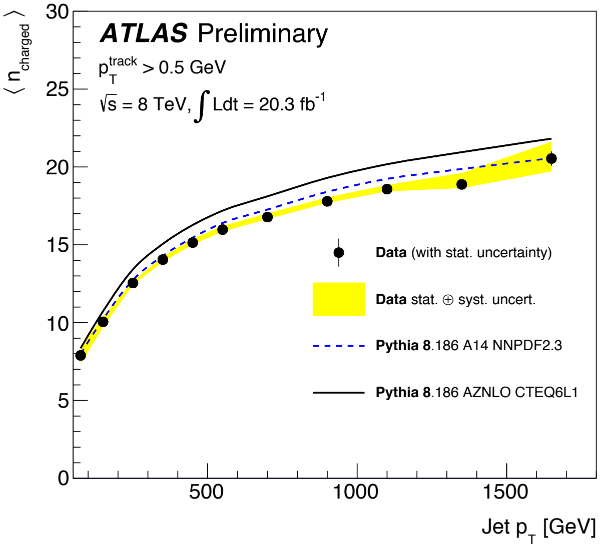

**Figure 8.7:** Comparison of the particle-level charged particle multiplicity of jets from ATLAS Run 1 data and Pythia 8 with the A14 and AZNLO tunes [83].

### 8.4.1 Signal simulation

To test and optimise the analysis for the four benchmark models described in Section 8.1, we need simulated data samples that correspond to these models. The PYTHIA Hidden-Valley implementation of the processes $pp \to Z_d \to q_d q_d$ is used for generating signal events. Separate samples are produced with six different mediator masses for each benchmark model. The tested mass points range from 1000 GeV to 3500 GeV in step of 500 GeV.

### 8.4.2 Background simulation

The dominant background process for this search is multijet QCD processes. Simulated MC samples of such events are used to optimise the event selection and test the background description which will eventually be derived from data.

PYTHIA 8 is used to generate the multijet events, including the showering and hadronisation processes. This is done for separate slices of leading jet $p_{\mathrm{T}}$, after which the events are weighted to produce a smoothly falling $p_{\mathrm{T}}$ spectrum when combining the slices.

## 8.5 Event reconstruction

The dark QCD models we consider in this work predict wider jets than SM QCD. Therefore, events are clustered into large-radius jets using the anti-$k_t$ algorithm with $R = 1.0$. The input objects passed to the jet algorithm are LCW-weighted topoclusters, and contributions from pile-up and the underlying event are mitigated with the grooming technique, called *trimming*. The jets are calibrated with the full chain of calibration steps, as described for large-*R* jets in Section 5.

The jet definition used in this analysis follows the current recommendations of ATLAS, for which a full calibration is derived centrally. However, there is a potential for improving the sensitivity of this search by considering other jet definitions. Particularly the trimming algorithm might not be optimal for our purpose. It is optimised to not only mitigate pile-up, but also improve the identification of large-radius jets where the energy is concentrated around two or more prongs, by removing soft radiation. As we saw in Section 6.1, prong-like jets are typically created by the hadronic decay of heavy, boosted particles, e.g. a boosted $W$ or top quark. These object are the main interest to most analyses that use large-radius jets. Our dark jets, on the other hand, are initiated by a single dark quark, and therefore do not exhibit prong-like substructure. However, they do have many soft components which are partially removed by the trimming algorithm. This makes the $m_{\mathrm{JJ}}$ distribution wider and shifts the peak to significantly lower masses than the simulated resonance mass. The reconstructed $m_{\mathrm{JJ}}$ distribution, computed from trimmed and calibrated model C jets, is shown for different mediator masses in Figure 8.8.

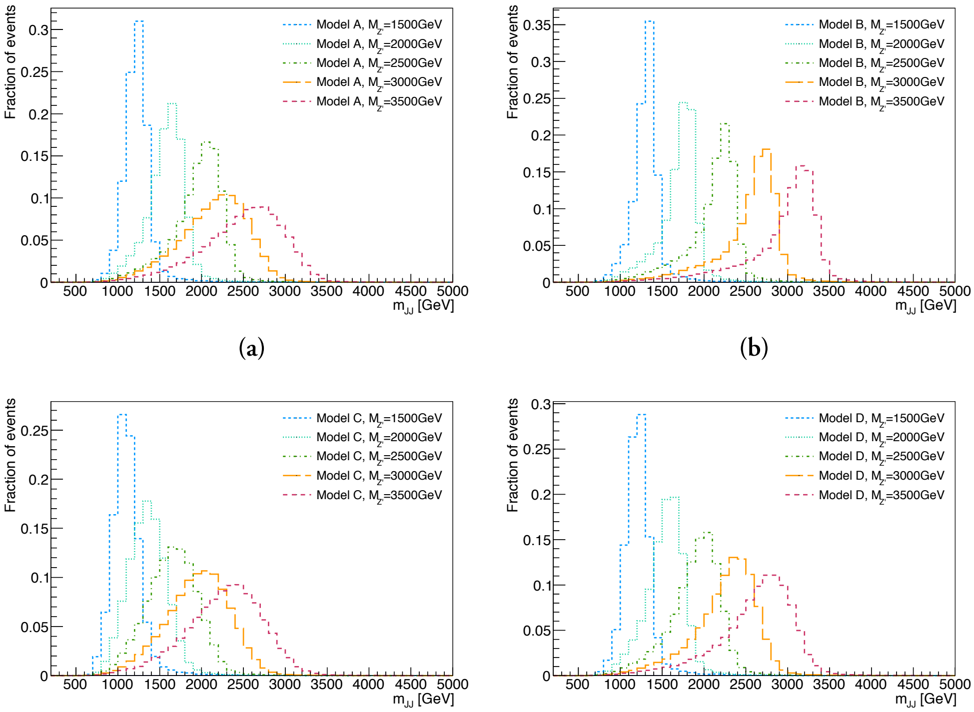

(a) (b) (c) (d)

**Figure 8.8:** Invariant mass distributions of the two leading jets in signal events for a given model and mediator mass. From the top left to the bottom right figure, the distributions are shown for Model A, B, C, and D, respectively.

Here it can be seen that the distributions peak at significantly lower values than the mediator mass. A detailed discussion of potential improvements to the jet reconstruction is given in Section 8.9.

## 8.6 Signal region

The analysis strategy described in Section 8.2 requires that the signal region satisfies at least two conditions: The background distribution in the final data sample must be smoothly falling without peak-like structures, in order to distinguish the mass peak signature of a heavy resonance decay, and the amount of background in the signal region must be large enough to allow for a robust parameterisation.

To obtain a good sensitivity for the search, the event selection must enhance the significance of potential signal relative to background, while satisfying the above mentioned conditions. As mentioned in 8.2 the signal region for this search is defined by an event selection based on the track multiplicity of the jets. More specifically on the variable $n_{\mathrm{trk}}$, which is defined as the number of tracks with $p_{\mathrm{T}} > 500$ MeV, that are associated with the jet prior to any jet grooming. This section discusses the challenges and considerations that govern the signal region definition.

### 8.6.1 Challenge of $n_{\mathrm{trk}}$-based event selection

An optimisation over all the tested benchmark models combined implies that a strict cut on $n_{\mathrm{trk}}$ of the two leading jets gives the best significance. Figure 8.9 compares the distribution of $n_{\mathrm{trk}}$ for simulated background and signal jets, where the signal distribution includes all models and mass points.

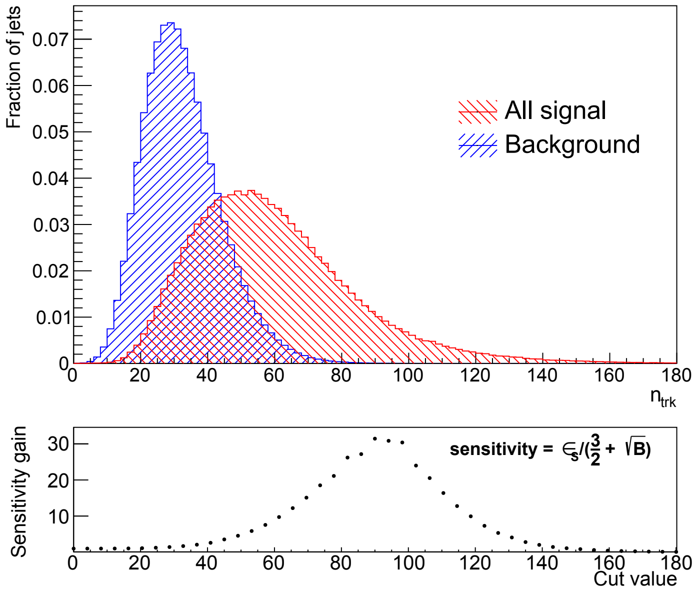

**Figure 8.9:** The top panel shows the distributions of $n_{\mathrm{trk}}$, defined as the number of charged tracks with $p_{\mathrm{T}}$ >500 MeV, that are associated with the jet prior to trimming. The distribution is shown for the multijet background (blue) and all signal samples combined (red). The lower panel shows the significance gain obtained by requiring that the two leading jets have an $n_{\mathrm{trk}}$ larger than the cut value.

The lower panel shows the gain in significance obtained by a cut on both jets at the given $n_{\mathrm{trk}}$ value relative to the significance when no cut is applied. To estimate the significance

$\sigma$ of a given cut we use the metric

$$\sigma = \epsilon_S/(\frac{3}{2} + \sqrt{B}) \tag{8.4}$$

where $\epsilon_S$ is the signal efficiency and $B$ is the number of background events. The effect of a certain cut value $c$ is evaluated as the sensitivity gain, $\sigma(c)/\sigma(c = 0)$. The offset value of $3/2$ was optimised for the hadronic diboson search [96], but the result of the optimisation is not very sensitive to this value.

Looking at Figure 8.9, it appears that the optimal definition of a signal region would be a cut requiring $n_{\mathrm{trk}} \gtrsim 90$. This achieves the highest significance gain, as computed for all signal models combined. However, the signal region resulting from such a cut, does not meet the condition of yielding sufficient background statistics to perform a robust fit. With a background efficiency of order $\mathcal{O}(10^{-7})$, the cut leaves only around 50 background events, according to the simulated multijet sample. Furthermore, such a strict event selection would have almost no sensitivity to some of the models we tested. Figure 8.10 shows the same $n_{\mathrm{trk}}$ distributions and sensitivity cut as 8.9, but for each benchmark model separately, still combining all mass points. It shows that most events from model B would be rejected by this event selection.

A cut around $n_{\mathrm{trk}} \gtrsim 70$, which would leave around $\mathcal{O}(1000)$ events, might be a better compromise. But a third problem remains. The track multiplicity of SM QCD jets is correlated with the jet $p_{\mathrm{T}}$ and thus with $m_{\mathrm{JJ}}$, such that a larger fraction of events at high $m_{\mathrm{JJ}}$ have a higher $n_{\mathrm{trk}}$. This feature can be seen in Figure 8.11, where the relative distribution of leading jet $n_{\mathrm{trk}}$ is shown as function of $m_{\mathrm{JJ}}$. Because the number of events drops exponentially with $m_{\mathrm{JJ}}$, each bin is normalised to the integral of the $m_{\mathrm{JJ}}$ bin, to better see the effect.

The correlation between $n_{\mathrm{trk}}$ and $m_{\mathrm{JJ}}$ means that any given cut on $n_{\mathrm{trk}}$ removes a larger fraction of the events at low $m_{\mathrm{JJ}}$, thereby changing the shape of the background distribution. In Figure 8.12, the shape of the inclusive multijet background distribution (following the preselections) is compared to the distribution following a cut at $n_{\mathrm{trk}} = 70$. The $m_{\mathrm{JJ}}$ distribution is also shown for Model A with $M_{Z'} = 3\,\mathrm{TeV}$ which to how the shape of the signal mass peak becomes harder to distinguish from the shape of the background. Furthermore, in the inlcusive event selection, the $m_{\mathrm{JJ}}$ distribution starts to fall off smoothly from $m_{\mathrm{JJ}} \sim 1\,\mathrm{TeV}$, meaning that the fit can start from $1.3\,\mathrm{TeV}$ where we know the trigger is fully efficient. With a cut $n_{\mathrm{trk}} > 70$, the $m_{\mathrm{JJ}}$ distribution starts to fall off from $m_{\mathrm{JJ}} \sim 2\,\mathrm{TeV}$, giving a more narrow window in which we can perform a fit and do the search. This means we would become insensitive to the lower signal mass points.

To address this third problem, we have designed a variable that enforces a uniform back-

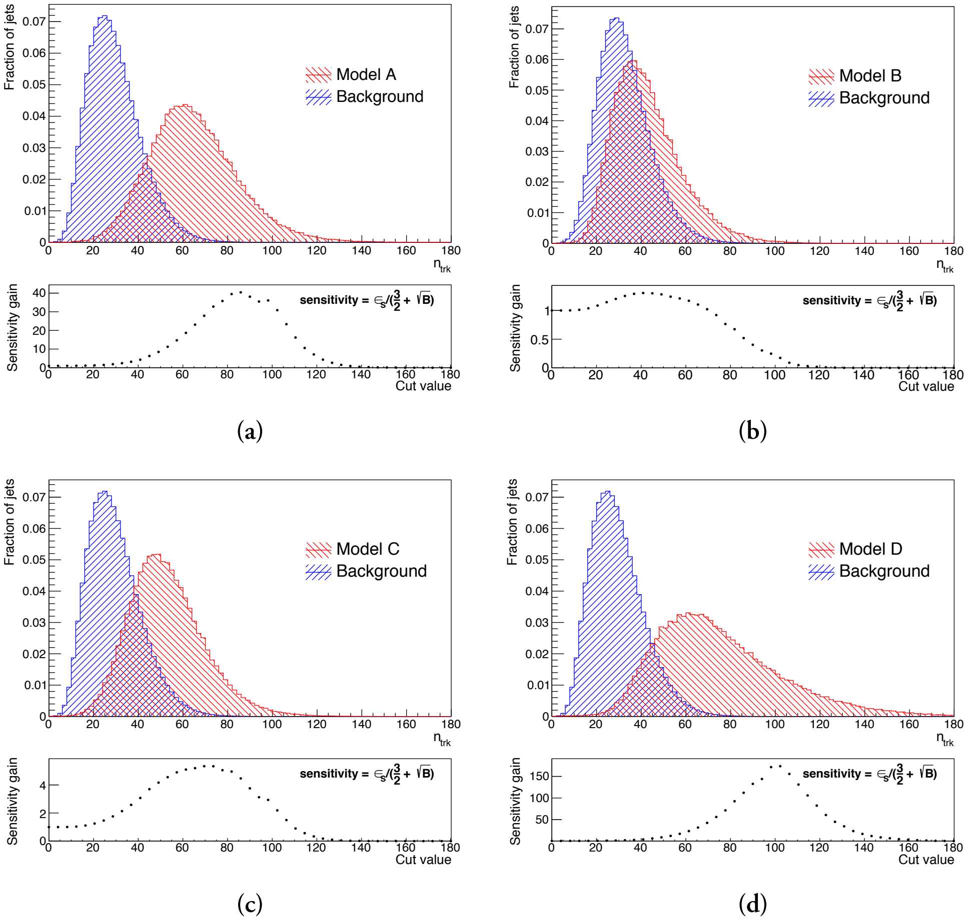

(a)

(b)

(c)

(d)

**Figure 8.10:** Distributions of the charged track multiplicity $n_{\text{trk}}$ for the simulated multijet background and each of the signal models. From the top left figure to the bottom right is shown the $n_{\text{trk}}$ distribution for model A, B, C, and D, respectively. The lower panel shows the significance gain obtained by requiring that the two leading jets have an $n_{\text{trk}}$ larger than the cut value.

ground selection efficiency across the full range of $m_{\text{JJ}}$.

### 8.6.2 Fixed-efficiency regression

To enforce a uniform selection efficiency across all $m_{\text{JJ}}$ bins we employ a decorrelation method called Fixed-Efficiency Regression. This method is described and tested for the selection of hadronically decaying $W$ bosons in [98].

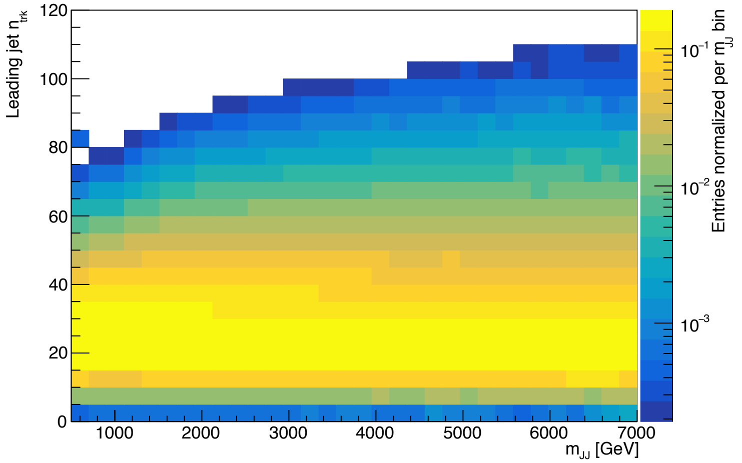

**Figure 8.11:** Distribution of leading jet $n_{\mathrm{trk}}$ relative to the integrated number of events in each $m_{\mathrm{JJ}}$ bin, as function of $m_{\mathrm{JJ}}$.

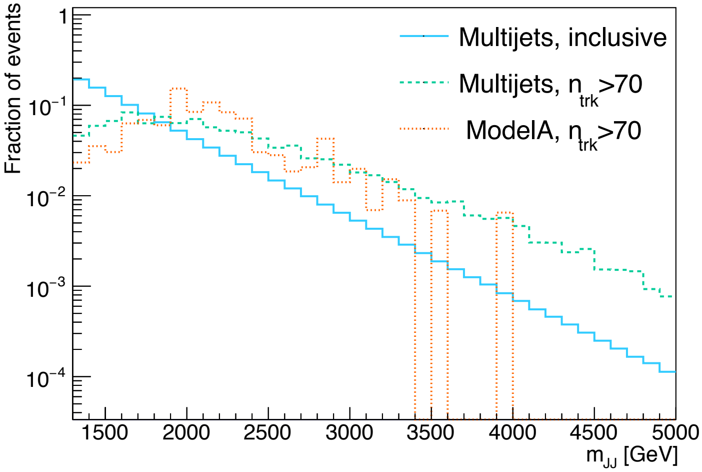

**Figure 8.12:** The $m_{\mathrm{JJ}}$ spectrum shown for background events with only baseline cuts applied (solid blue), or with a cut at $n_{\mathrm{trk}}$ >70 applied to the leading jets (dashed green). The background distribution are compared to the corresponding distribution for Model A with a mediator mass of $M_{Z'} = 3000$ GeV (dotted orange).

The Fixed-Efficiency Regression is performed in the following steps: First, the desired background efficiency, called the target efficiency $\epsilon$, is chosen. Then, the cut value on $n_{\mathrm{trk}}$ that corresponds to a background efficiency of $\epsilon$ is evaluated in bins of $m_{\mathrm{JJ}}$. This profile is fitted to give a continuous description of expected $n_{\rm trk}$ percentiles $P^{\epsilon}$ as a function of $m_{\rm JJ}$. A new observable $n^{\epsilon}_{\rm trk}$ is then formed for each jet by subtracting from $n_{\rm trk}$ the $P^{\epsilon}$ corresponding to $m_{\rm JJ}$ of the event:

$$n^{\epsilon}_{\rm trk}(m_{\rm JJ}) = n_{\rm trk} - P^{\epsilon}(m_{\rm JJ}) \tag{8.5}$$

Thus, a cut on $n^{\epsilon}_{\rm trk}$ which yields a total background efficiency close to the target efficiency $\epsilon$ will have roughly the same efficiency in every $m_{\rm JJ}$ bin and should therefore not distort the background distribution.

The functional dependence of percentile $P^{\epsilon}(m_{\rm JJ})$ on $m_{\rm JJ}$, is determined by fitting the distribution with an error function,

$$y = a \cdot \mathrm{erf}(b \cdot (m_{\rm JJ} + c)) \quad , \quad \mathrm{erf}(x) = \frac{2}{\sqrt{\pi}} \int_0^x \exp^{-t^2} dt \tag{8.6}$$

which was found to give a more accurate description than a first, second, or third order polynomial. A non-parametric method for pattern recognition, called *k*-nearest neighbors (*k*-NN) algorithm [99], was also tested for describing the percentile curve, in order to avoid assumptions on the functional form. However, given the *k*-NN-based definition, the cut on $n^{\epsilon}_{\rm trk}$ yielded a step-wise falling background distribution in the signal region.

The percentiles are calculated from a collection of jets, consisting of the two leading jets in each event, such that $\epsilon$ is a jet efficiency rather than an event efficiency. In this way, the amount of statistics used in the method is doubled, and the leading and sub-leading jets are treated on an equal footing. The $1\%$ single-jet efficiency percentiles, $P^{\epsilon=1\%}(m_{\rm JJ})$, are shown in Figure 8.13 for a random subset of the simulated mulitjet sample corresponding to half of the events. This subset is referred to as the *training* sample, and is used in order to test the effect of the selection on the other half of the sample, called the *testing* sample. The fit only goes up to $m_{\rm JJ} = 6000$ GeV, to get a better description in the region where data is expected. At higher $m_{\rm JJ}$ values, we assume a constant given by the value at $m_{\rm JJ} = 6000$ GeV.

Figure 8.14 shows the single-jet background efficiency given by the cut, $n^{\epsilon}_{\rm trk} > 0$, and the event efficiency given by requiring both the leading and sub-leading jet $n^{\epsilon}_{\rm trk} > 0$. The single jet efficiency is indeed close to $1.0\%$ across the full $m_{\rm JJ}$ range, as expected. The event efficiency is slightly larger than $1\% \times 1\% = 0.01\%$, due to correlations between the two leading jets. The selection efficiency is compared to that of a cut on $n_{\rm trk} > 70$, which has a clear slope.

The $m_{\rm JJ}$ bins in which the percentiles are computed, are defined starting from the high end of the spectrum such that the minimum bin width is 200 GeV, and is increased by 100 GeV

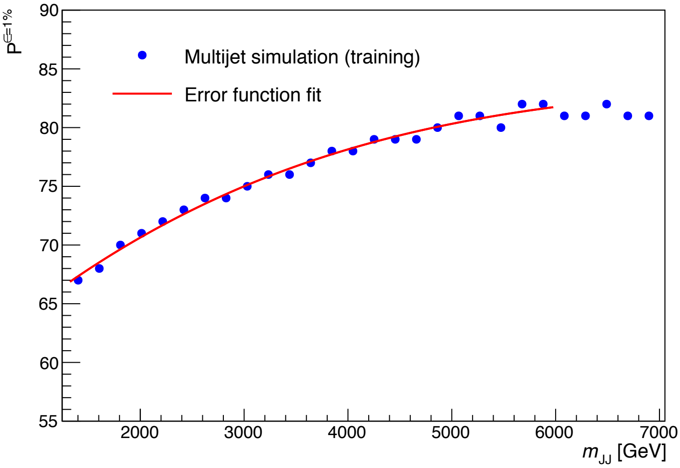

**Figure 8.13:** The cut value on $n_{\text{trk}}$ corresponding to a background efficiency of 1%, $P^{\epsilon=1\%}$ in simulated multijet events. The $P^{\epsilon=1\%}$ values are evaluated in bins of $m_{\text{JJ}}$ (blue dots) and fitted with an error function (red line) to give a continuous prediction across $m_{\text{JJ}}$.

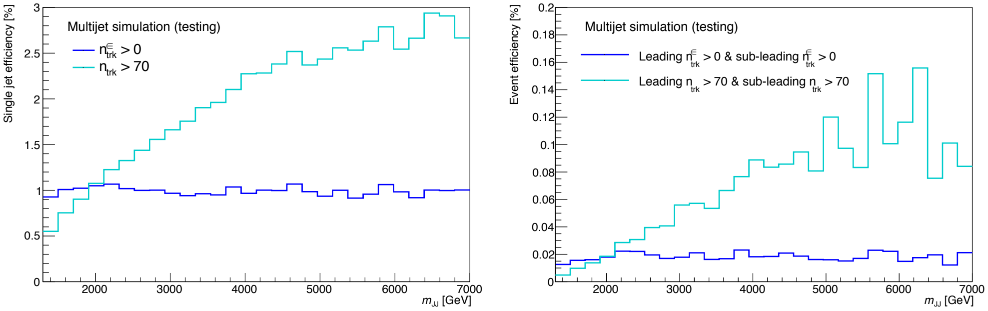

**Figure 8.14:** The single jet background efficiency of a cut on $n_{\text{trk}}$ (teal) and $n^{\epsilon}_{\text{trk}}$ (blue), measured bin-by-bin across the relevant $m_{\text{JJ}}$ range. The efficiency is measured in a subset of the mulitjet background sample which is orthorgonal to that used for defining $n^{\epsilon}_{\text{trk}}$.

until a minimum amount of statistics $n_{\text{min}}$ is present in that bin. The value of $n_{\text{min}}$ was determined by performing the fit for a range of values and seeing where they converge. The resulting background $m_{\text{JJ}}$ distribution following a cut on $n^{\epsilon}_{\text{trk}}$ is shown in Figure 8.15, and compared to the inclusive background distribution. The $m_{\text{JJ}}$ distribution for Model A, $M_{Z'} = 3\,\text{TeV}$, following the cut on $n^{\epsilon}_{\text{trk}}$, is also plotted to show that the cut indeed maintains the peak like signature for signal events.

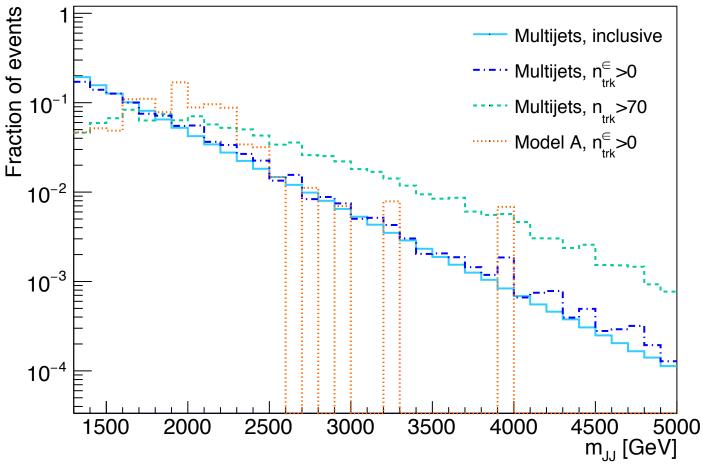

**Figure 8.15:** Shape comparisons of the $m_{\mathrm{JJ}}$ spectrum with different selections applied. In solid, light blue line is shown the inclusive event selection where only the preselection is applied. In dashed green the spectrum is shown after a requirement of $n_{\mathrm{trk}} > 70$. In dashed, dark blue line the spectrum is shown after a requirement of $n^{\epsilon}_{\mathrm{trk}} > 0$. The spectrum is also shown for a signal sample with the model A parameters and a mediator mass of $M_{Z'} = 3\,\mathrm{TeV}$.

### 8.6.3 Choice of $\epsilon$

For the fixed-efficiency regression to work best, the final cut must yield a jet-by-jet selection efficiency corresponding to $\epsilon$ of the percentiles. Therefore, $\epsilon$ is determined in an iterative process:

1. The initial value of $\epsilon$ was set to $0.5\%$ as that is the minimum single-jet efficiency required to yield sufficient background statistics in the SR for fitting.
2. With the variable $n^{\epsilon=0.5\%}_{\mathrm{trk}}$ defined, the sensitivity was studied for each model separately. This showed that a cut above -10 would render the analysis completely insensitive to model B type dark QCD.
3. The final value of $\epsilon$ was then determined as the single jet efficiency corresponding to cut on $n^{\epsilon=0.5\%}_{\mathrm{trk}} > -10$, which was found to be $1\%$.

According to Figure 8.16, the optimal cut would be somewhere around $n^{\epsilon=1\%}_{\mathrm{trk}} = 25$, but a single jet efficiency of $1\%$ is obtained by a cut at $n^{\epsilon=1\%}_{\mathrm{trk}} = 0$. A requirement of $n^{\epsilon}_{\mathrm{trk}} > 0$ is inclusive enough for the search to be sensitive to model B, but still rejects the vast majority of background events. The selection efficiencies of the signal region for simulated signal and multijet background is shown in Table 8.3.

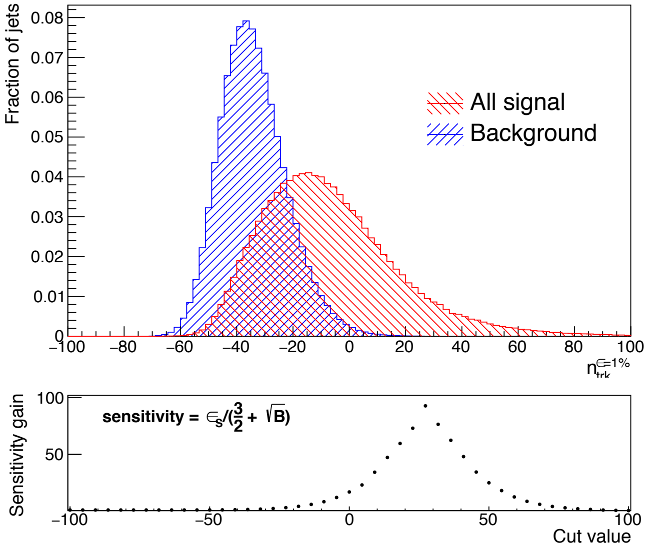

**Figure 8.16:** The top panel shown the distribution of $n^{\epsilon}_{\text{trk}}$ for multijet background in red hashed histogram and for all signal models combined in the blue. The bottom panel shows the sensitivity gain equivalent to a cut corresponding to the $n^{\epsilon}_{\text{trk}}$ value on the x-axis.

### 8.6.4 Data-driven sanity check

The definition of $n^{\epsilon}_{\text{trk}}$ is derived in multijet simulations, although $n_{\text{trk}}$ is known to be poorly modeled due to its sensitivity to non-perturbative processes, such as fragmentation. We saw in Figure 8.7 that the Pythia 8 generator tune used for the multijet simulations, A14, provides a reasonable description of the charged particle multiplicity in the jet. However, the tune parameters were not optimised for the full Run 2 data set and even for Run 1, the description is not perfect. Therefore, some mis-modeling of $n_{\text{trk}}$ is expected in our simulated samples.

Unfortunately, it is not possible to use data to derive the $n^{\epsilon}_{\text{trk}}$ definition, because there is no variable uncorrelated with $n_{\text{trk}}$ with which we can define a data selection that is devoid of potential signal events - a *control region*. In a control region based on $n_{\text{trk}}$ or a correlated variable, the sample is biased towards lower $n_{\text{trk}}$ values. That means the percentile curve changes, and a signal region cut on the resulting $n^{\epsilon}_{\text{trk}}$ would not necessarily give a fixed efficiency. Although we can not use a control region data sample to derive the final $n^{\epsilon}_{\text{trk}}$ cut variable, we can use such a region to test the effect of the potential mis-modeling of $n_{\text{trk}}$. By deriving the $n^{\epsilon}_{\text{trk}}$ in a simulated control region sample, we can check that the corresponding cut also gives a flat efficiency in the control region data sample.

We define an control region with negligible signal contamination, by requiring that at least one of the two leading jets satisfy $n_{\mathrm{trk}} < 20$. This selection has an efficiency of $\sim 0.5\%$ on the tested signal models. If only one of the two leading jets, satisfies the cut, the other is stored in a low-signal sample of jets. If both jets satisfy the cut, a random choice is made between the two jets. We will refer to this as the initial control region (CR1), because a different control region will be defined later. By deriving a definition of $n^{\epsilon}_{\mathrm{trk}}$ from CR1 of simulation, we can test the efficiency of the signal region criterion on a corresponding data sample.

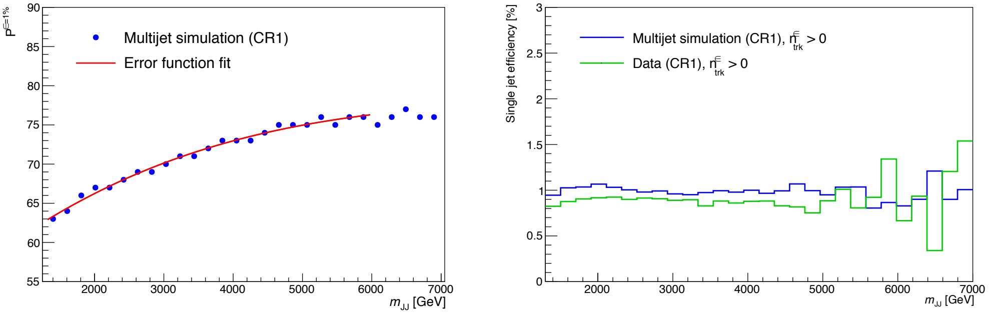

(a) (b)

**Figure 8.17:** Validation of the fixed-efficiency method. On the left is shown the $\epsilon = 1\%$ percentiles computed in the initial control region (CR1) of the simulated multijet sample. On the right is shown the selection efficiency of a cut $n^{\epsilon}_{\mathrm{trk}} > 0$, where $n^{\epsilon}_{\mathrm{trk}}$ is defined from the percentiles on the left.

Figure 8.17 shows the percentiles $P^{\epsilon=1\%}$ computed from the control sample of simulated jets along with the selection efficiencies of a cut on the corresponding $n^{\epsilon}_{\mathrm{trk}}$ in both data and simulated CR1. The efficiency is close to $1\%$ across the $m_{\mathrm{JJ}}$ spectrum in both cases. The efficiency in data is slightly lower than for simulation, but with a roughly constant offset. Hereby, we are more confident that a cut on $n^{\epsilon}_{\mathrm{trk}} > 0$ should have a flat efficiency in data, even though it is derived from simulated events.

## 8.7 Background estimation

Following the event selection described above, the remaining background events are expected to form a smoothly falling $m_{\mathrm{JJ}}$ spectrum, atop which we can look for the mass peak of a narrow resonance. The background is estimated empirically by fitting the observed $m_{\mathrm{JJ}}$ spectrum in the signal region using a binned-likelihood fit of the parameterised form:

$$\frac{\mathrm{d}N}{\mathrm{d}x} = p_1(1-x)^{p_2+\zeta p_3} x^{p_3}, \quad x = \frac{m_{\mathrm{JJ}}}{\sqrt{s}} \tag{8.7}$$

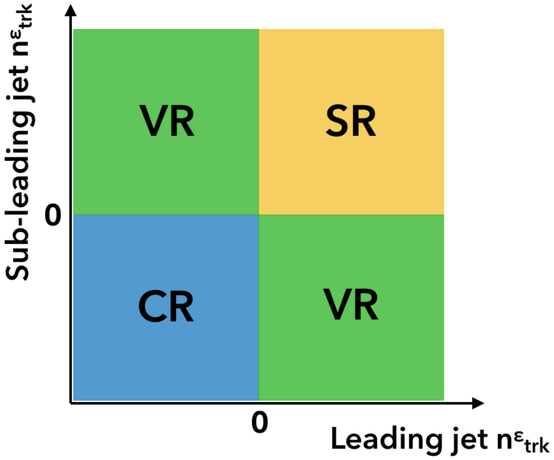

**Figure 8.18:** The signal region (SR), control region (CR) and validation regions (VR) defined by the main discriminating variable $n^{\epsilon}_{\mathrm{trk}}$.

where $p_1$ is a normalisation factor, $p_2$ and $p_3$ are dimensionless shape parameters, and $\zeta$ is a constant chosen to minimise the correlation between $p_2$ and $p_3$.

To establish and test the background estimation, we use simulated multijet samples and as well as data from regions where we expect low signal contamination. The data set is divided into four regions, as illustrated in Figure 8.18, where the two validation regions are combined as one selection.

The control region (CR) is defined by requiring that both leading jets have $n^{\epsilon}_{\mathrm{trk}} < 0$, such that the relative signal contribution is expected to be negligible. Therefore, this region is used to define the background template. The intermediate validation region (VR), where exactly one jet is required to have $n^{\epsilon}_{\mathrm{trk}} > 0$, is used to check the background template and potentially assign an uncertainty if a difference seen. The selection efficiencies of each region for simulated signal and multijet background samples are listed in Table 8.3, where signal refers to all models and mass points combined.

**Table 8.3:** Table listing the selection efficiencies of each data region for the multijet background and for all signal models combined.

| | Signal Region [%] | Validation Region [%] | Control Region [%] |
|---|---|---|---|
| Background | 0.0129 | 1.71 | 98.3 |
| Signal | 19.1 | 34.8 | 46.1 |

In Figure 8.19 the $m_{\mathrm{JJ}}$ spectrum shape in the various regions are compared to the inclusive

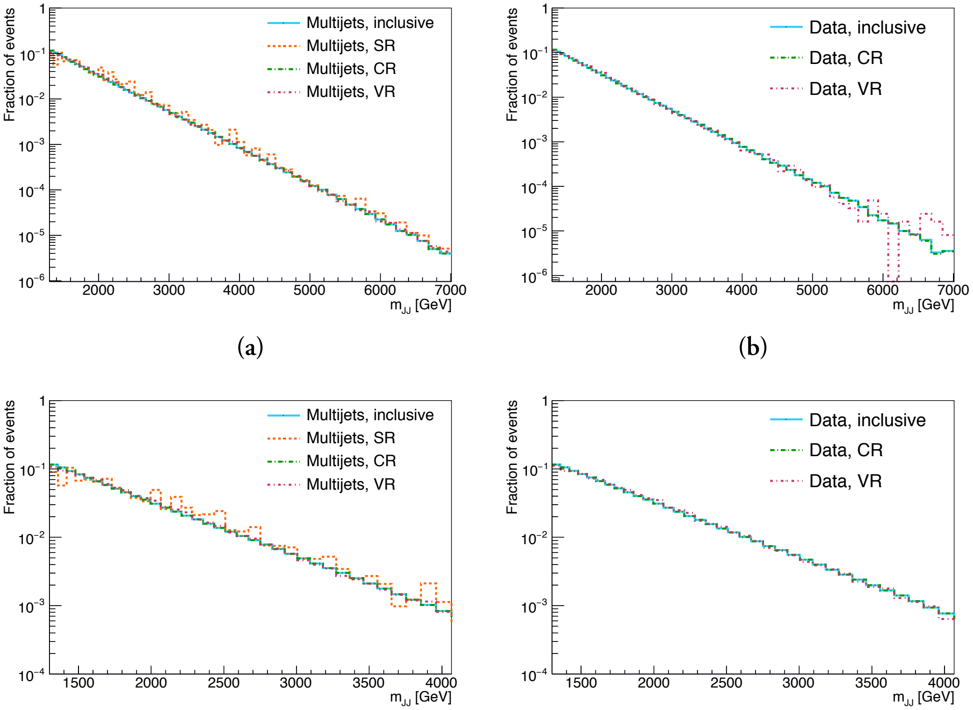

(a) (b)

(c) (d)

**Figure 8.19:** Shape comparisons of the dijet invariant mass spectrum in the various event selections. The comparison in shown for multijet simulations in the left hand plots and data in the right hand plots. The upper plots show the full spectrum, and the lower plots are zoomed in on the high-statistics region. Comparisons are made between the inclusive sample, the control region (CR), and the validation (VR) for both data and simulation. The signal region(SR) is only shown for simulation.

sample for both data and multijet simulation. The validation region and control region look to agree well with each other in both cases. The signal region is only shown for simulated data, but also shows decent overall agreement. A small bias is, however, observed at low $m_{\text{JJ}}$, which means we may have to see if we can improve the percentile fit for the derivation of the cut variable $n_{\text{trk}}^{\epsilon}$.

Since the analysis is not unblinded at the time of writing, the result of the background estimation in the signal region can not be presented here. Instead, I review the tests that we have either performed already or are planning to perform, and which conclusion we have or may draw from them.

### 8.7.1 Resolution-based $m_{\mathrm{JJ}}$ binning

The binning of the $m_{\mathrm{JJ}}$ distribution is chosen to approximate the relative detector mass resolution, which is defined as the standard deviation of the response divided by the response. The detector response is measured in a simulated multijet sample corresponding to the 2017 data taking conditions. The procedure of determining the bins sizes follow multiple steps:

1. The sample is divided into slices of the true dijet mass $m_{\mathrm{JJ}}^{\mathrm{truth}}$, where the width of the slices are determined by Scott's normal reference rule [100]. In each slice, a histogram is filled with $m_{\mathrm{JJ}}$ responses, defined as $m_{\mathrm{JJ}}^{\mathrm{reco}}/m_{\mathrm{JJ}}^{\mathrm{truth}}$ and computed for every jet.
2. A Gaussian function is fitted to each response histogram and the relative resolution defined as the width over the mean $\sigma_R/\mu_R$, which directly translates to the relative $m_{\mathrm{JJ}}$ resolution $\sigma_{m_{\mathrm{JJ}}}/m_{\mathrm{JJ}}$.
3. Similarly to the relative energy resolution of a typical calorimeter, the $m_{\mathrm{JJ}}$ resolution can be parameterised as:

   $$F(m_{\mathrm{JJ}}) = \frac{\sigma_{m_{\mathrm{JJ}}}}{m_{\mathrm{JJ}}} = a\frac{1}{m_{\mathrm{JJ}}} + b\frac{1}{\sqrt{m_{\mathrm{JJ}}}} + c \tag{8.8}$$

   This function is fitted to the computed resolutions.
4. Starting from the lowest bin edge $b_0$, the next bin edge $b_i$ is obtained as

   $$b_i = b_{i-1} + F(b_{i-1}) \cdot_{i-1} + 1 \tag{8.9}$$

   where the second is rounded down to obtain integer bin edges.

As a result, the binning of $m_{\mathrm{JJ}}$ distribution is determined to be:

$$\begin{aligned}[&1300, 1359, 1419, 1479, 1540, 1602, 1665, 1729, 1794, 1860, 1927, 1996,\\ &2066, 2137, 2209, 2282, 2357, 2433, 2510, 2589, 2669, 2751, 2834, 2919,\\ &3005, 3093, 3182, 3273, 3366, 3460, 3556, 3654, 3754, 3856, 3960, 4066,\\ &4174, 4284, 4396, 4510, 4627, 4746, 4867, 4991, 5117, 5246, 5377, 5511,\\ &5648, 5787, 5929, 6074, 6222, 6373, 6527, 6685, 6846, 7010]\end{aligned}$$

### 8.7.2 Wilk's likelihood-ratio test

To determine whether the number of free parameters of the function in Equation 8.7 is optimal for the expected number of events, a Wilk's likelihood-ratio test is performed [101].

For a Wilk's test, several pseudo-data sets are generated from the simulated background sample and fitted with a function of higher complexity than the nominal. From these fits several new pseudo-data sets are created and fitted with the two functions that are being compared. For each set of pseudo-data, the minimised log-likelihood is computed for the nominal fit $L_0$ and the higher-complexity fit $L_1$. The Wilk's test statistics is then given by $\Lambda = -2\log(L_0/L_1)$, and the mean $\mu_\Lambda$ of all pseudo-experiments is used to determine if higher complexity is necessary. If the probability of $\mu_\Lambda$ is higher than 0.05 the nominal function is sufficiently complex, and can then be compared to one of lower complexity.

### 8.7.3 Signal injection test

Once the fit function is settled to be suitable for fitting the background distribution alone, we check the performance in the case where both signal and background events are present. The idea of a signal injection test is to take a simulated background sample with a known amount of simulated signal events injected, and fit it with a background-only fit function. If a local excess, corresponding to the injected signal, is observed, the function is performing well. If a smaller or no excess is observed, the function is likely to be too flexible for the signal shape, and is therefore absorbing the signal in the background estimate.

Our signal injection tests, showed that the signal shapes expected for the tested benchmark models would be too wide compared to the flexibility of the fit function. This can be seen in Figure 8.20, where the background template obtained from the pure simulated multijet sample is compared to one where signal is injected in the sample.

Figure 8.20 shows that the background template derived from the signal injected sample, corresponds well to the pseudo-data, meaning that the background fit is accommodation to the signal events present in the pseudo-data. Based on this result, we have chosen to fix the shape parameters of the background template in the data control region. This method requires that the background shape is very similar in the signal and control regions.

### 8.7.4 Spurious signal test

Spurious signal tests are performed to estimate the fit bias, and check the smoothness of the expected background distribution. A sample of background pseudo-data is fitted with a signal-plus-background function. If a deviation from the background-only expectation is observe, a "spurious signal", this is taken as the modeling bias.

A spurious signal test with a previous event selection, where the k-nearest-neighbor (*k*-NN) method method was used in the definition of $n^{\epsilon}_{\mathrm{trk}}$, revealed that the non-parametric fit lead to a staircase type of structure in the $m_{\mathrm{JJ}}$ spectrum of the signal region. This struc-

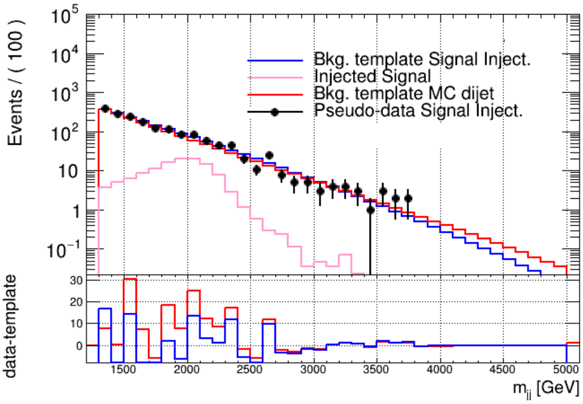

**Figure 8.20:** Dijet mass spectrum of pseudo data (black points) generated from multijet simulations with signal events injected. The psuedodata is compared to the background template taken made from a background-only sample, and the background template obtained with the signal injected sample. The injected signal is generated with Model A parameters and a mediator mass of $M_{Z'} = 2.5$ TeV. The plot is produced by Dilia Portillo and Nathan Lalloue.

ture introduced large spurious signals at certain mass points, which lead us to redefine the discriminating $n^{\epsilon}_{\mathrm{trk}}$ variable using functional fit instead.

Spurious signal test have not yet been performed on the current event selection, but the background distributions is smoother than with the *k*-NN-based $n^{\epsilon}_{\mathrm{trk}}$ cut. In case a significant bias is observed, this will be assigned as an uncertainty on the background estimate.

## 8.8 Systematic uncertainties

At the time of writing, most systematic uncertainties have not been evaluated yet. In this section I describe the uncertainties expected to be most relevant and how we plan to quantify them.

### 8.8.1 Background uncertainties

The statistical uncertainty on the background estimate will be taken directly from the uncertainties on the parameters of the SR background fit. Additional systematic uncertainties may be assigned on the basis of the spurious signal test, discussed under background validation, and from potential differences between the $m_{\mathrm{JJ}}$ spectrum shape in the control region and validation region.

### 8.8.2 Signal uncertainties

#### 8.8.2.1 Jet energy scale and resolution

The uncertainty on the jet energy scale (JES) is an important effect in the search for resonant structures over rapidly falling background spectra. Variations in the JES can shift the expected the mass peak peak of a signal resonance, thereby affecting the potential significance of an excess.

The individual components of the JES uncertainty are evaluated by the *in situ* analyses and propagated to the final JES calibration via the *in situ* combination, as described in Chapter 5. A breakdown of the JES uncertainties was shown in Figure 5.13.

Uncertainties on the measurement of the jet energy resolution (JER) can lead to a mismeasurement of the width of any observed signal and affect the signal selection efficiency. The JER uncertainty is fixed to 2% per jet by the jet performance group in ATLAS. The impact of the uncertainty on the final analysis will be evaluated event-by-event by rerunning the analysis with a corresponding Gaussian smearing applied to the jets $p_{\mathrm{T}}$. Thereby, the nominal resolution will be degraded by the systematic uncertainty value. The changes to the overall signal yield and mass peak can then be assigned as the up-variations, while the down variation is then taken as the mirrored difference between the nominal and up variations.

#### 8.8.2.2 Theoretical uncertainties

The track multiplicity $n_{\mathrm{trk}}$ of the dark jets might be very sensitive to theoretical uncertainties and tuning parameters of the event generation. Variations in the number of tracks could significantly impact the signal efficiency of the $n_{\mathrm{trk}}^{\epsilon}$ event selection. However, the uncertainty on $n_{\mathrm{trk}}$ of dark jets can not be estimated from data, as we have no known dark jet events. At the same time, we can not evaluate the uncertainty by varying our choice of Monte Carlo generator either, since no other generator than PYTHIA 8 exists for hidden sector simulation. It has been discussed to vary the renormalisation scale in the signal generation, but the appropriate size of such a variation is not well-defined.

#### 8.8.2.3 Luminosity scale

The uncertainty in the combined 2015–2018 integrated luminosity is 1.7 % [102], obtained using the LUCID-2 detector [103] for the primary luminosity measurements.

## 8.9 Outlook

The analysis presented in this chapter is the first attempt at a search for dark QCD jets using jet characteristics and substructure variables. We have demonstrated the feasibility of such a search while keeping the analysis as simple as possible. This means that there is plenty of room for improving the sensitivity to the benchmark models, and for broadening the analysis to more sets of dark QCD parameters. In this section I discuss the potential improvements which could be considered for a future iteration of this search.

### 8.9.1 Jet reconstruction

The jet collection, trimmed anti-$kt$ $R = 1.0$ LCTopo jets, was chosen because it is the one for which the full large-$R$ jet calibration is derived. However, potential benefits of other jet definitions have been studied for the sake of future iterations of this analysis. The motivation for investigating other jet types, is the observation that for all models and mass points, the distribution of reconstructed dijet mass $m_{\mathrm{JJ}}$ peaks at a significantly lower value than the simulated resonance mass $M_{Z'}$. This is a disadvantage for the sensitivity of the search, since the background levels are generally higher at lower $m_{\mathrm{JJ}}$ values.

The effect is illustrated in Figure 8.21, which shows the relative difference between the mean of the reconstructed $m_{\mathrm{JJ}}$ and the resonance mass for all models and mass points.

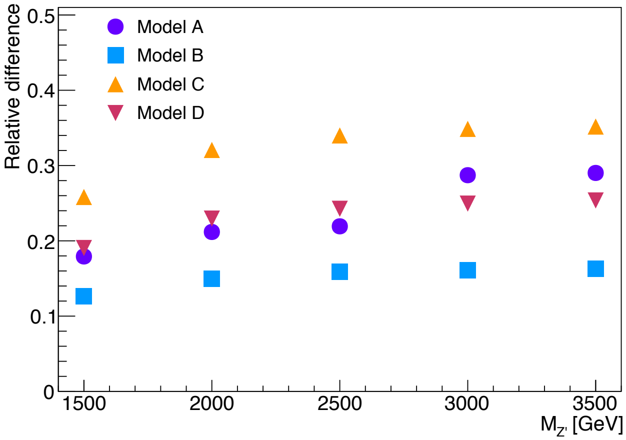

**Figure 8.21:** Relative difference between reconstructed invariant dijet mass $m_{\mathrm{JJ}}$ and the simulated resonance mass as function of the resonance mass for all four benchmark models.

The shift of the peak can not be explained by invisible particles carrying away energy and thereby reducing the reconstructed $m_{\mathrm{JJ}}$. The generated signal samples do not contain stable dark hadrons and the fraction of missing transverse momentum related to neutrinos is very small. However, the dark photons in models C and D do have a significant branching ratio to muons, as was seen in Table 8.2. Muons leave only a small fraction of their energy in the calorimeters, and therefore do not contribute much to the $m_{\mathrm{JJ}}$ reconstruction. This would explain why the effect is largest for model C, where the distribution of reconstructed $m_{\mathrm{JJ}}$ peaks 25% to 35% below the resonance mass. However, muons can not be the full explanation, since a mass difference is also seen in Model A and B, where there are no muons in the decay channel.

Indeed several effects related to the jet definition seem to be at play. To avoid running the full reconstruction and calibration on a number of jet definitions, we study these effects at "truth-level". That means the jet four-momentum is reconstructed from the truth-information on individual particles available in the simulation output. These signal samples are filtered at the generator level to have at least one anti-$k_t$ jet with $p_{\mathrm{T}} > 300\,\mathrm{GeV}$ and $|\eta| < 2.7$. The following studies are made with the further requirements that there are two jets with $p_{\mathrm{T}} > 100\,\mathrm{GeV}$ and $|\eta| < 2.5$. The invariant mass is constructed from the two leading jets.

Figure 8.22 shows the effect of including muons in the dijet mass calculation. The nominal $m_{\mathrm{JJ}}$ distribution, constructed without muons, is compared to the one obtained by adding the muons four momenta in the calculation. The comparison is shown for each of the four models with a mediator mass $M_{Z'} = 1000\,\mathrm{GeV}$. In the cases of model C and D, the addition of muons recovers some of the energy, bringing the peak closer to the resonance mass. This indicates, that a lepton-jet analysis could be more sensitive specifically to dark QCD models with a large muon fraction in the shower. Figure 8.22 also shows that the muons have no impact on model A and B as expected.

Energy is also removed from the jet by the trimming procedure, described in Chapter 5. The effect of trimming for each model can be seen in Figure 8.23, where the dijet mass for the nominal jet reconstruction is compared to that obtained without applying trimming. The peak of the trimmed jets is shifted downwards in $m_{\mathrm{JJ}}$, suggesting that a large fraction of the jet energy is deposited in soft components which are removed by the trimming procedure. A downwards shift reduces the expected signal-over-background ratio, since the background is larger at lower $m_{\mathrm{JJ}}$ values. Trimming also seems to make the peak wider, thereby decreasing the sensitivity further.

Figure 8.23 also shows the dijet mass distribution where the jets are untrimmed and muons are included in the $m_{\mathrm{JJ}}$ calculation. It can be seen that, in this case, the dijet invariant mass of model B jets peaks nicely around the mediator mass of $M_{Z'} = 1000\,\mathrm{GeV}$, while the three other models remain slightly offset.

The remaining offset could be related to the different strong coupling and decay modes of the models, where the settings of model B gives the most narrow jets: If the jets are not fully

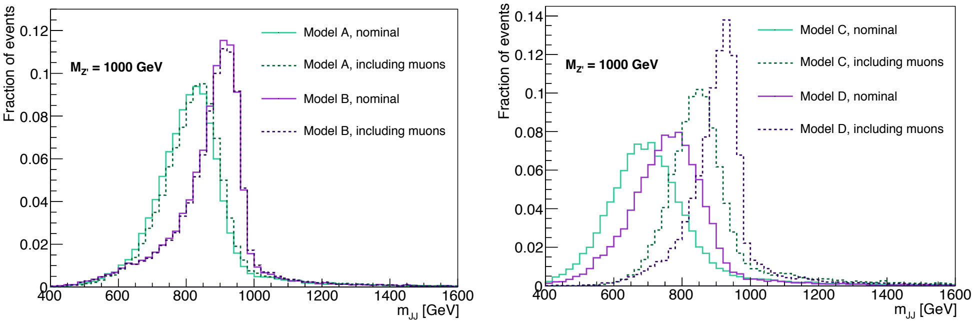

(a) (b)

**Figure 8.22:** Dijet invariant mass distribution, as computed from the nominal jet definition (solid lines) and by including muons (dashed lines). The distributions are shown for Model A and B in (a) and Model C and D in (b). A large effect is observed for Model B and C, where a significant muon component is expected from the dark meson decays.

contained by in $R = 1.0$ jets, all energy is not accounted for. This seems to be the case for model A. Figure 8.24 shows the $m_{\mathrm{JJ}}$ distribution, where the jets are reconstructed using the anti-$k_t$ algorithm with different radius parameters. For untrimmed jets, the peak moves towards larger $m_{\mathrm{JJ}}$ as the radius grows, and it is best defined with $R = 1.2$. However, for trimmed jets, increasing the radius beyond $R = 1.0$ has no effect.

These studies imply that not only might the nominal pile-up mitigation technique of large-$R$ jets be sub-optimal for our signal models but also the standard large-$R$ jet reconstruction. However, some type of pile-up mitigation is necessary - not having any would be even worse for the resolution when looking in real data.

An alternative jet definition is to build large-$R$ jets by reclustering small-$R$ jets which have a different pile-up subtraction applied (see Chapter 5), so no trimming needs to be applied. Where the trimming algorithm was designed, to also improve tagging efficiency of jets with prong-like substructure, the pile-up subtraction method targets pile-up contributions more directly. This may be better suited for the present search, since we can not use two- or three-prong taggers to select dark jets. Another advantage is that the centrally-derived calibration and uncertainties for anti-$k_t R = 0.4$ jets can be propagated to the reclustered (RC) jets, while the jet radius can be optimised for the considered signal models.

The effect of using RC jets with $R = 1.0$ and $R = 1.2$ can be seen for model A with $M_{Z'} = 1000\,\mathrm{GeV}$ in Figure 8.25. A similar shift of the peak towards the mediator mass is observed for mediator masses of 1.5, 2.0 and 2.5 TeV. At the same time, the width of the peak is reduced to about 2/3 of the on obtained with standard large-$R$ trimmed jets.

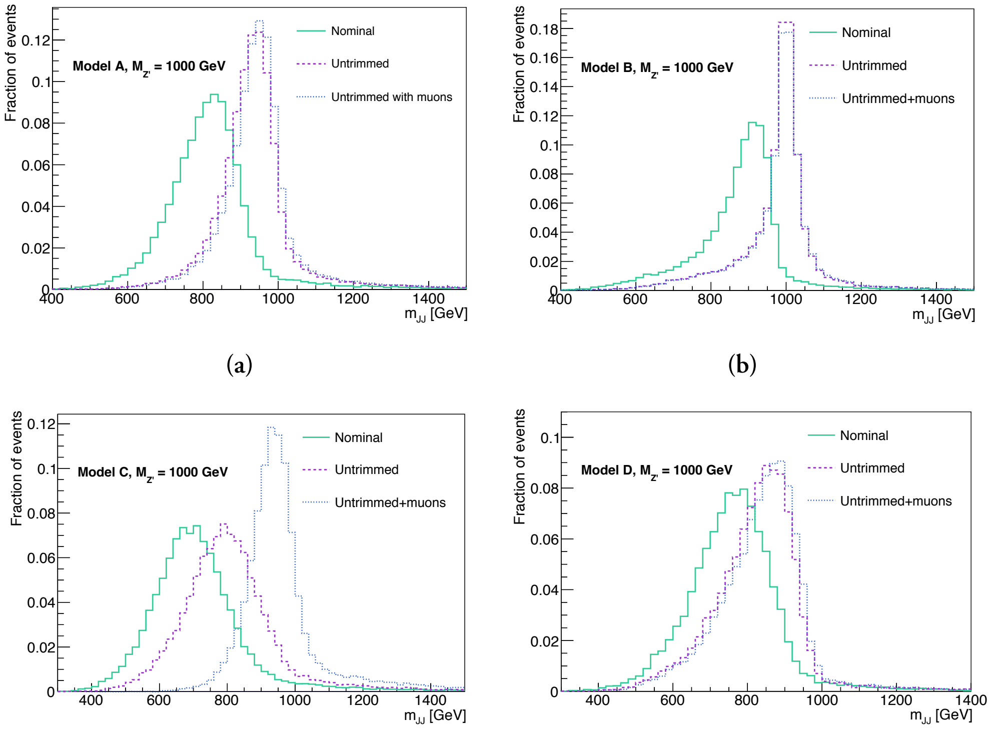

(a)

(b)

(c)

(d)

**Figure 8.23:** Dijet invariant mass distribution of signal jets, as computed from the nominal jet definition (solid lines), from the untrimmed jets (dashed lines), and from untrimmed jets with muons included (dotted lines).

Further improvements may be achieved in a future iterations of a dark jet search by using UFO jets (described in Chapter 5) for which precision calibrations are currently being derived. These are expected to be the baseline recommendation for all searches with large-$R$ jets.

### 8.9.2 Multivariate analysis

The best performing variables for discriminating between dark jets and QCD jets, are generally correlated with $n_{\mathrm{trk}}$. Therefore, we do not expect that combining these would lead to a big improvement in the sensitivity for any of the four tested benchmark models. But given the various possible signatures of dark QCD jets, it might be possible to gain broader sensitivity to all possible models by combining several jet substructure variables in a multivariate classification scheme.

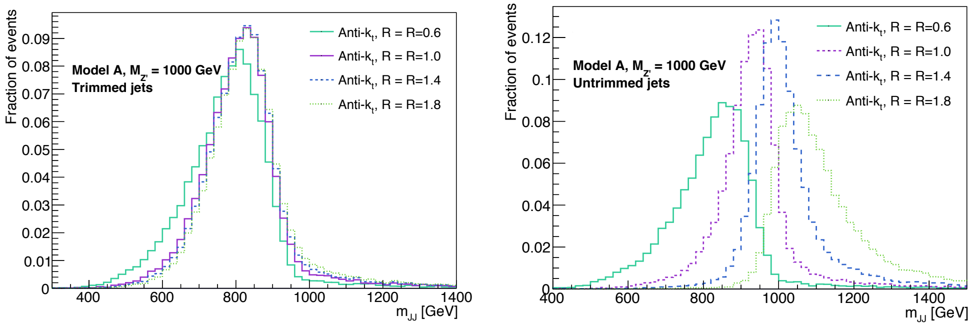

(a)

(b)

**Figure 8.24:** Dijet invariant mass distribution of signal jets, computed from jets reconstructed with various radius parameters in the anti-$k_t$ algorithm. The effect is shown for trimmed jets in (a) and for untrimmed jets in (b).

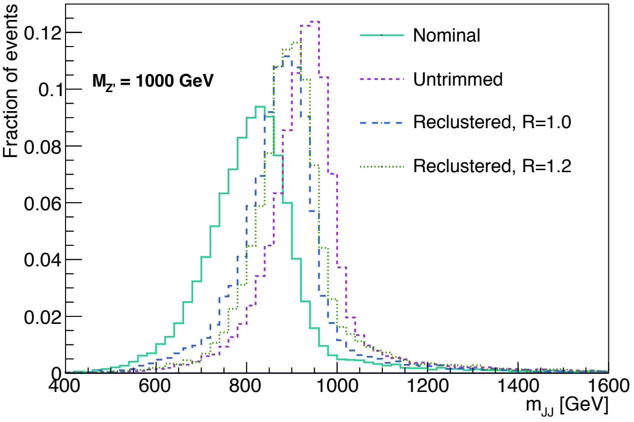

**Figure 8.25:** Dijet invariant mass distribution of signal jets, comparing the nominal jet definition (teal, solid line) to untrimmed jets (purple, dashed line), and reclustered jets with radius $R = 1.0$ (blue dashed line) or $R = 1.2$ (green, dotted line).

In the paper where the benchmark models were proposed [44], the authors show that a Boosted Decision Tree with three variable, can improve the discrimination. By training the BDT on the four benchmark models, A, B, C, and D and testing them on two new ones, E and F, the authors find that this approach can be applied to cover a wide range of parameters in dark QCD physics.

An event selection based on a BDT score built from several substructure variables, is also likely to shape the $m_{JJ}$ distribution, similarly to what we have seen for a flat cut on the track multiplicity. This effect makes background fitting less feasible. Therefore, it is worth considering to use instead an adversarial neural network (ANN), which can be build to avoid background shaping. The ANN method was tested along with the fixed-efficiency regression for $W$-boson tagging in [98], and was found to result in the best discrimination and least correlation of the all the tested methods.

# Chapter 9

# Concluding Remarks

This thesis has presented two searches for new physics phenomena beyond the Standard Model which use events with either small- or large-radius jets in the final state. The calibration chain of both types of jets has also been described in detail. The analyzed data from LHC $pp$ collisions was collected with the ATLAS detector between 2015 and 2018.

Jets are important signatures at hadron colliders for probing new physics as well precision measurements, and accurate calibrations of jets are therefore crucial for the ATLAS physics program. Using *in situ* calibration methods, the detector response to jets was measured directly in data to correct for potential discrepancies between data and simulation. The methodology was originally developed for the small-$R$ jet $p_{\mathrm{T}}$ calibration, but it was adapted and implemented in the large-$R$ jet $p_{\mathrm{T}}$ and mass calibration during Run 2. This *in situ* calibration led to significantly reduced uncertainties in the reconstructed large-$R$ jet $p_{\mathrm{T}}$ and mass, thereby increasing the sensitivity of ATLAS searches and measurements using large-$R$ jets.

An alternative procedure for combining *in situ* measurements was also presented. By basing the combination on a polynomial fit rather than interpolating splines, the final calibration curve became less sensitive to local fluctuations, which turned out to be an advantage for searches with very small statistical uncertainties, such as the Dijet Trigger Level Analysis.

The presented search for a pair-produced coloured resonance decaying to four jets was conducted with $37\,\mathrm{fb}^{-1}$ of data collected during 2015 and 2016. A counting experiment was performed in bins of the average mass of the two resonance candidates using two different event selections; one inclusive and one with two $b$-tagged jets. No significant deviation from the Standard Model prediction was observed. The result of the $b$-tagged selection was interpreted in a SUSY simplified model, where the stop squark is the lightest supersymmetric particle. It is pair-produced and decays promptly to a $b$-quark and a light quark through *R*-parity violating couplings.

Masses of such a stop squark were excluded in the range 100 GeV $< m_{\tilde{t}} <$ 470 GeV and 480 GeV $< m_{\tilde{t}} <$ 610 GeV at 95% CL. The results of the inclusive selection were interpreted a similar SUSY model where the stop squark decays to any two quarks. Stop squark masses between 100 GeV and 410 GeV were excluded at 95% CL. Limits were also set on pair-produced scalar gluons decaying to two gluons and pair-produced colorons coupling only to light quarks. The masses of these were excluded up to 800 GeV and 1500 GeV, respectively.

At the time of writing, the search for a heavy resonance decaying to two jets with distinct substructure, has not been finalised. The analysis has been designed to target confined hidden sector models where the mediator decays to two dark quarks which shower and hadronise according to the confinement scale of the hidden sector. The resulting dark mesons decay promptly to Standard Model particles, forming a pair of visible jets. An event selection has been developed to target dark jets based on the number of tracks associated with the jet. The event selection uses the novel technique of Fixed-Efficiency Regression, to ensure that the selection does not distort the background distribution. This technique has not been used in an ATLAS analysis before, but could be relevant for many searches that apply a jet substructure-based selection, since the substructure variables often are correlated with mass. The Standard Model background of the search will be estimated directly from data in the signal region. The estimation method is currently being validated in other regions of data and in Monte Carlo simulations.

# References

[1] Stephen P. Martin. A Supersymmetry Primer. *Advanced Series on Directions in High Energy Physics*, 1998. ISSN 1793-1339. doi: 10.1142/9789812839657_0001. URL http://dx.doi.org/10.1142/9789812839657_0001.

[2] Matthew J. Strassler and Kathryn M. Zurek. Echoes of a hidden valley at hadron colliders. *Physics Letters B*, 651(5-6), Aug 2007. ISSN 0370-2693. doi: 10.1016/j.physletb.2007.06.055. URL http://dx.doi.org/10.1016/j.physletb.2007.06.055.

[3] Rober Oerter. *The theory of almost everything: The Standard Model, the unsung triumph of modern physics.* Pi Press, 2006.

[4] Cliff Burgess and Guy Moore. *The Standard Model: A Primer*. Cambridge University Press, 2006.

[5] M. Tanabashi et al. Review of particle physics. *Phys. Rev. D*, 98:030001, 2018. doi: 10.1103/PhysRevD.98.030001. URL https://link.aps.org/doi/10.1103/PhysRevD.98.030001.

[6] Carsten Burgard. The standard model of particle physics, 2016. URL https://texample.net/tikz/examples/model-physics/.

[7] A. Einstein. Über einen die Erzeugung und Verwandlung des Lichtes betreffenden heuristischen Gesichtsppunkt. *Annalen der Physik*, 322(6):132–148, 1905. doi: 10.1002/andp.19053220607. URL https://onlinelibrary.wiley.com/doi/abs/10.1002/andp.19053220607.

[8] A. Einstein. Zur Elektrodynamik bewegter Körper. *Annalen der Physik*, 322(10): 891–921, 1905. doi: 10.1002/andp.19053221004. URL https://onlinelibrary.wiley.com/doi/abs/10.1002/andp.19053221004.

[9] A. Einstein. Ist die Trägeint eines Körpers von seinem Energieinhalt abhängig? *Annalen der Physik*, 323(13):639–641, 1905. doi: 10.1002/andp.19053231314. URL https://onlinelibrary.wiley.com/doi/abs/10.1002/andp.19053231314.

[10] P. Dirac. The Quantum Theory of the Emission and Absorption of Radiation. *Proceedings of the Royal Society of London Series A*, 114(767):243–265, 1927. doi: 10.1098/rspa.1927.0039.

[11] E.Fermi. Versuch einer Theorie der $\beta$-Strahlen, I. *Zeitschrift für Physik*, 1934. URL `https://doi.org/10.1007/BF01351864`.

[12] S. Glashow. The renormalizability of vector meson interactions. *Nucl. Phys.*, 10, 1959.

[13] A. Salam. Weak and electromagnetic interactions. *Nuovo Cimento*, 11, 1959. URL `https://doi.org/10.1007/BF02726525`.

[14] Steven Weinberg. A Model of Leptons. Phys. Rev. Lett., 19(21):1264–1266, November 1967. doi: 10.1103/PhysRevLett.19.1264.

[15] Michael Riordan. *The Hunting of the Quark: A True Story of Modern Physics*. Simon & Schuster, 1987.

[16] Particle Data Group. Review of Particle Physics. *Progress of Theoretical and Experimental Physics*, 2020(8), 08 2020. URL `https://pdg.lbl.gov/2020/reviews/rpp2020-rev-qcd.pdf`.

[17] F. Englert and R. Brout. Broken symmetry and the mass of gauge vector mesons. *Phys. Rev. Lett.*, 13:321–323, Aug 1964. doi: 10.1103/PhysRevLett.13.321. URL `https://link.aps.org/doi/10.1103/PhysRevLett.13.321`.

[18] Peter W. Higgs. Broken symmetries and the masses of gauge bosons. *Phys. Rev. Lett.*, 13:508–509, Oct 1964. doi: 10.1103/PhysRevLett.13.508. URL `https://link.aps.org/doi/10.1103/PhysRevLett.13.508`.

[19] CMS Collaboration. A measurement of the higgs boson mass in the diphoton decay channel. *Physics Letters B*, 805:135425, 2020. ISSN 0370-2693. doi: 10.1016/j.physletb.2020.135425. URL `http://dx.doi.org/10.1016/j.physletb.2020.135425`.

[20] J. Rojo V. Bertone, S. Carrazza. APFEL Web. URL `https://apfel.mi.infn.it/`.

[21] A.D. Martin, W.J. Stirling, R.S. Thorne, and G. Watt. Parton distributions for the LHC. *Eur. Phys. J. C*, 63:189–285, 2009. doi: 10.1140/epjc/s10052-009-1072-5.

[22] G. Altarelli and G. Parisi. Asymptotic freedom in parton language. *Nuclear Physics B*, 126(2):298 – 318, 1977. ISSN 0550-3213. doi: https://doi.org/10.1016/0550-3213(77)90384-4. URL `http://www.sciencedirect.com/science/article/pii/0550321377903844`.

[23] B. Andersson, G. Gustafson, G. Ingelman, and T. Sjöstrand. Parton fragmentation and string dynamics. Phys. Rep., 97(2-3):31–145, July 1983. doi: 10.1016/0370-1573(83)90080-7.

[24] B.R. Webber. A qcd model for jet fragmentation including soft gluon interference. *Nuclear Physics B*, 238(3):492 – 528, 1984. ISSN 0550-3213. doi: https://doi.org/10.1016/0550-3213(84)90333-X. URL http://www.sciencedirect.com/science/article/pii/055032138490333X.

[25] Torbjorn Sjotrand, Stephen Mrenna, and Peter Skands. A brief introduction to PYTHIA 8. *Computer Physics Communications*, 178(11), 2008. ISSN 0010-4655. doi: 10.1016/j.cpc.2008.01.036. URL http://dx.doi.org/10.1016/j.cpc.2008.01.036.

[26] Gennaro Corcella, Ian G Knowles, Giuseppe Marchesini, Stefano Moretti, Kosuke Odagiri, Peter Richardson, Michael H Seymour, and Bryan R Webber. Herwig 6: an event generator for hadron emission reactions with interfering gluons (including supersymmetric processes). *Journal of High Energy Physics*, 2001(01), Jan 2001. ISSN 1029-8479. doi: 10.1088/1126-6708/2001/01/010. URL http://dx.doi.org/10.1088/1126-6708/2001/01/010.

[27] Enrico Bothmann, Gurpreet Singh Chahal, Stefan HÂche, Johannes Krause, Frank Krauss, Silvan Kuttimalai, Sebastian Liebschner, Davide Napoletano, Marek SchÂnherr, Holger Schulz, and et al. Event generation with sherpa 2.2. *SciPost Physics*, 7(3), Sep 2019. ISSN 2542-4653. doi: 10.21468/scipostphys.7.3.034. URL http://dx.doi.org/10.21468/SciPostPhys.7.3.034.

[28] J. Alwall, R. Frederix, S. Frixione, V. Hirschi, F. Maltoni, O. Mattelaer, H.-S. Shao, T. Stelzer, P. Torrielli, and M. Zaro. The automated computation of tree-level and next-to-leading order differential cross sections, and their matching to parton shower simulations. *Journal of High Energy Physics*, 2014(7), Jul 2014. ISSN 1029-8479. doi: 10.1007/jhep07(2014)079. URL http://dx.doi.org/10.1007/JHEP07(2014)079.

[29] Simone Alioli, Paolo Nason, Carlo Oleari, and Emanuele Re. A general framework for implementing NLO calculations in shower Monte Carlo programs: the POWHEG BOX. *Journal of High Energy Physics*, 2010(6), 2010. ISSN 1029-8479. doi: 10.1007/jhep06(2010)043. URL http://dx.doi.org/10.1007/JHEP06(2010)043.

[30] S. Agostinelli et al. GEANT 4 - a simulation toolkit. *Nuclear Instruments and Methods in Physics Research Section A: Accelerators, Spectrometers, Detectors and Associated Equipment*, 506(3):250 – 303, 2003. ISSN 0168-9002. doi: https://doi.

org/10.1016/S0168-9002(03)01368-8. URL http://www.sciencedirect.com/science/article/pii/S0168900203013688.

[31] P. Hernandez. Neutrino Physics. In *8th CERN–Latin-American School of High-Energy Physics*, pages 85–142, 2016. doi: 10.5170/CERN-2016-005.85.

[32] A. D. Sakharov. Violation of CP invariance, C asymmetry, and Baryon asymmetry of the Universe. *Journal of Experimental and Theoretical Physics Letters*, 1967.

[33] Gianfranco Bertone and Dan Hooper. History of dark matter. *Reviews of Modern Physics*, 90(4), Oct 2018. ISSN 1539-0756. doi: 10.1103/revmodphys.90.045002. URL http://dx.doi.org/10.1103/RevModPhys.90.045002.

[34] Katherine Garrett and Gintaras Duda. Dark Matter: A Primer. *Advances in Astronomy*, 2011. ISSN 1687-7977. doi: 10.1155/2011/968283. URL http://dx.doi.org/10.1155/2011/968283.

[35] translated by Kurt Riesselmann Wolfgang Pauli. Pauli's letter. URL https://www.symmetrymagazine.org/sites/default/files/legacy/pdfs/200703/logbook_letter_translation.pdf.

[36] R. Barbier, C. Berat, M. Besancon, M. Chemtob, A. Deandrea, E. Dudas, P. Fayet, S. Lavignac, G. Moreau, E. Perez, and et al. R-Parity-violating supersymmetry. *Physics Reports*, 420(1-6):1–195, 2005. ISSN 0370-1573. doi: 10.1016/j.physrep.2005.08.006. URL http://dx.doi.org/10.1016/j.physrep.2005.08.006.

[37] Herbi Dreiner. An introduction to explicit R-parity violation. *Pramana*, 51(1-2):123–133, 1998. ISSN 0973-7111. doi: 10.1007/bf02827485. URL http://dx.doi.org/10.1007/BF02827485.

[38] Timothy Cohen, Daniel J. Phalen, Aaron Pierce, and Kathryn M. Zurek. Asymmetric dark matter from a gev hidden sector. *Physical Review D*, 82(5), Sep 2010. ISSN 1550-2368. doi: 10.1103/physrevd.82.056001. URL http://dx.doi.org/10.1103/PhysRevD.82.056001.

[39] S. Ghigna, B. Moore, F. Governato, G. Lake, T. Quinn, and J. Stadel. Density Profiles and Substructure of Dark Matter Halos: Converging Results at Ultra-High Numerical Resolution. *The Astrophysical Journal*, 544(2):616–628, 2000. ISSN 1538-4357. doi: 10.1086/317221. URL http://dx.doi.org/10.1086/317221.

[40] Miguel Rocha, Annika H. G. Peter, James S. Bullock, Manoj Kaplinghat, Shea Garrison-Kimmel, Jose OÂorbe, and Leonidas A. Moustakas. Cosmological simulations with self-interacting dark matter I: Constant-density cores and substructures. *Monthly Notices of the Royal Astronomical Society*, 430(1), 2013. ISSN 0035-8711. doi: 10.1093/mnras/sts514. URL http://dx.doi.org/10.1093/mnras/sts514.

[41] Annika H. G. Peter, Miguel Rocha, James S. Bullock, and Manoj Kaplinghat. Cosmological simulations with self-interacting dark matter II: Halo shapes versus observations. *Monthly Notices of the Royal Astronomical Society*, 430(1), 2013. ISSN 0035-8711. doi: 10.1093/mnras/sts535. URL `http://dx.doi.org/10.1093/mnras/sts535`.

[42] Mark Vogelsberger, Jesus Zavala, and Abraham Loeb. Subhaloes in self-interacting galactic dark matter haloes. *Monthly Notices of the Royal Astronomical Society*, 423 (4):3740–3752, 2012. ISSN 0035-8711. doi: 10.1111/j.1365-2966.2012.21182.x. URL `http://dx.doi.org/10.1111/j.1365-2966.2012.21182.x`.

[43] Jesu Zavala, Mark Vogelsberger, and Matthew G. Walker. Constraining self-interacting dark matter with the Milky Way'sdwarf spheroidals. *Monthly Notices of the Royal Astronomical Society: Letters*, 431(1):L20–L24, 2013. ISSN 1745-3925. doi: 10.1093/mnrasl/sls053. URL `http://dx.doi.org/10.1093/mnrasl/sls053`.

[44] Myeonghun Park and Mengchao Zhang. Tagging a jet from a dark sector with jet substructures at colliders. *Physical Review D*, 100(11), 2019. ISSN 2470-0029. doi: 10.1103/physrevd.100.115009. URL `http://dx.doi.org/10.1103/PhysRevD.100.115009`.

[45] ATLAS Collaboration. Search for new phenomena in events with jets and missing transverse momentum in $pp$ collisions at $\sqrt{s} = 13$ TeV with the ATLAS detector. Technical Report ATLAS-CONF-2020-048, CERN, Geneva, 2020. URL `http://cds.cern.ch/record/2728058`.

[46] Juliette Alimena et. al. Searching for long-lived particles beyond the Standard Model at the Large Hadron Collider, 2019.

[47] Timothy Cohen, Mariangela Lisanti, and Hou Keong Lou. Semivisible Jets: Dark Matter Undercover at the LHC. *Physical Review Letters*, 115(17), 2015. ISSN 1079-7114. doi: 10.1103/physrevlett.115.171804. URL `http://dx.doi.org/10.1103/PhysRevLett.115.171804`.

[48] Deepak Kar and Sukanya Sinha. Exploring Jet Substructure in Semi-visible jets, 2020.

[49] J L Abelleira Fernandez, C Adolphsen, A N Akay, H Aksakal, J L Albacete, S Alekhin, P Allport, V Andreev, R B Appleby, E Arikan, and et al. A large hadron electron collider at cern report on the physics and design concepts for machine and detector. *Journal of Physics G: Nuclear and Particle Physics*, 39(7):075001, Jul 2012. ISSN 1361-6471. doi: 10.1088/0954-3899/39/7/075001. URL `http://dx.doi.org/10.1088/0954-3899/39/7/075001`.

[50] ATLAS Collaboration. The ATLAS Experiment at the CERN Large Hadron Collider. *JINST*, 3:S08003. 437 p, 2008. doi: 10.1088/1748-0221/3/08/S08003. URL `http://cds.cern.ch/record/1129811`. Also published by CERN Geneva in 2010.

[51] ALICE Collaboration. The alice experiment at the cern lhc. *Nuclear Physics B - Proceedings Supplements*, 117:62 – 64, 2003. ISSN 0920-5632. doi: https://doi.org/10.1016/S0920-5632(03)90488-9. URL `http://www.sciencedirect.com/science/article/pii/S0920563203904889`.

[52] CMS Collaboration. *CMS Physics: Technical Design Report Volume 1: Detector Performance and Software*. Technical Design Report CMS. CERN, Geneva, 2006. URL `https://cds.cern.ch/record/922757`.

[53] Jr. Alves, A.Augusto et al. The LHCb Detector at the LHC. *JINST*, 3:S08005, 2008. doi: 10.1088/1748-0221/3/08/S08005.

[54] ATLAS Collaboration. Luminosity Public Results Run2, 2019. URL `https://twiki.cern.ch/twiki/bin/view/AtlasPublic/LuminosityPublicResultsRun2`.

[55] Ahmed Tarek. *Measurement of Higgs boson production cross sections in the diphoton channel with the full ATLAS Run-2 data and constraints on anomalous Higgs boson interactions*. PhD thesis, 2019. URL `https://cds.cern.ch/record/2696211`. Presented 30 Sep 2019.

[56] ATLAS Collaboration. *ATLAS magnet system: Technical Design Report, 1*. Technical Design Report ATLAS. CERN, Geneva, 1997. URL `https://cds.cern.ch/record/338080`.

[57] J.J. Goodson. *Search for Supersymmetry in States with Large Missing Transverse Momentum and Three Leptons including a Z-Boson*. PhD thesis, Stony Brook University, 2012. Presented 17 Apr 2012.

[58] ATLAS Collaboration. Performance of the ATLAS track reconstruction algorithms in dense environments in LHC Run 2. *The European Physical Journal C*, 77(10), 2017. ISSN 1434-6052. doi: 10.1140/epjc/s10052-017-5225-7. URL `http://dx.doi.org/10.1140/epjc/s10052-017-5225-7`.

[59] ATLAS Collaboration. Luminosity determination in $pp$ collisions at $\sqrt{s} = 13$ TeV using the ATLAS detector at the LHC. Technical Report ATLAS-CONF-2019-021, CERN, Geneva, Jun 2019. URL `http://cds.cern.ch/record/2677054`.

[60] ATLAS Collaboration. Technical Design Report for the Phase-I Upgrade of the ATLAS TDAQ System. 2013.

[61] M. Aleksa, W. Cleland, Y. Enari, M. Fincke-Keeler, L. Hervas, F. Lanni, S. Majewski, C. Marino, and I. Wingerter-Seez. ATLAS Liquid Argon Calorimeter Phase-I Upgrade Technical Design Report. Technical Report CERN-LHCC-2013-017. ATLAS-TDR-022, 2013. URL `https://cds.cern.ch/record/1602230`. Final version presented to December 2013 LHCC.

[62] R. Schwitters. Hadron Production at SPEAR. 1975.

[63] ATLAS Collaboration. Topological cell clustering in the ATLAS calorimeters and its performance in LHC Run 1. *The European Physical Journal C*, 77(7), 2017. ISSN 1434-6052. doi: 10.1140/epjc/s10052-017-5004-5. URL `http://dx.doi.org/10.1140/epjc/s10052-017-5004-5`.

[64] ATLAS Collaboration. Jet reconstruction and performance using particle flow with the ATLAS Detector. *The European Physical Journal C*, 77(7), 2017. ISSN 1434-6052. doi: 10.1140/epjc/s10052-017-5031-2. URL `http://dx.doi.org/10.1140/epjc/s10052-017-5031-2`.

[65] Improving jet substructure performance in ATLAS using Track-CaloClusters. Technical Report ATL-PHYS-PUB-2017-015, CERN, Geneva, 2017. URL `http://cds.cern.ch/record/2275636`.

[66] Matteo Cacciari, Gavin P Salam, and Gregory Soyez. The anti-kt jet clustering algorithm. *Journal of High Energy Physics*, 2008(04):63, 2008. ISSN 1029-8479. doi: 10.1088/1126-6708/2008/04/063. URL `http://dx.doi.org/10.1088/1126-6708/2008/04/063`.

[67] ATLAS Collaboration. Jet mass reconstruction with the ATLAS Detector in early Run 2 data. Technical Report ATLAS-CONF-2016-035, CERN, Geneva, 2016. URL `http://cds.cern.ch/record/2200211`.

[68] ATLAS Collaboration. Jet energy scale and resolution measured in proton-proton collisions at $\sqrt{s} = 13$ TeV with the ATLAS detector, 2020.

[69] ATLAS Collaboration. In situ calibration of large-radius jet energy and mass in 13 TeV proton-proton collisions with the ATLAS detector. *The European Physical Journal C*, 79(2), 2019. ISSN 1434-6052. doi: 10.1140/epjc/s10052-019-6632-8. URL `http://dx.doi.org/10.1140/epjc/s10052-019-6632-8`.

[70] ATLAS Collaboration. Performance of pile-up mitigation techniques for jets in $pp$ collisions at $\sqrt{s} = 8$ TeV using the ATLAS detector. *Eur. Phys. J.*, C76(11):581, 2016. doi: 10.1140/epjc/s10052-016-4395-z.

[71] Matteo Cacciari, Gavin P Salam, and Gregory Soyez. The catchment area of jets. *Journal of High Energy Physics*, 2008(04):005–005, 2008. ISSN 1029-8479.

doi: 10.1088/1126-6708/2008/04/005. URL http://dx.doi.org/10.1088/1126-6708/2008/04/005.

[72] ATLAS Collaboration. Impact of Alternative Inputs and Grooming Methods on Large-R Jet Reconstruction in ATLAS. Technical Report ATL-PHYS-PUB-2017-020, CERN, Geneva, 2017. URL https://cds.cern.ch/record/2297485.

[73] ATLAS Collaboration. Jet reclustering and close-by effects in ATLAS run II. Technical Report ATLAS-CONF-2017-062, CERN, Geneva, 2017. URL https://cds.cern.ch/record/2275649.

[74] ATLAS Collaboration. In situ large-r jet energy scale calibration and uncertainties in 2015-2017 data, 2019. URL https://atlas.web.cern.ch/Atlas/GROUPS/PHYSICS/PLOTS/JETM-2019-05/.

[75] ATLAS Collaboration. Search for low-mass dijet resonances using trigger-level jets with the ATLAS detector in $pp$ collisions at $\sqrt{s} = 13$ TeV. *Phys. Rev. Lett.*, 121(8): 081801, 2018. doi: 10.1103/PhysRevLett.121.081801.

[76] CMS Collaboration. Search for dijet resonances in proton-proton collisions at $\sqrt{s} = 13$tev and constraints on dark matter and other models. *Physics Letters B*, 769, 2017. ISSN 0370-2693. doi: 10.1016/j.physletb.2017.02.012. URL http://dx.doi.org/10.1016/j.physletb.2017.02.012.

[77] LHCb Collaboration. Tesla: An application for real-time data analysis in High Energy Physics. *Computer Physics Communications*, 208, 2016. ISSN 0010-4655. doi: 10.1016/j.cpc.2016.07.022. URL http://dx.doi.org/10.1016/j.cpc.2016.07.022.

[78] ATLAS Collaboration. A measurement of the calorimeter response to single hadrons and determination of the jet energy scale uncertainty using LHC Run-1 pp-collision data with the ATLAS detector. *The European Physical Journal C*, 77(1), 2017. ISSN 1434-6052. doi: 10.1140/epjc/s10052-016-4580-0. URL http://dx.doi.org/10.1140/epjc/s10052-016-4580-0.

[79] ATLAS Collaboration. Track assisted techniques for jet substructure. Technical Report ATL-PHYS-PUB-2018-012, CERN, Geneva, Jul 2018. URL https://cds.cern.ch/record/2630864.

[80] ATLAS Collaboration. Measurement of the ATLAS Detector Jet Mass Response using Forward Folding with 80 $\text{fb}^{-1}$ of $\sqrt{s} = 13$ TeV $pp$ data. Technical Report ATLAS-CONF-2020-022, CERN, Geneva, Jul 2020. URL https://cds.cern.ch/record/2724442.

[81] Jesse Thaler and Ken Van Tilburg. Identifying boosted objects with N-subjettiness. *Journal of High Energy Physics*, 2011(3), 2011. ISSN 1029-8479. doi: 10.1007/jhep03(2011)015. URL http://dx.doi.org/10.1007/JHEP03(2011)015.

[82] ATLAS Collaboration. Identification of boosted, hadronically decaying W bosons and comparisons with ATLAS data taken at $\sqrt{s} = 8$ TeV. *The European Physical Journal C*, 76(3), 2016. ISSN 1434-6052. doi: 10.1140/epjc/s10052-016-3978-z. URL http://dx.doi.org/10.1140/epjc/s10052-016-3978-z.

[83] ATLAS Collaboration. Quark versus Gluon Jet Tagging Using Charged Particle Multiplicity with the ATLAS Detector. Technical Report ATL-PHYS-PUB-2017-009, CERN, Geneva, 2017. URL https://cds.cern.ch/record/2263679.

[84] ATLAS Collaboration. ATLAS b-jet identification performance and efficiency measurement with $t\bar{t}$-events in pp collisions at $\sqrt{s} = 13$ TeV. *The European Physical Journal C*, 79(11), 2019. ISSN 1434-6052. doi: 10.1140/epjc/s10052-019-7450-8. URL http://dx.doi.org/10.1140/epjc/s10052-019-7450-8.

[85] ATLAS Collaboration. A search for pair-produced resonances in four-jet final states at $\sqrt{s} = 13$ TeV with the ATLAS detector. *The European Physical Journal C*, 78 (3), 2018. ISSN 1434-6052. doi: 10.1140/epjc/s10052-018-5693-4. URL http://dx.doi.org/10.1140/epjc/s10052-018-5693-4.

[86] ATLAS Collaboration. ATLAS data quality operations and performance for 2015–2018 data-taking. *JINST*, 15:P04003, 2020. doi: 10.1088/1748-0221/15/04/P04003.

[87] ATLAS Collaboration. Selection of jets produced in 13TeV proton-proton collisions with the ATLAS detector. Technical Report ATLAS-CONF-2015-029, CERN, Geneva, 2015. URL https://cds.cern.ch/record/2037702.

[88] ATLAS Collaboration. Summary of ATLAS Pythia 8 tunes. Technical Report ATL-PHYS-PUB-2012-003, CERN, Geneva, 2012. URL https://cds.cern.ch/record/1474107.

[89] Michele Redi, Veronica Sanz, Maikel de Vries, and Andreas Weiler. Strong Signatures of Right-Handed Compositeness. *JHEP*, 08:008, 2013. doi: 10.1007/JHEP08(2013)008.

[90] ATLAS Collaboration. ATLAS Pythia 8 tunes to 7 TeV datas. Technical Report ATL-PHYS-PUB-2014-021, CERN, Geneva, 2014. URL https://cds.cern.ch/record/1966419.

[91] Peter Z. Skands. Tuning monte carlo generators: The perugia tunes. *Phys. Rev. D*, 82: 074018, Oct 2010. doi: 10.1103/PhysRevD.82.074018. URL https://link.aps.org/doi/10.1103/PhysRevD.82.074018.

[92] ATLAS Collaboration. Performance of b-jet identification in the ATLAS experiment. *Journal of Instrumentation*, 11(04):P04008Ã04008, 2016. ISSN 1748-0221. doi: 10.1088/1748-0221/11/04/p04008. URL `http://dx.doi.org/10.1088/1748-0221/11/04/P04008`.

[93] ATLAS Collaboration. Search for pair-produced massive coloured scalars in four-jet final states with the ATLAS detector in proton-proton collisions at $\sqrt{s} = 7$ TeV. *The European Physical Journal C*, 73(1), 2013. ISSN 1434-6052. doi: 10.1140/epjc/s10052-012-2263-z. URL `http://dx.doi.org/10.1140/epjc/s10052-012-2263-z`.

[94] ATLAS Collaboration. A search for top squarks with R-parity-violating decays to all-hadronic final states with the ATLAS detector in $\sqrt{s} = 8$ TeV proton-proton collisions. *Journal of High Energy Physics*, 2016(6), 2016. ISSN 1029-8479. doi: 10.1007/jhep06(2016)067. URL `http://dx.doi.org/10.1007/JHEP06(2016)067`.

[95] Jim Alexander et al. Dark Sectors 2016 Workshop: Community Report, 2016.

[96] ATLAS Collaboration. Search for diboson resonances in hadronic final states in 139 fb of pp collisions at $\sqrt{13}$ TeV with the ATLAS detector. *Journal of High Energy Physics*, 2019(9), 2019. ISSN 1029-8479. doi: 10.1007/jhep09(2019)091. URL `http://dx.doi.org/10.1007/JHEP09(2019)091`.

[97] ATLAS Collaboration. A search for the $z\gamma$ decay mode of the higgs boson in pp collisions at s=13 tev with the atlas detector. *Physics Letters B*, 809:135754, Oct 2020. ISSN 0370-2693. doi: 10.1016/j.physletb.2020.135754. URL `http://dx.doi.org/10.1016/j.physletb.2020.135754`.

[98] ATLAS Collaboration. Performance of mass-decorrelated jet substructure observables for hadronic two-body decay tagging in ATLAS. Technical Report ATL-PHYS-PUB-2018-014, CERN, Geneva, 2018. URL `https://cds.cern.ch/record/2630973`.

[99] N. S. Altman. An introduction to kernel and nearest-neighbor nonparametric regression. *The American Statistician*, 46(3):175–185, 1992. doi: 10.1080/00031305.1992.10475879. URL `https://www.tandfonline.com/doi/pdf/10.1080/00031305.1992.10475879`.

[100] David W. Scott. Scott's rule. *WIREs Computational Statistics*, 2(4):497–502, 2010. doi: 10.1002/wics.103. URL `https://www.onlinelibrary.wiley.com/doi/abs/10.1002/wics.103`.

[101] S. S. Wilks. The large-sample distribution of the likelihood ratio for testing composite hypotheses. *Ann. Math. Statist.*, 9(1):60–62, 1938. doi: 10.1214/aoms/1177732360. URL `https://doi.org/10.1214/aoms/1177732360`.

[102] ATLAS Collaboration. Luminosity determination in $pp$ collisions at $\sqrt{s} = 13$ TeV using the ATLAS detector at the LHC. Technical Report ATLAS-CONF-2019-021, CERN, Geneva, 2019. URL `https://cds.cern.ch/record/2677054`.

[103] G. Avoni et al. The new lucid-2 detector for luminosity measurement and monitoring in atlas. *JINST*, 13(07):P07017, 2018. doi: 10.1088/1748-0221/13/07/P07017.